A Novel Overactuated Quadrotor UAV

Von der Fakultät Konstruktions-, Produktions- und Fahrzeugtechnik der Universität Stuttgart zur Erlangung der Würde eines Doktor-Ingenieurs (Dr.-Ing.) genehmigte Abhandlung

Vorgelegt von

Markus Ryll

aus Stuttgart

Hauptberichter:	Prof. Dr.-Ing. Frank Allgöwer
Mitberichter:	Prof. Dr. Heinrich H.Bülthoff
	Prof. Dr. Lorenzo Marconi

Tag der mündlichen Prüfung: 06. Februar 2015

Institut für Systemtheorie und Regelungstechnik

Universität Stuttgart

2015

Acknowledgements

First of all I would like to thank my direct supervisor Dr. Paolo Robuffo Giordano for the supervision of my thesis, his great support at any day and night time, steady encouragement and continuous motivation. Working together with Paolo is always a great joy. I also want to express my thankfulness to Prof. Dr. Heinrich H. Bülthoff for his support and the promotion of my PhD by stimulating me in my research and asking critical questions in the right moment. Prof. Dr. Heinrich H. Bülthoff created a great melting pot of scientists from different backgrounds at the Max Planck Institute for Biological Cybernetics that is probably unique in the world. In the same manner I want thank Prof. Dr. Frank Allgöwer, for accepting me as his Ph.D.-student at the University of Stuttgart, without him this work would not have been possible. Many thanks go to all the current and previous members of the 'Autonomous Robotics and Human-Machine Systems'-group. I enjoyed every single day spent with you in- and outside the office. As well I want to thank all the people that accompanied me in the last 4 years and often became good friends.

I am also grateful to my family, my parents and my siblings Thomas and Karoline, for the background they gave me. Most of all I would like to thank Katharina for always standing by me in the office and at home. You fill my and Lotta's life with love, happiness and adventure.

Tübingen, July 2014

Markus Ryll

Table of Contents

List of Variables

Conventions

a, b	Scalar
$\boldsymbol{a}, \boldsymbol{b}$	Vector
$\boldsymbol{A}, \boldsymbol{B}$	Matrix
$\mathcal{A}, \mathcal{B}$	Coordinate frame
$\dot{a}$	Temporal derivative of quantity a
$[\boldsymbol{a}]_\times \in \mathbb{R}^{3\times3}$	Skew symmetric matrix associated to vector $\boldsymbol{a} \in \mathbb{R}^3$ such that $a \times b = [\boldsymbol{a}]_\times b$
$\|\boldsymbol{a}\| \in \mathbb{R}$	Norm of vector $\boldsymbol{a}$

Most important variables used globally throughout this thesis.

Definitions:

$\mathcal{F}_B$	Quadrotor body frame B
$\mathcal{F}_W$	Inertial world frame
$\mathcal{F}_{P_i}$	i-th propeller group frame P_i
${}^W\boldsymbol{R}_B$	Rotation matrix from $\mathcal{F}_B$ to $\mathcal{F}_W$
${}^B\boldsymbol{R}_{P_i}$	Rotation matrix from $\mathcal{F}_{P_i}$ to $\mathcal{F}_B$

Latin symbols:

$A \in \mathbb{R}^3$ $[m^2]$	Propeller disk area
$a \in \mathbb{R}$ [1]	Lift slope
$\boldsymbol{a} \in \mathbb{R}^3$ $[\frac{\mathrm{m}}{\mathrm{s}^2}]$	Linear acceleration

$\bar{C}_d \in \mathbb{R}$	Average drag coefficient
$\boldsymbol{I}_B \in \mathbb{R}^{3\times3}$ $[\frac{\text{kg}}{\text{m}^2}]$	Inertia of the quadrotor body B
$\boldsymbol{F}_H \in \mathbb{R}^3$ [N]	Hub force
$g \in \mathbb{R}$ $[\frac{\text{m}}{\text{s}^2}]$	Gravitational acceleration of Earth $\approx 9.81 \frac{\text{m}}{\text{s}^2}$
$L \in \mathbb{R}$ [m]	Distance of $\mathcal{F}_{P_i}$ from $\mathcal{F}_B$
$m \in \mathbb{R}$ [kg]	Total mass of the holocopter
$\boldsymbol{I}_P \in \mathbb{R}^{3\times3}$ $[\frac{\text{kg}}{\text{m}^2}]$	Inertia of the i-th propeller group P_i
$k_f \in \mathbb{R}$ $[\frac{\text{N}}{\text{rad}}]$	Propeller thrust coefficient
$k_m \in \mathbb{R}$ $[\frac{\text{Nm}}{\text{rad}}]$	Propeller drag coefficient
$\boldsymbol{p} \in \mathbb{R}^3$ [m]	Position of B in $\mathcal{F}_W$
$R \in \mathbb{R}$ [m]	Propeller radius
$\boldsymbol{T}_i \in \mathbb{R}^3$ [N]	i-th propeller thrust along $\boldsymbol{Z}_{P_i}$
$\boldsymbol{v} \in \mathbb{R}^3$ $[\frac{\text{m}}{\text{s}}]$	Linear velocity
$v_1 \in \mathbb{R}$ $[\frac{\text{m}}{\text{s}}]$	Propeller inflow velocity
$\bar{w}_i \in \mathbb{R}$ $[\frac{\text{rad}}{\text{s}}]$	i-th propeller spinning velocity about $\boldsymbol{Z}_{P_i}$
$\dot{x}_{P_i}, \dot{y}_{P_i}, \dot{z}_{P_i} \in \mathbb{R}$ $[\frac{\text{m}}{\text{s}}]$	Velocity of the propeller w.r.t. ground

Greek symbols:

$\alpha_i \in \mathbb{R}$ [rad]	i-th propeller tilt angle about $\boldsymbol{X}_{P_i}$
$\theta \in \mathbb{R}$ [rad]	Roll angel
$\theta_{tw} \in \mathbb{R}$ [rad]	Twist pitch
$\theta_0 \in \mathbb{R}$ $[rad]$	Pitch of incidence
$\lambda_i \in \mathbb{R}$ [1]	Inflow ratio
$\mu_i \in \mathbb{R}$ [1]	Rotor advance ratio
$\rho \in \mathbb{R}$ $[\frac{\text{kg}}{\text{m}^3}]$	Air density
$\tau_{P_i} \in \mathbb{R}$ [Nm]	Motor torque actuating $\boldsymbol{X}_{P_i}$
$\boldsymbol{\tau}_R \in \mathbb{R}^3$ [Nm]	Rolling moment
$\boldsymbol{\tau}_{ext_i} \in \mathbb{R}^3$ [Nm]	i-th propeller air drag torque about $\boldsymbol{Z}_{P_i}$
$\sigma \in \mathbb{R}$ $[\frac{1}{\text{rad}}]$	Solidity ratio
$\tau_{\bar{\omega}_i} \in \mathbb{R}$ [Nm]	Motor torque actuating $\boldsymbol{Z}_{P_i}$

$\phi \in \mathbb{R}$ [rad]	Pitch angel
$\psi \in \mathbb{R}^3$ [rad]	Yaw angel
$\boldsymbol{\omega}_B \in \mathbb{R}^3$ $[\frac{\text{rad}}{\text{s}}]$	Angular velocity of B in $\mathcal{F}_B$

All other symbols are only defined locally for one section and might be used in other sections in a different context. This allowed the authors to adapt to common notations and symbols whenever possible. For the reader's convenience most important symbols of a section are summarized in tables in the same section.

List of Abbreviations

A/D	Analog/Digital
ATX	Advanced Technology eXtended
BL-Ctrl	Brushless controller
CAD	Computer-aided design
CAN	Controller area network
DC	Direct current
DDR2	Double Data Rate 2
dof	Degree of freedom
e.g.	Exempli gratia
EC	Electronically commutated
Fig.	Figure
I^2C	Inter-Integrated Circuit
i.e	Id est
IMU	Inertial measurement unit
LTS	Long-term support
MAV	Micro aerial vehicel
MEMS	Microelectromechanical systems
MoCap	Motion capture system
MOSFETS	Metal-oxide-semiconductor field-effect transistor
OS	Operating system
PC	Personal computer
PID	Proportional-integral-derivative
PWM	Pulse-width modulation
RAM	Random-access memory

RC	Remote control
Sect.	Section
TTL	Transistor-transistor logic
UAV	Unmanned aerial vehicle
USB	Universal Serial Bus
w.r.t.	With respect to

Abstract

Standard quadrotor UAVs are inherently underactuated as they posses only four independent control inputs - their four propeller spinning velocities. Therefore they only possess a limited mobility in space for the six dofs parameterizing the quadrotor position/orientation. This implies that for standard quadrotors it is impossible to follow an arbitrarily designed trajectory. A standard quadrotor for example cannot translate position while remaining horizontal. The common use of UAVs and quadrotors in particular is changing from common observer tasks to more applied *flying service robot* tasks including interaction with the environment. Here the loss of mobility on the basis of the inherent underactuation can constitute a limiting factor. In this thesis we will present a novel quadrotor UAV design that surmounts these limitations by additional four control inputs actuating the four *propeller tilting angles*. First, we will show that our novel quadrotor UAV with tilting propellers offers behavior as a fully-actuated flying vehicle with full actuation of the quadrotor position and orientation in space. Second, a comprehensive modeling and control framework for the proposed quadrotor is presented, and the hardware/software specifications of an experimental prototype will be introduced. Finally, the results of several simulations and real experiments are reported to illustrate the capabilities of the proposed novel UAV design.

Deutsche Kurzfassung

Neue Ansätze zur Regelung überaktuierter, unbemannte Luftfahrzeuge

Unbemannte Quadrocopter und ähnliche Luftfahrzeuge (z.B. Hubschrauber) haben eine eingeschränkte Manövrierbarkeit aufgrund ihres konzeptuell unteraktuierten Systems. Das heißt diese Luftfahrzeuge besitzen weniger Steuereingänge (im Falle von Quadrocoptern die vier Rotationsgeschwindigkeiten der Rotoren) als die sechs translatorischen und rotatorischen Freiheitsgrade eines Körpers im Raum. Daraus folgt das diese Luftfahrzeuge einer beliebigen Trajektorie im Raum nicht notwendigerweise folgen können. Beispielsweiße ist eine horizontale Translation ohne Rotation nicht möglich. Da unbemannte Luftfahrzeuge mehr und mehr als *fliegende Serviceroboter*, die auf ihre Umgebung einwirken, verwendet werden, ist dieser Mangel an Mobilität ein grundsätzlich limitierender Faktor. In dieser Doktorarbeit wird ein konstruktiv neuartiger Entwurf eines Luftfahrzeuges vorgestellt - der **Holocopter**. Beim Holocopter ist zusätzlich die *Orientierung der Rotoren* regelbar, hier durch ist die beschriebene Unteraktuierung nicht mehr gegeben. Das System ist nun überaktuiert, da den nun acht Steuereingängen sechs Freiheitsgrade gegenüberstehen. Die vier zusätzlichen Steuereingänge ermöglichen eine vollständige Steuerbarkeit der Position und Orientierung des Holocopters im Raum. Daher lässt sich der Holocopter als vollständig steuerbarer, fliegender Roboter verwenden. In dieser Arbeit wurde zunächst ausführlich das kinematische Modell des Holocopters hergeleitet und ein passender Regler basierend auf dynamischer, linearisierter Zustandsrückführung entworfen. Anschließend wurde ein

Prototyp entworfen und gebaut und das nötige Software-Framework entwickelt. Zentraler Bestandteil der Arbeit sind ausführliche Simulationen und tatsächliche Tests mit den Prototypen. Abschließend bietet die Arbeit einen Ausblick auf Interaktionsszenarios des Holocopters mit der Umgebung.

Chapter 1

Introduction

In the past decade research on Unmanned Aerial Vehicles (UAVs) experienced an enormous increment of growth (see e.g. Bouabdallah et al. (2007); Gurdan et al. (2007); Mellinger et al. (2010); Pounds et al. (2010); Valavanis (2007)). A literature research lists 117 publications containing the phrase "'Unmanned Aerial Vehicles"' in major journals and conferences in 2003. In 2008 this are already 459 publications while in 2013 it exceeds 845 articles (see figure 1.1). In particular micro aerial vehicles (MAVs) contribute to this interest. This vast growth is due to several facts e.g. advances in microelectromechanical systems and sensors (MEMS), increasing computational power of microcontrollers and miniaturized computer systems, improvements in energy storage on batteries and the overall decreasing costs for UAVs. All this offers new application areas for UAVs and MAVs in various fields like search and rescue missions, data collection, autonomous exploration and surveillance in inaccessible disaster areas, beneficial from a research point of view as well as for our society. While MAV research in its beginning mainly focused on general control of the MAV system and it localization (here self localization and mapping has to be mentioned) a new topic rose in the last years - the transitional use of MAVs from 'autonomous flying vehicles' into more robotic oriented 'autonomous flying *service robots*'. This means a transition from pure observer tasks to the possibility of actual interaction with the environment either by robust incidental interaction (Briod (2014)), simple grasping/manipulation tasks (Lindsey et al. (2011); Pound et al. (2011)) or desired long term contact in the meaning of manipulation (Gentili et al. (2008); Gioioso et al. (2014); Naldi and Marconi (2010)). The extension of tasks as well as their complexity demands as well innovative breakthroughs

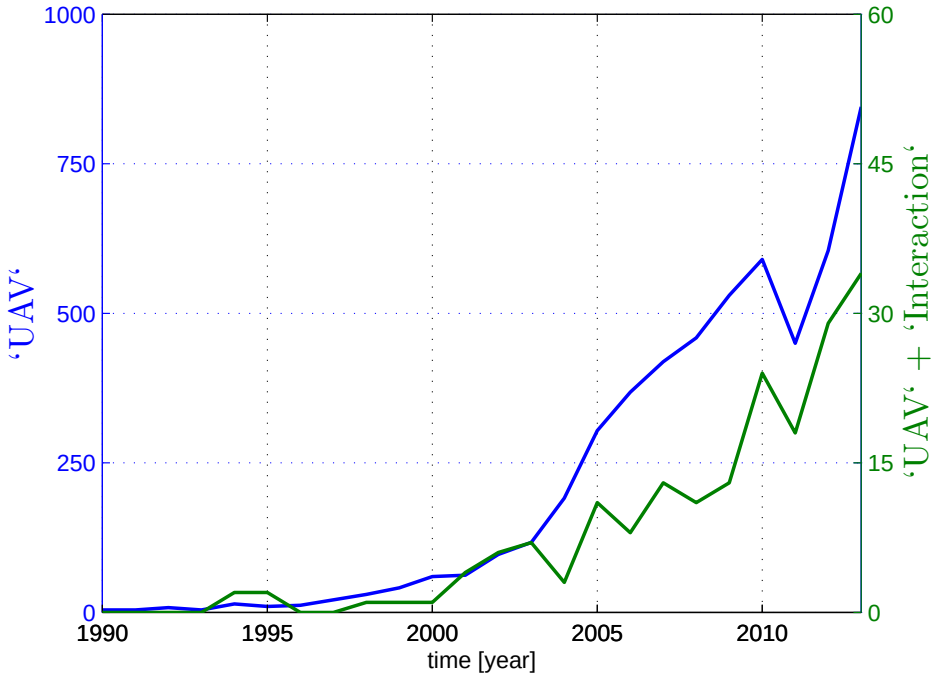

Figure 1.1: Publications listed at http://ieeexplore.ieee.org including either the term "'*Unmanned Aerial Vehicle*"' (blue line and left axis) or '*Unmanned Aerial Vehicle*' and '*Interaction*' (green line and right axis) in the abstract.

on the mechanical and actuation side. Most of current common UAVs and MAVs are underactuated mechanical systems, meaning that these systems possess less control inputs than available degrees of freedom (dofs).

This holds for example for the two most common UAVs, which are helicopters and quadrotors. In both cases only the Cartesian position and the vertical attitude (yaw angle) w.r.t. an inertial frame can be independently controlled (4 dofs). The other remaining 2 dofs, in this case the roll and pitch angles, are determined by the trajectory chosen for the former 4 dofs. This property is well studied and in usually referred as the quadrotor 'flat outputs' (see Bouabdallah et al. (2007); Mahony et al. (2012); Pounds et al. (2010)).

In the past years, a plenty of different control techniques have been introduced to deal and overcome the given underactuation of quadrotors to facilitate not only effective and fast but as well robust flight performances, compare Hua et al. (2009, 2013a); Mahony et al. (2012) for an overview. The aforementioned improvements in the miniaturization of MEMS and in the computational power of microcontrollers have led to impressive

achievements by employing quadrotor UAVs as robotics platforms: planning and control for aggressive flight maneuvers (Mellinger et al. (2010)), collective control of multiple small- and micro-quadrotors (Franchi et al. (2012); Kushleyev et al. (2012)), and vision-based state estimation for autonomous flight (Shen et al. (2013)) are just a few examples.

However the underactuated design of most common UAVs still limits on one hand the maneuverability in either free or cluttered environments and on the other hand and probably even more importantly corrupts diversity of possible interactions with the environment by exerting desired but arbitrary forces and torques in all directions. In particular this limiting factor determines common quadrotor UAVs while they are more and more exploited as autonomous flying *service robots*. Flying robots is a vast growing academic and economic branch of robotics as e.g. proven by the recently funded EU projects "AIRobots" EU Collaborative Project ICT-248669 AIRobots and "ARCAS" EU Collaborative Project ICT-287617 ARCAS. Indeed, several groups have been addressing the possibility to allow for an actual interaction with the environment, either in the form of direct contact Gentili et al. (2008); Marconi and Naldi (2012); Naldi and Marconi (2010) or by considering aerial grasping/manipulation tasks Lindsey et al. (2011); Manubens et al. (2013); Pound et al. (2011); Spica et al. (2012); Sreenath and Kumar (2013). In this respect, as also recognized in Hua et al. (2013b); Long and Cappelleri (2013), it is interesting to explore different actuation strategies that can overcome the aforementioned underactuation problem and allow for full motion and force control in all directions in space.

Motivated by these considerations, several solutions have been proposed in the past literature spanning different concepts as, e.g., using multiple UAVs to manipulate a cable-towed object Manubens et al. (2013), ducted-fan designs Naldi et al. (2010), tilt-wing mechanisms Oner et al. (2008, 2009), UAVs with non-parallel (but fixed) thrust directions Voyles and Jiang (2012), or tilt-rotor actuations Kendoul et al. (2006); Sanchez et al. (2008). In Forte et al. (2012b), the possibility of combining several modules of underactuated ducted-fan vehicles to achieve full 6-dof actuation for the assembled robot is theoretically explored, with a special focus on the optimal allocation of the available (redundant) control inputs. In contrast, the authors of Hua et al. (2013b) consider the possibility of a 'thrust-tilted' quadrotor UAV in which the main thrust direction (2 dofs) can be actively regulated. A trajectory tracking control strategy is then proposed, which is able to explicitly take

into account a limited range of the thrust tilting angles. Finally, in Long and Cappelleri (2013) a UAV made of two central coaxial counter-rotating propellers surrounded by three tilting thrusters has been presented along with some preliminary experimental results. The prototype is capable of two flight modalities: a 'fixed configuration' in which it essentially behaves as a standard underactuated UAV, and a 'variable angle' configuration which guarantees some degree of full actuation as shown in the reported results.

1.1 Summary of Contributions

Inspired by the aforementioned works for this theses we opted for a novel actuation concept of a quadrotor UAV with propellers actuated revolvable about the axes connecting them to the main body frame Falconi and Melchiorri (2012); Ryll et al. (2012, 2013). As explained before standard quadrotor designs suffer from their intrinsic underactuation with only 4 control inputs (spinning velocity of the 4 rotors) which prevents an independent control of the position and orientation of the UAV at the same time. For example, for classical quadrotors lateral transitions are impossible without changing the attitude to accelerate into the desired lateral direction. In other words classical quadrotors can hover *only* stationary if the plane in which the motors lie is parallel to the ground plane (vertical to gravity vector). In opposition to standard quadrotors the presented quadrotor is able to gain full controllability over position and orientation by exploiting the additional actuation of the propeller orientation, thus transforming it, as a matter of fact, in a fully actuated flying rigid body[1]. Apart from the challenges inherent to the control design for this novel UAV, we believe that endowing UAVs with full 6 dofs mobility will represent an important feature in many future applications, especially those involving interaction and manipulation as well as precise force and motion control in cluttered environments. Figure 1.2 shows a picture of our current prototype of 'quadrotor with tilting propellers', which will be denoted as *holocopter* throughout the following developments.

[1]This, of course, without taking into account possible limitations of the actuation systems such as, e.g., finite range for the tilting angles.

Figure 1.2: Picture of the holocopter prototype. The four propeller groups are slightly tilted. The red bar indicates the positive direction of the $\boldsymbol{X}_B$ holocopter body axis

1.2 Organization of the Thesis

The thesis, as well as its main contributions, are organized as follows:

1. a *complete* dynamical model of the holocopter is first derived in Sect. 2 by taking into account the dominant aerodynamic forces/torques (the propeller actuation), and by analyzing the effects of the main neglected terms;

2. a trajectory tracking controller is then presented in Sect. 3 aimed at exploiting the actuation capabilities of the holocopter for tracking arbitrary trajectories for its body position and orientation. As the holocopter is actually *overactuated* (8 control inputs for 6 controlled dofs), suitable strategies to exploit the actuation redundancy are also discussed: these are aimed at preserving full controllability of the holocopter pose and at minimizing the total energy consumption during flight;

3. a thorough description of the hardware/software architecture of the prototype shown in Fig. 1.2 is then given in Sect. 4, including the identification of its dynamical parameters and a discussion of the main non-idealities w.r.t. the dynamical model developed in Sect. 2. In particular, a predictive scheme complementing the control action of Sect. 3 is introduced in order to cope with the poor performance of the employed servo motors. Subsequently the hardware/software architecture of the improved and more advanced second prototype that is currently under final testing is as well thoroughly discussed and described;

4. an extensive set of ideal/realistic simulations and experimental results on the holocopter prototype is then presented in Sects. 5–8, showing the appropriateness of the various modeling assumptions and of the adopted control design. A video collecting several experimental flights is also available at `http://youtu.be/hA-uNHW8MLE`;

5. an outline of future developments on the control design for enabling interaction tasks is presented focusing on an admittance based control scheme utilizing the position controller presented in Sect. 3 and an force/torque observer to avoid the need of a force/torque sensor;

6. conclusions and some future discussions are then given in Sect. 8 with a focus on interaction tasks and the second prototype;

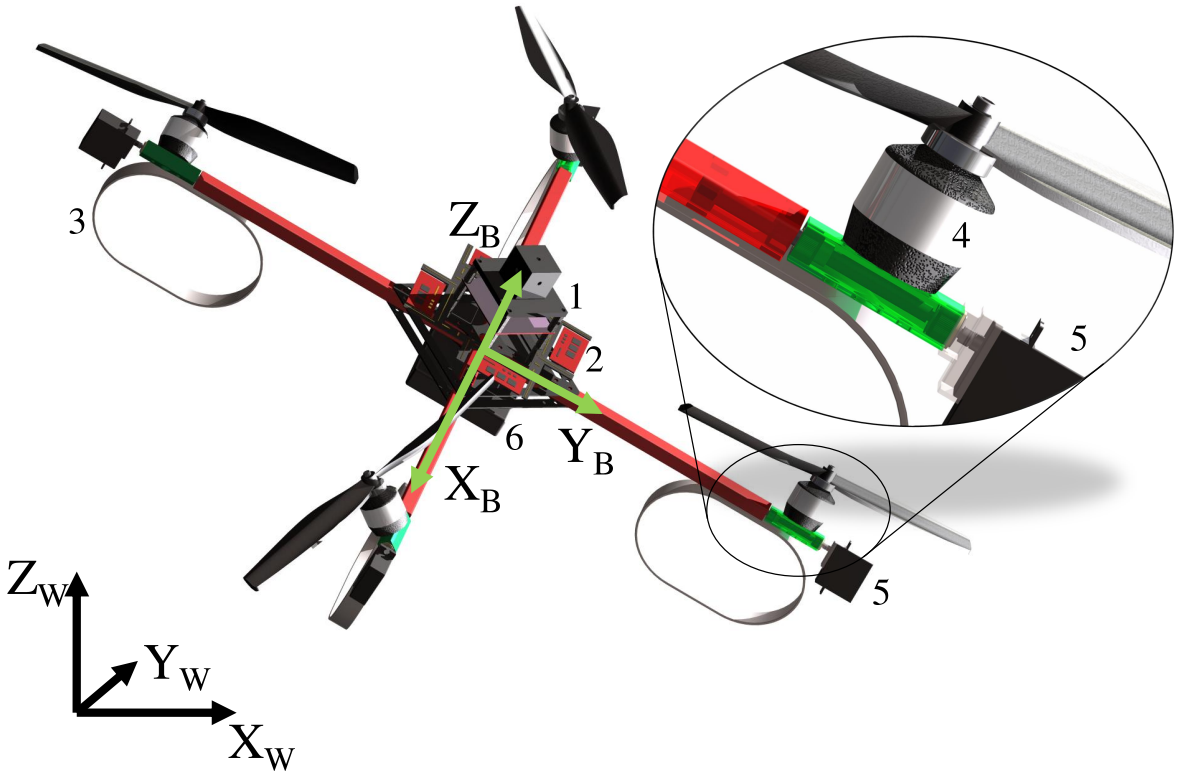

Figure 1.3: CAD model of the quadrotor with tilting propellers. The model is based on a quadrotor from mikrokopter.de, and is composed of: (1) Micro controller, (2) Brushless controller, (3) Lander, (4) Propeller motor, (5) Tilting actuator, (6) Battery.

We finally note that parts of this thesis have already been published in Ryll et al. (2012, 2013, to be published 2014).

Chapter 2

Dynamical Model of the Holocopter

This chapter has been mainly reproduced from an article published in ICRA 2012: Ryll et al. (2012)

The quadrotor analyzed in this thesis can be considered as a connection of 5 main rigid bodies in relative motion among themselves: the quadrotor body itself B and the 4 propeller groups P_i. These consist of the propeller arm hosting the motor responsible for the tilting actuation mechanism, and the propeller itself connected to the rotor of the motor responsible for the propeller spinning actuation[1] (see Figs. 1.2–2.2). The aim of this Section is to derive the equations of motion of this multi-body system.

2.1 Preliminary definitions

Let $\mathcal{F}_W : \{\boldsymbol{O}_W;\ \boldsymbol{X}_W,\ \boldsymbol{Y}_W,\ \boldsymbol{Z}_W\}$ be a world inertial frame and $\mathcal{F}_B : \{\boldsymbol{O}_B;\ \boldsymbol{X}_B,\ \boldsymbol{Y}_B,\ \boldsymbol{Z}_B\}$ a moving frame attached to the quadrotor body at its center of mass (see Fig. 2.1). We also define $\mathcal{F}_{P_i} : \{\boldsymbol{O}_{P_i};\ \boldsymbol{X}_{P_i},\ \boldsymbol{Y}_{P_i},\ \boldsymbol{Z}_{P_i}\}$, $i = 1 \dots 4$, as the frames associated to the i-th propeller group, with $\boldsymbol{X}_{P_i}$ representing the tilting actuation axis and $\boldsymbol{Z}_{P_i}$ the propeller actuated spinning (thrust T_i) axis (see Fig. 2.2).

As usual, we let ${}^1\boldsymbol{R}_2 \in SO(3)$ be the rotation matrix representing the orientation of frame 2 w.r.t. frame 1: therefore, ${}^W\boldsymbol{R}_B$ will represent the orientation of the body frame w.r.t. the world frame, while ${}^B\boldsymbol{R}_{P_i}$ the orientation of the propeller group i-th frame w.r.t. the body

[1] For simplicity we are here considering each propeller groups P_i as a 'single body approximation' of both the propeller/rotor and its hoisting mechanism.

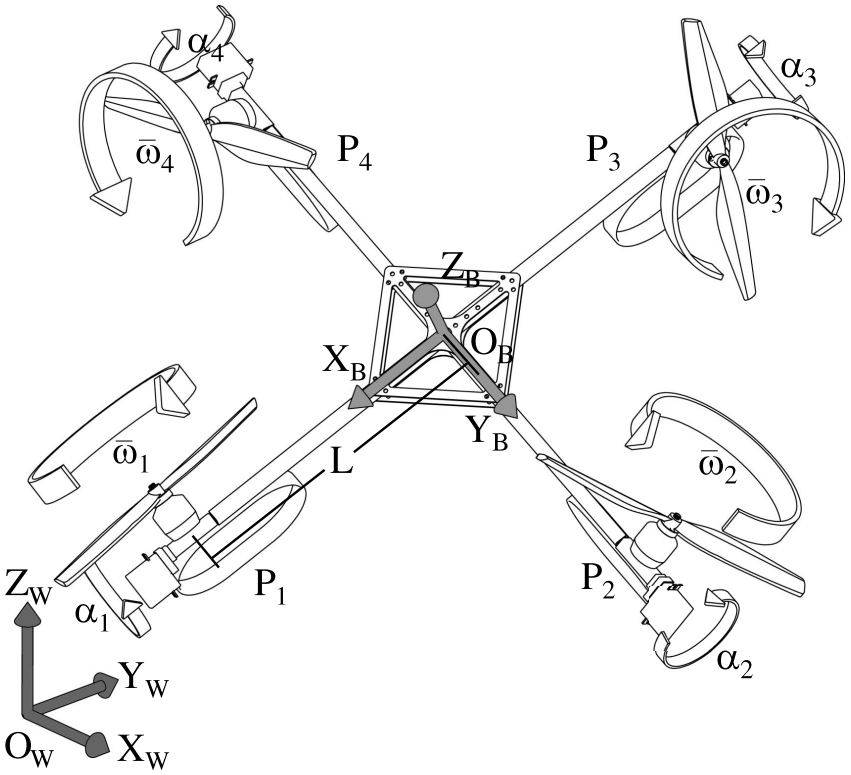

Figure 2.1: Schematic view of the quadrotor considered in this thesis. The overall center of mass is assumed to be in the body frame center. The symbol L represents the length of all propeller arms, ω_i, $i = 1 \dots 4$, the propeller rotation speed and α_i, $i = 1 \dots 4$, the orientation of the propeller group

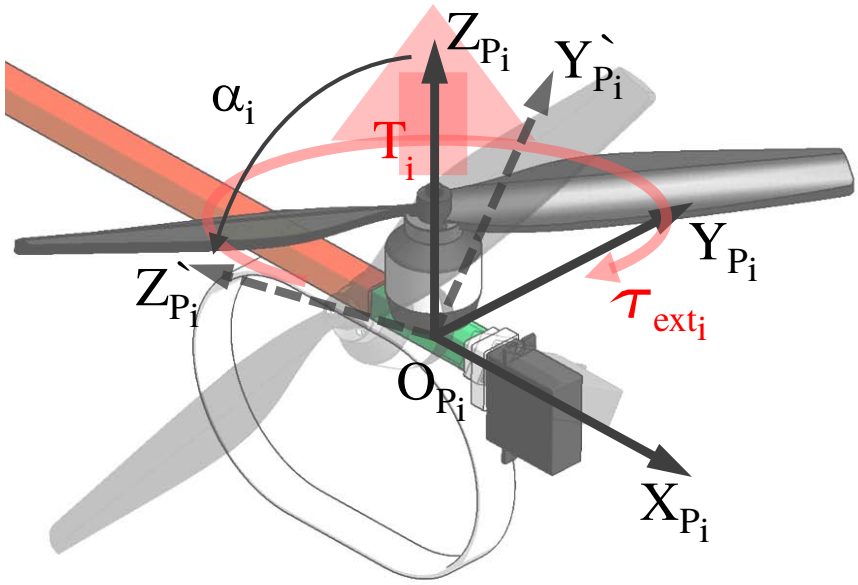

Figure 2.2: i-th tilting arm visualizing the body frame $\mathcal{F}_{P_i}$, the associated propeller thrust T_i, torque τ_{ext_i} and the propeller tilt angle α_i

frame. By denoting with $\alpha_i \in \mathbb{R}$ the propeller tilt angle about axis $\boldsymbol{X}_{P_i}$, it follows from Fig. 2.1 that[2]

$$^{B}\boldsymbol{R}_{P_i} = \boldsymbol{R}_Z\left((i-1)\frac{\pi}{2}\right)\boldsymbol{R}_X(\alpha_i), \qquad i = 1\dots 4.$$

Similarly, we also let

$$^{B}\boldsymbol{O}_{P_i} = \boldsymbol{R}_Z\left((i-1)\frac{\pi}{2}\right)\begin{bmatrix} L \\ 0 \\ 0 \end{bmatrix}, \qquad i = 1\dots 4$$

be the origin of the propeller frames $\mathcal{F}_{P_i}$ in the body frame with L being the distance of $\boldsymbol{O}_{P_i}$ from $\boldsymbol{O}_B$.

Summarizing, the quadrotor configuration is completely determined by the body position $\boldsymbol{p} = {}^{W}\boldsymbol{O}_B \in \mathbb{R}^3$ and orientation ${}^{W}\boldsymbol{R}_B$ in the world frame, and by the 4 tilt angles α_i specifying the propeller group orientations in the body frame (rotations about $\boldsymbol{X}_{P_i}$). We omit the propeller spinning angles about $\boldsymbol{Z}_{P_i}$ as configuration variables, although the propeller spinning velocities $\bar{w}_i$ about $\boldsymbol{Z}_{P_i}$ will be part of the system model (see next Sections).

2.2 Equations of motion

By exploiting standard techniques (e.g., Newton-Euler procedure), it is possible to derive a complete description of the quadrotor dynamic model by considering the forces/moments generated by the propeller motion, as well as any cross-coupling due to gyroscopic and inertial effects arising from the relative motion of the 5 bodies composing the quadrotor. As aerodynamic forces and torques, we will only consider those responsible for the quadrotor actuation and neglect any additional second-order effects/disturbances. Indeed, as discussed in the next Sect. 2.3, for the typical 'slow' flight regimes considered in this work, the propeller actuation forces and torques result significantly dominant w.r.t. other aerodynamic effects. We now discuss in detail the main conceptual steps needed to derive the quadrotor dynamical model.

[2]Throughout the following, $\boldsymbol{R}_X(\theta)$, $\boldsymbol{R}_Y(\theta)$, $\boldsymbol{R}_Z(\theta)$ will denote the canonical rotation matrixes about the $\boldsymbol{X}$, $\boldsymbol{Y}$, $\boldsymbol{Z}$ axes of angle θ, respectively.

To this end, let $\boldsymbol{\omega}_B \in \mathbb{R}^3$ be the angular velocity of the quadrotor body B expressed in the body frame[3], and consider the i-th propeller group P_i. The angular velocity of the i-th propeller (i.e., of $\mathcal{F}_{P_i}$) w.r.t. $\mathcal{F}_W$ and expressed in $\mathcal{F}_{P_i}$ is just

$$\boldsymbol{\omega}_{P_i} = {}^B\boldsymbol{R}_{P_i}^T \boldsymbol{\omega}_B + [\dot{\alpha}_i \; 0 \; \bar{w}_i]^T,$$

where $\dot{\alpha}_i$ is the tilting velocity about $\boldsymbol{X}_{P_i}$ and $\bar{w}_i \in \mathbb{R}$ the *spinning velocity* about $\boldsymbol{Z}_{P_i}$, both w.r.t. $\mathcal{F}_B$ (see Sect. 2.1). This results in an angular acceleration

$$\dot{\boldsymbol{\omega}}_{P_i} = {}^B\boldsymbol{R}_{P_i}^T \dot{\boldsymbol{\omega}}_B + {}^B\dot{\boldsymbol{R}}_{P_i}^T \boldsymbol{\omega}_B + [\ddot{\alpha}_i \; 0 \; \dot{\bar{w}}_i]^T.$$

By applying the Euler equations of motion, it follows that

$$\boldsymbol{\tau}_{P_i} = \boldsymbol{I}_{P_i} \dot{\boldsymbol{\omega}}_{P_i} + \boldsymbol{\omega}_{P_i} \times \boldsymbol{I}_{P_i} \boldsymbol{\omega}_{P_i} - \boldsymbol{\tau}_{ext_i}. \tag{2.1}$$

Here, $\boldsymbol{I}_{P_i} \in \mathbb{R}^{3\times3}$ is the (constant) symmetric and positive definite inertia matrix of the i-th propeller/rotor assembly approximated as an equivalent disc (the inertia of the tilting mechanism is supposed lumped into the main body B), and $\boldsymbol{\tau}_{ext_i}$ any external torque applied to the propeller. As usual, see e.g. Valavanis (2007), we assume presence of a counter-rotating torque about the $\boldsymbol{Z}_{P_i}$ axis caused by air drag and modeled as

$$\boldsymbol{\tau}_{ext_i} = [0 \; 0 \; -k_m \omega_{P_{i_Z}} |\omega_{P_{i_Z}}|]^T, \qquad k_m > 0 \tag{2.2}$$

with $\omega_{P_{i_Z}}$ being the third component of ω_{P_i}.

Let now

$$\boldsymbol{T}_{P_i} = [0 \; 0 \; k_f \bar{w}_i |\bar{w}_i|]^T, \qquad k_f > 0, \tag{2.3}$$

represent the i-th propeller force (thrust) along the $\boldsymbol{Z}_{P_i}$ axis and acting at ${}^B\boldsymbol{O}_{P_i}$ in $\mathcal{F}_B$. By considering the quadrotor body B and the torques generated by the four propellers P_i, one then obtains

$$\sum_{i=1}^{4} \left({}^B\boldsymbol{O}_{P_i} \times {}^B\boldsymbol{R}_{P_i} \boldsymbol{T}_{P_i} - {}^B\boldsymbol{R}_{P_i} \boldsymbol{\tau}_{P_i} \right) = \boldsymbol{I}_B \dot{\boldsymbol{\omega}}_B + \boldsymbol{\omega}_B \times \boldsymbol{I}_B \boldsymbol{\omega}_B, \tag{2.4}$$

with $\boldsymbol{I}_B \in \mathbb{R}^{3\times3}$ being the (constant) symmetric and positive definite Inertia matrix of B.

As for the translational dynamics, we assume for simplicity that the barycenter of each propeller group P_i coincides with $\boldsymbol{O}_{P_i}$. This allows us to neglect inertial effects on the

[3]In the following, we will assume that every quantity is expressed in its own frame, e.g., $\boldsymbol{\omega}_B = {}^B\boldsymbol{\omega}_B$.

propeller groups due to the quadrotor body acceleration in space. Therefore, by recalling that $\boldsymbol{p} = {}^{W}\boldsymbol{O}_{B}$ is the quadrotor body position in world frame, one has

$$m\ddot{\boldsymbol{p}} = m \begin{bmatrix} 0 \\ 0 \\ -g \end{bmatrix} + {}^{W}\boldsymbol{R}_{B} \sum_{i=1}^{4} {}^{B}\boldsymbol{R}_{P_i} \boldsymbol{T}_{P_i} \tag{2.5}$$

where m is the total mass of the quadrotor and propeller bodies and g the scalar gravitational acceleration of Earth.

Summarizing, equations (2.1)–(2.4)–(2.5) describe the rotational/translational dynamics of the quadrotor body and propeller groups. Note that the inputs of this model are the motor torques actuating the propeller tilting axes $\boldsymbol{X}_{P_i}$ and spinning axes $\boldsymbol{Z}_{P_i}$. These are denoted as $\tau_{\alpha_i} = \boldsymbol{\tau}_{P_i}^{T} \boldsymbol{X}_{P_i} \in \mathbb{R}$ and $\tau_{\bar{w}_i} = \boldsymbol{\tau}_{P_i}^{T} \boldsymbol{Z}_{P_i} \in \mathbb{R}$, $i = 1 \dots 4$, respectively, for a total of $4+4=8$ independent control torques (inputs). The propeller spinning velocities $\bar{w}_i$ (actuated by $\tau_{\bar{w}_i}$) will then generate the forces and torques affecting the translational/rotational motion of the quadrotor body B as a function of its current configuration, in particular of the tilting angles α_i actuated by τ_{α_i}. For the reader's convenience, Table 2.1 lists the main quantities introduced in this section.

2.3 Additional Aerodynamic Effects

The derivation of the most significant aerodynamic effects besides the already considered propeller torques and forces (2.2–2.3) can be obtained by considering momentum and blade element theory. In this section we will focus on the influence of the *hub force* $\boldsymbol{F}_{H_i}$ (a force perpendicular to the rotor shaft acting on the single blade elements and opposing the x-y velocity component of the i-th propeller group frame P_i) and of the *rolling moment* $\boldsymbol{\tau}_{R_i}$ (a torque around $\boldsymbol{X}_{P_i}$ caused by different thrust on the retreating and the advancing blade of the propeller). Figure 2.3 gives an illustration of these quantities, while Table 2.2 summarizes the main symbols introduced hereafter.

Let $(\dot{x}_{P_i}, \dot{y}_{P_i}, \dot{z}_{P_i}) = {}^{W}\boldsymbol{R}_{P_i}^{T}\, {}^{W}\dot{\boldsymbol{O}}_{P_i}$ be the velocity of the i-th propeller w.r.t. the world frame and expressed in the propeller frame $\mathcal{F}_{P_i}$. We define

$$V_i = \sqrt{\dot{x}_{P_i}^2 + \dot{y}_{P_i}^2}$$

Symbols	Definitions
$\mathcal{F}_W$	inertial world frame
$\mathcal{F}_B$	quadrotor body frame B
$\mathcal{F}_{P_i}$	i-th propeller group frame P_i
$\boldsymbol{p}$	position of B in $\mathcal{F}_W$
${}^W\boldsymbol{R}_B$	rotation matrix from $\mathcal{F}_B$ to $\mathcal{F}_W$
${}^B\boldsymbol{R}_{P_i}$	rotation matrix from $\mathcal{F}_{P_i}$ to $\mathcal{F}_B$
α_i	i-th propeller tilt angle about $\boldsymbol{X}_{P_i}$
$\bar{w}_i$	i-th propeller spinning velocity about $\boldsymbol{Z}_{P_i}$
$\boldsymbol{\omega}_B$	angular velocity of B in $\mathcal{F}_B$
$\boldsymbol{\tau}_{ext_i}$	i-th propeller air drag torque about $\boldsymbol{Z}_{P_i}$
$\boldsymbol{T}_i$	i-th propeller thrust along $\boldsymbol{Z}_{P_i}$
τ_{P_i}	motor torque actuating $\boldsymbol{X}_{P_i}$
$\tau_{\bar{\omega}_i}$	motor torque actuating $\boldsymbol{Z}_{P_i}$
m	total mass of the holocopter
$\boldsymbol{I}_P$	inertia of the i-th propeller group P_i
$\boldsymbol{I}_B$	inertia of the quadrotor body B
k_f	propeller thrust coefficient
k_m	propeller drag coefficient
L	distance of $\mathcal{F}_{P_i}$ from $\mathcal{F}_B$
g	gravitational acceleration of Earth

Table 2.1: Main quantities and definitions for the holocopter dynamic model

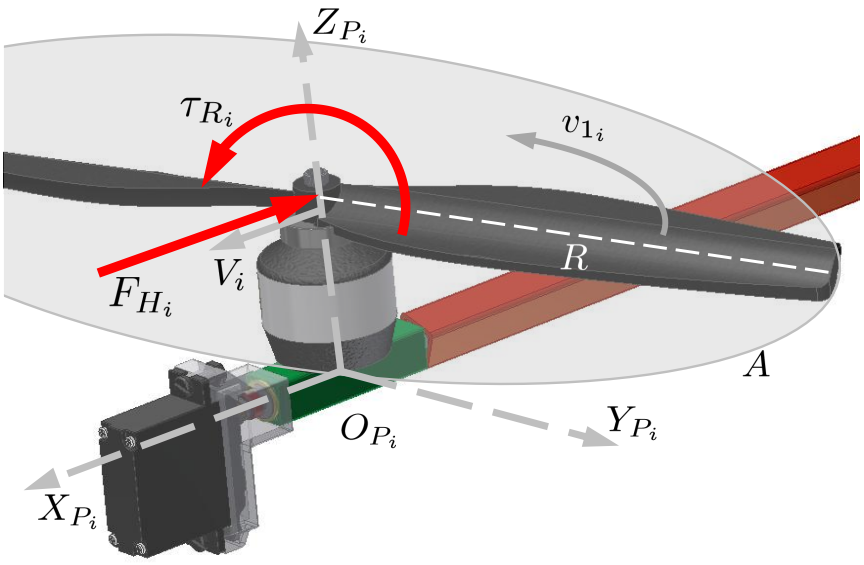

Figure 2.3: Visualization of hub force F_{H_i} and rolling moment τ_{R_i} acting on a single blade

as the sideways velocity of the i-th propeller in propeller group frame. Momentum theory models the generated thrust of a single propeller as $\|\boldsymbol{T}_{P_i}\| = 2\rho A v_{1_i}\sqrt{V_i^2 + v_{1_i}^2}$, with v_{1_i} being the so-called i-th propeller inflow velocity (Stepniewski and Keys (1984)). Solving for v_{1_i} we get

$$v_{1_i} = \sqrt{\frac{V_i^2}{2} + \sqrt{\left(\frac{V_i^2}{2}\right)^2 + \left(\frac{\|\boldsymbol{T}_{P_i}\|}{2\rho A}\right)^2}} \tag{2.6}$$

where ρ is the air density and A the rotor area.

Following the assumptions and simplifications of Fay. G (2001), the magnitude of the hub force $\boldsymbol{F}_{H_i}$ can then be modeled as

$$\begin{cases} \|\boldsymbol{F}_{H_i}\| &= C_{H_i}\rho A(\bar{w}_i R)^2 \\ \dfrac{C_{H_i}}{\sigma a} &= \dfrac{1}{4a}\mu_i \bar{C}_d + \dfrac{1}{4}\lambda_i\mu_i(\theta_0 - \dfrac{\theta_{tw}}{2}) \end{cases} \tag{2.7}$$

where

$$\lambda_i = \frac{v_{1_i} - \dot{z}_{P_i}}{\bar{w}_i R}, \quad \mu_i = \frac{V_i}{\bar{w}_i R}, \tag{2.8}$$

and R is the propeller radius, σ the solidity ratio, a the lift slop, $\bar{C}_d$ the average drag coefficient, θ_0 the pitch of incidence, and θ_{tw} the twist pitch. One can similarly model the magnitude of the rolling moment $\boldsymbol{\tau}_{R_i}$ acting on P_i and due to the different lift of the

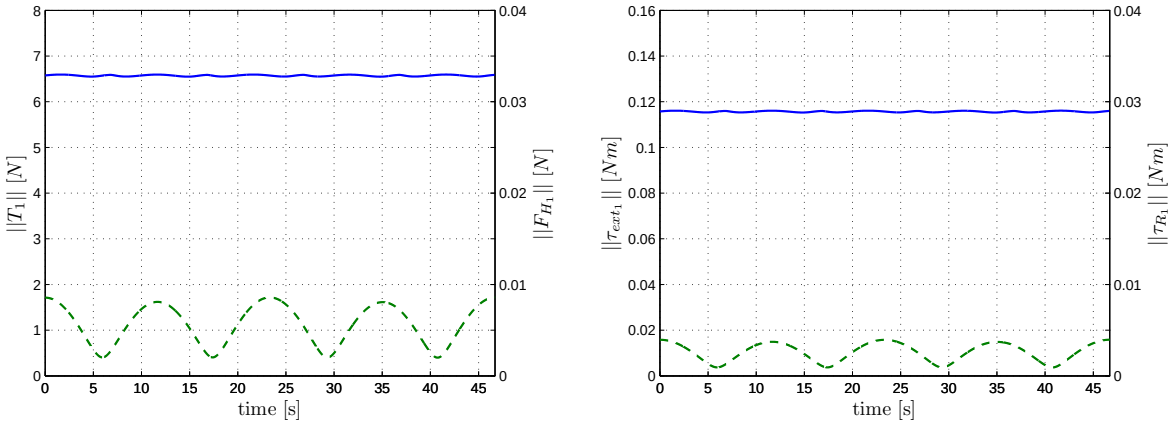

(a) (b)

Figure 2.4: (a) Solid line: Thrust $\|\boldsymbol{T}_{P_1}\|$ in $\mathcal{F}_{P_1}$ (left y-axis), dashed lines: hub force $\|F_{H_1}\|$ in $\mathcal{F}_{P_1}$ (right y-axis); (b) Solid line: Drag $\|\boldsymbol{\tau}_{ext_1}\|$ in $\mathcal{F}_{P_1}$ (left y-axis), dashed line: rolling moment $\|\tau_{R_1}\|$ in $\mathcal{F}_{P_1}$ (right y-axis). Note the *different scales* of the y-axes in both plots

retrieving and the advancing blade of the propeller as

$$\begin{cases} \|\boldsymbol{\tau}_{R_i}\| &= C_{R_m i}\rho A(\bar{w}_i R)^2 R \\ \dfrac{C_{R_m i}}{\sigma a} &= -\mu_i(\frac{1}{6}\theta_0 - \frac{1}{8}\theta_{tw} - \frac{1}{8}\lambda_i) \end{cases} . \tag{2.9}$$

In order to assess the influence of these aerodynamic effects, we compared them against the thrust $\boldsymbol{T}_{P_i}$ and torque $\boldsymbol{\tau}_{ext_i}$ of a single propeller during the simulated trajectory described in Sect. 5.1.2 and relying, for the various parameters, on the physical properties of our prototype and on values taken from literature. The trajectory consists of a horizontal eight-shape planar curve with a superimposed sinusoidal rotation about the body $\boldsymbol{Y}_B$ axis, and has been chosen as being representative of the typical operational regimes of our prototype. The results are shown in Fig. 2.4: as clear from the plots, it is $\|\boldsymbol{T}_{P_i}\|/\|\boldsymbol{F}_{H_i}\| \simeq 600$ and $\|\boldsymbol{\tau}_{ext_i}\|/\|\boldsymbol{\tau}_{R_i}\| \simeq 30$ (note the two *different scales* of the y-axes in both plots). This then confirms the minor significance of these (neglected) second-order aerodynamics effects w.r.t. the propeller actuation forces and torques (2.2–2.3) which are instead taken into account in the holocopter dynamical model. As for the significance of blade flapping and induced drag (typically modeled as *first-order* contributions, see Mahony et al. (2012)), a similar analysis showed an even smaller effect w.r.t. the above-mentioned second-order

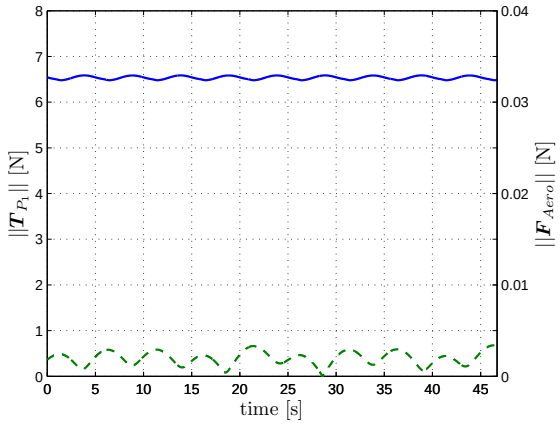

Figure 2.5: Solid blue line: thrust $\|\boldsymbol{T}_{P_1}\|$ while following the 8-shape trajectory as in Sect. II.C; dashed green line: norm $\|\boldsymbol{F}_{Aero}\|$ of the first-order exogenouse force from ref. [3].

forces and torques in the same flying regimes (see figure 2.5). Therefore, these first-order terms were also neglected in the holocopter model.

Symbols	Definitions
$\rho\ [kg/m^3]$	Air density
$A\ [m^2]$	Propeller disk area
$v_1\ [m/s]$	Propeller inflow velocity
$\boldsymbol{F}_H\ [N]$	Hub force
$\boldsymbol{\tau}_R\ [Nm]$	Rolling moment
$R\ [m]$	Propeller radius
a	Lift slope
$\sigma\ [rad^{-1}]$	Solidity ratio
$\bar{C}_d$	Average drag coefficient
λ_i	Inflow ratio
μ_i	Rotor advance ratio
$\theta_0\ [rad]$	Pitch of incidence
$\theta_{tw}\ [rad]$	Twist pitch
$\dot{x}_{P_i}$, $\dot{y}_{P_i}$, $\dot{z}_{P_i}\ [m/s]$	Velocity of the propeller w.r.t. ground

Table 2.2: Symbols and Definitions describing the main aerodynamic effects on a single propeller

Chapter 3

Motion Control of the Holocopter

This chapter has been mainly reproduced from an article published in ICRA 2012: Ryll et al. (2012)

We start with some preliminary considerations: the dynamic model illustrated in the previous Section is useful for simulation purposes as it captures the main effects of the quadrotor motion in space (apart from unmodeled aerodynamics forces and torques). Some simplifications are however useful for transforming it into a 'reduced model' more suited to control design. First, as in many practical situations, we assume that the motors actuating the tilting/spinning axes are implementing a fast high-gain local controller able to impose desired speeds $w_{\alpha_i} = \dot{\alpha}_i$ and $\bar{w}_i$ with negligible transients[1]. This allows to neglect the motor dynamics, and to consider w_{α_i} and $\bar{w}_i$, $i = 1 \dots 4$, as (virtual) control inputs in place of the motor torques τ_{α_i} and $\tau_{\bar{w}_i}$. Second, in this simplified model we also neglect the internal gyroscopic/inertial effects by considering them as second-order disturbances to be rejected by the controller[2]. We note that the validity of these assumptions will be discussed in Sect. 5.1 where the proposed controller will be tested against the *complete dynamic model* of Sect. 2 representing the actual dynamics of the quadrotor.

Let us then define $\boldsymbol{\alpha} = [\alpha_1 \dots \alpha_4]^T \in \mathbb{R}^4$, $\boldsymbol{w}_\alpha = [w_{\alpha_1} \dots w_{\alpha_4}]^T \in \mathbb{R}^4$ and $\boldsymbol{w} = [\bar{w}_1|\bar{w}_1| \dots \bar{w}_4|\bar{w}_4|]^T \in \mathbb{R}^4$. Note that the elements of vector $\boldsymbol{w}$ are the signed squares of the spinning velocities $\bar{w}_i$, as the torques and forces in (2.2)–(2.3) are a (approx. linear)

[1] For instance, in the standard quadrotor case, the spinning velocities $\bar{w}_i$ are usually taken as control inputs.

[2] Obviously, this assumption holds as long as the inertia of the propeller group is small w.r.t. the main holocopter body.

function of these quantities. Therefore, in the following analysis, $w_i = \bar{w}_i|\bar{w}_i|$ will be considered as input 'spinning velocity' of the i-th propeller, with the understanding that one can always recover the actual speed $\bar{w}_i = \text{sign}(w_i)\sqrt{|w_i|}$. Under the stated assumptions, the quadrotor dynamic model can be simplified into

$$\begin{cases} \ddot{\boldsymbol{p}} &= \begin{bmatrix} 0 \\ 0 \\ -g \end{bmatrix} + \frac{1}{m} {}^W\boldsymbol{R}_B \boldsymbol{F}(\boldsymbol{\alpha})\boldsymbol{w} \\ \dot{\boldsymbol{\omega}}_B &= \boldsymbol{I}_B^{-1}\boldsymbol{\tau}(\boldsymbol{\alpha})\boldsymbol{w} \\ \dot{\boldsymbol{\alpha}} &= \boldsymbol{w}_\alpha \\ {}^W\dot{\boldsymbol{R}}_B &= {}^W\boldsymbol{R}_B[\boldsymbol{\omega}_B]_\wedge \end{cases} \tag{3.1}$$

with $[\cdot]_\wedge$ being the usual map taking a vector $\boldsymbol{a} \in \mathbb{R}^3$ into the associated skew-symmetric matrix $[\boldsymbol{a}]_\times \in so(3)$, and

$$\boldsymbol{F}(\boldsymbol{\alpha}) = \begin{bmatrix} 0 & -k_f s_2 & 0 & k_f s_4 \\ -k_f s_1 & 0 & k_f s_3 & 0 \\ k_f c_1 & -k_f c_2 & k_f c_3 & -k_f c_4 \end{bmatrix},$$

$$\boldsymbol{\tau}(\boldsymbol{\alpha}) = \begin{bmatrix} 0 & -Lk_f c_2 - k_m s_2 & 0 & Lk_f c_4 + k_m s_4 \\ -Lk_f c_1 + k_m s_1 & 0 & Lk_f c_3 - k_m s_3 & 0 \\ -Lk_f s_1 - k_m c_1 & Lk_f s_2 - k_m c_2 & -Lk_f s_3 - k_m c_3 & Lk_f s_4 - k_m c_4 \end{bmatrix} \tag{3.2}$$

the 3×4 input coupling matrixes ($s_i = \sin(\alpha_i)$ and $c_i = \cos(\alpha_i)$). Note that input $\boldsymbol{w}$ appears linearly in (3.1) as expected. The subsequent control design is then performed on the simplified model (3.1–3.2).

3.1 Control Design

The control problem considered in this thesis is an output tracking problem: how to track, with the available inputs, a desired (and arbitrary) trajectory $(\boldsymbol{p}_d(t), \boldsymbol{R}_d(t)) \in \mathbb{R}^3 \times SO(3)$

for the body position $\boldsymbol{p}$ and orientation ${}^{W}\boldsymbol{R}_{B}$ taken as output functions. We note again that this problem is clearly ill-posed for a *standard* quadrotor with fixed propellers because of its underactuation. However, the chosen *overactuated* design of the holocopter (8 independent control inputs) can guarantee full controllability over the position/orientation of its main body as it is shown in the following developments.

As in many output tracking problems, a possible solution is to resort to output feedback linearization techniques (either static or dynamic), see Isidori (1995) for a detailed treatment. To this end, we rewrite the first two rows of (3.1) as

$$\begin{aligned}\begin{bmatrix}\ddot{\boldsymbol{p}}\\ \dot{\boldsymbol{\omega}}_B\end{bmatrix} =& \begin{bmatrix}\begin{bmatrix}0\\0\\-g\end{bmatrix}\\ \boldsymbol{0}\end{bmatrix} + \begin{bmatrix}\frac{1}{m}{}^{W}\boldsymbol{R}_B & \boldsymbol{0}\\ \boldsymbol{0} & \boldsymbol{I}_B^{-1}\end{bmatrix}\begin{bmatrix}\boldsymbol{F}(\boldsymbol{\alpha}) & \boldsymbol{0}\\ \boldsymbol{\tau}(\boldsymbol{\alpha}) & \boldsymbol{0}\end{bmatrix}\begin{bmatrix}\boldsymbol{w}\\ \boldsymbol{w}_\alpha\end{bmatrix}\\ =& \boldsymbol{f} + \boldsymbol{J}_R\begin{bmatrix}\bar{\boldsymbol{J}}_\alpha(\boldsymbol{\alpha}) & \boldsymbol{0}\end{bmatrix}\begin{bmatrix}\boldsymbol{w}\\ \boldsymbol{w}_\alpha\end{bmatrix} = \boldsymbol{f} + \boldsymbol{J}_R\boldsymbol{J}_\alpha(\boldsymbol{\alpha})\begin{bmatrix}\boldsymbol{w}\\ \boldsymbol{w}_\alpha\end{bmatrix}\\ =& \boldsymbol{f} + \boldsymbol{J}(\boldsymbol{\alpha})\begin{bmatrix}\boldsymbol{w}\\ \boldsymbol{w}_\alpha\end{bmatrix},\end{aligned} \tag{3.3}$$

where $\boldsymbol{f} \in \mathbb{R}^6$ is a constant drift vector, $\bar{\boldsymbol{J}}(\boldsymbol{\alpha}) \in \mathbb{R}^{6\times 4}$, $\boldsymbol{J}_R \in \mathbb{R}^{6\times 6}$, and the 6×8 matrix $\boldsymbol{J}(\boldsymbol{\alpha})$ will be referred to as the *output Jacobian*. When $\rho_J = \operatorname{rank}(\boldsymbol{J}(\boldsymbol{\alpha})) = 6$, it is always possible to statically feedback linearize (3.3) by means of the law

$$\begin{bmatrix}\boldsymbol{w}\\ \boldsymbol{w}_\alpha\end{bmatrix} = \boldsymbol{K}(\boldsymbol{\alpha})\left(-\boldsymbol{f} + \begin{bmatrix}\ddot{\boldsymbol{p}}_r\\ \dot{\boldsymbol{\omega}}_r\end{bmatrix}\right) \tag{3.4}$$

where $\boldsymbol{K}(\boldsymbol{\alpha})$ is a generalized inverse of $\boldsymbol{J}(\boldsymbol{\alpha})$, e.g., the pseudoinverse $\boldsymbol{J}^{\dagger}(\boldsymbol{\alpha})$, and $[\ddot{\boldsymbol{p}}_r^T\ \dot{\boldsymbol{\omega}}_r^T]^T \in \mathbb{R}^6$ an arbitrary reference linear/angular acceleration vector to be imposed to the output dynamics in (3.1).

This solution is, however, not viable in the case under consideration. Indeed, $\rho_J = \operatorname{rank}(\boldsymbol{J}) = \operatorname{rank}(\boldsymbol{J}_R\boldsymbol{J}_\alpha) = \operatorname{rank}(\boldsymbol{J}_\alpha)$ since $\boldsymbol{J}_R$ is a nonsingular square matrix. Furthermore, $\rho_J = \operatorname{rank}(\boldsymbol{J}_\alpha) = \operatorname{rank}(\bar{\boldsymbol{J}}_\alpha) \leq 4 < 6$ because of the structural null matrix $\boldsymbol{0} \in \mathbb{R}^{6\times 4}$ in matrix $\boldsymbol{J}_\alpha(\boldsymbol{\alpha})$ weighting the inputs $\boldsymbol{w}_\alpha$. Presence of this null matrix is due to the fact that inputs $\boldsymbol{w}_\alpha$ affect the output dynamics at a higher differential level compared to

inputs $\boldsymbol{w}$. Therefore, a direct inversion at the acceleration level is bound to exploit only inputs $\boldsymbol{w}$ resulting in a loss of controllability for the system. Intuitively, the instantaneous linear/angular acceleration of the quadrotor body is directly affected by the propeller speeds $\boldsymbol{w}$ and tilting configuration $\boldsymbol{\alpha}$ (thanks to the dependence in $\bar{\boldsymbol{J}}_\alpha(\boldsymbol{\alpha})$), but *not* by $\dot{\boldsymbol{\alpha}} = \boldsymbol{w}_\alpha$, i.e., the tilting velocities[3].

A possible way to circumvent these difficulties is to resort to a *dynamic* output linearization scheme and seek to invert the input-output map at a higher differential level where inputs $\boldsymbol{w}_\alpha$ will explicitly appear. This can be achieved as follows: expanding the term $\bar{\boldsymbol{J}}_\alpha(\boldsymbol{\alpha})\boldsymbol{w}$ in (3.3) as

$$\bar{\boldsymbol{J}}_\alpha(\boldsymbol{\alpha})\boldsymbol{w} = \sum_{i=1}^{4} \bar{\boldsymbol{j}}_i(\boldsymbol{\alpha}) w_i,$$

and noting that

$$\frac{\mathrm{d}\bar{\boldsymbol{J}}_\alpha(\boldsymbol{\alpha})\boldsymbol{w}}{\mathrm{d}t} = \bar{\boldsymbol{J}}_\alpha(\boldsymbol{\alpha})\dot{\boldsymbol{w}} + \sum_{i=1}^{4} \frac{\partial \bar{\boldsymbol{j}}_i(\boldsymbol{\alpha})}{\partial \boldsymbol{\alpha}} \boldsymbol{w}_\alpha w_i,$$

differentiation of (3.3) w.r.t. time yields

$$\begin{aligned}
\begin{bmatrix} \ddot{\boldsymbol{p}} \\ \dot{\boldsymbol{\omega}}_B \end{bmatrix} &= \boldsymbol{J}_R \bar{\boldsymbol{J}}_\alpha(\boldsymbol{\alpha})\dot{\boldsymbol{w}} + \boldsymbol{J}_R \sum_{i=1}^{4} \frac{\partial \bar{\boldsymbol{j}}_i(\boldsymbol{\alpha})}{\partial \boldsymbol{\alpha}} \boldsymbol{w}_\alpha w_i + \dot{\boldsymbol{J}}_R \bar{\boldsymbol{J}}_\alpha(\boldsymbol{\alpha})\boldsymbol{w} \\
&= \boldsymbol{J}_R \begin{bmatrix} \bar{\boldsymbol{J}}_\alpha(\boldsymbol{\alpha}) & \sum_{i=1}^{4} \frac{\partial \bar{\boldsymbol{j}}_i(\boldsymbol{\alpha})}{\partial \boldsymbol{\alpha}} w_i \end{bmatrix} \begin{bmatrix} \dot{\boldsymbol{w}} \\ \boldsymbol{w}_\alpha \end{bmatrix} + \qquad (3.5) \\
&\quad \begin{bmatrix} \frac{{}^W\dot{\boldsymbol{R}}_B}{m} \boldsymbol{F}(\boldsymbol{\alpha})\boldsymbol{w} \\ \boldsymbol{0} \end{bmatrix} \\
&= \boldsymbol{J}_R \boldsymbol{J}'_\alpha(\boldsymbol{\alpha},\, \boldsymbol{w}) \begin{bmatrix} \dot{\boldsymbol{w}} \\ \boldsymbol{w}_\alpha \end{bmatrix} + \boldsymbol{b}(\boldsymbol{\alpha},\, \boldsymbol{w},\, \boldsymbol{\omega}_B) \\
&= \boldsymbol{A}(\boldsymbol{\alpha}, \boldsymbol{w}) \begin{bmatrix} \dot{\boldsymbol{w}} \\ \boldsymbol{w}_\alpha \end{bmatrix} + \boldsymbol{b}(\boldsymbol{\alpha},\, \boldsymbol{w},\, \boldsymbol{\omega}_B) \qquad (3.6)
\end{aligned}$$

where the new input $\dot{\boldsymbol{w}}$ is the dynamic extension of the former (and actual) input $\boldsymbol{w}$ obtained by adding 4 integrators on its channel[4].

[3] It is interesting to note that this inhomogeneity in the differential levels at which inputs are affecting the output dynamics is not a specificity of the system at hand. As an example, the same structural property is also present in other robotic structures such as mobile manipulators with steering wheels see (De Luca et al. (2010)) where the role of $\boldsymbol{w}_\alpha$ is played by the wheel steering velocities.

[4] By means of this dynamic extensions, vector $\boldsymbol{w}$ becomes an internal state of the controller.

We note that the new 6×8 input-output decoupling matrix $\boldsymbol{A}(\boldsymbol{\alpha}, \boldsymbol{w})$ consists of two column blocks: while the first block $\boldsymbol{J}_R\bar{\boldsymbol{J}}_\alpha(\boldsymbol{\alpha})$ is exactly the first block of the former output Jacobian $\boldsymbol{J}(\boldsymbol{\alpha})$, the second block is *not* a null matrix as in the previous case. Rather, a new set of 4 columns, weighting inputs $\boldsymbol{w}_\alpha$, are now present and contributing to the rank of matrix $\boldsymbol{A}$. Furthermore, it is $\boldsymbol{A}(\boldsymbol{\alpha}, \boldsymbol{0}) = \boldsymbol{J}(\boldsymbol{\alpha})$ and $\rho_A = \text{rank}(\boldsymbol{A}) = 6$ as long as $w_i \neq 0$, $i = 1 \dots 4$: in other words, *full rankness* of matrix $\boldsymbol{A}$ can always be ensured by preventing the propellers from stopping their spinning motion. The proof can be found in the appendix A.1. The next Section 3.2 proposes a strategy able to meet this requirement.

With $\rho_A = \text{rank}(\boldsymbol{A}) = 6$ system (3.5) can be inverted by the law

$$\begin{bmatrix} \dot{\boldsymbol{w}} \\ \boldsymbol{w}_\alpha \end{bmatrix} = \boldsymbol{A}^\dagger \left(\begin{bmatrix} \dddot{\boldsymbol{p}}_r \\ \ddot{\boldsymbol{\omega}}_r \end{bmatrix} - \boldsymbol{b} \right) + (\mathbf{I}_8 - \boldsymbol{A}^\dagger \boldsymbol{A})\boldsymbol{z}, \tag{3.7}$$

with $\mathbf{I}_N$ being the identity matrix of dimension N and $\boldsymbol{A}^\dagger \in \mathbb{R}^{8\times 6}$ denoting the Moore-Penrose pseudo-inverse of matrix $\boldsymbol{A}$, in order to achieve full input-output linearization

$$\begin{bmatrix} \dddot{\boldsymbol{p}} \\ \ddot{\boldsymbol{\omega}}_B \end{bmatrix} = \begin{bmatrix} \dddot{\boldsymbol{p}}_r \\ \ddot{\boldsymbol{\omega}}_r \end{bmatrix}. \tag{3.8}$$

Vector $\boldsymbol{z} \in \mathbb{R}^8$ in (3.7) is an additional free quantity projected onto the 2-dimensional null-space of $\boldsymbol{A}$ whose use will be detailed in the next Section 3.2. We note that presence of a 2-dimensional null space for matrix $\boldsymbol{A}$ is a direct (and expected) consequence of the *actuation redundancy* of degree 2 of the considered holocopter (8 control inputs for 6 controlled dofs). We are now in position for solving the control problem stated at the beginning of the Section, i.e., asymptotic tracking of a desired trajectory $(\boldsymbol{p}_d(t), \boldsymbol{R}_d(t))$.

Assuming now $\boldsymbol{p}_d(t) \in \bar{\mathcal{C}}^3$, it is then sufficient to set in (3.8)

$$\dddot{\boldsymbol{p}}_r = \dddot{\boldsymbol{p}}_d + \boldsymbol{K}_{p_1}(\ddot{\boldsymbol{p}}_d - \ddot{\boldsymbol{p}}) + \boldsymbol{K}_{p_2}(\dot{\boldsymbol{p}}_d - \dot{\boldsymbol{p}}) + \boldsymbol{K}_{p_3}(\boldsymbol{p}_d - \boldsymbol{p}) \tag{3.9}$$

for obtaining exponential and decoupled convergence of the position error to $\boldsymbol{0}$ as long as the (diagonal) positive definite gain matrixes $\boldsymbol{K}_{p_1}$, $\boldsymbol{K}_{p_2}$, $\boldsymbol{K}_{p_3}$ define Hurwitz polynomials. As for the stabilization of the orientation tracking error, several choices are possible depending on the particular parameterization chosen for the rotation matrix $\boldsymbol{R}$. Besides the usual Euler angles (with their inherent singularity issues), a convenient possibility is to resort to an orientation error term directly defined on $SO(3)$, as shown in Mellinger and Kumar

(2011) and Lee et al. (2010). Assume, as before, that $\boldsymbol{R}_d(t) \in \bar{\mathcal{C}}^3$ and let $\boldsymbol{\omega}_d = [\boldsymbol{R}_d^T \dot{\boldsymbol{R}}_d]_\vee$, where $[\cdot]_\vee$ represents the inverse map from $so(3)$ to $\mathbb{R}^3$. By defining the orientation error as

$$\boldsymbol{e}_R = \frac{1}{2}[{}^W\boldsymbol{R}_B^T \boldsymbol{R}_d - \boldsymbol{R}_d^{TW}\boldsymbol{R}_B]_\vee \tag{3.10}$$

the choice

$$\ddot{\boldsymbol{\omega}}_r = \ddot{\boldsymbol{\omega}}_d + \boldsymbol{K}_{\omega_1}(\dot{\boldsymbol{\omega}}_d - \dot{\boldsymbol{\omega}}_B) + \boldsymbol{K}_{\omega_2}(\boldsymbol{\omega}_d - \boldsymbol{\omega}_B) + \boldsymbol{K}_{\omega_3}\boldsymbol{e}_R \tag{3.11}$$

in (3.8) yields an exponential convergence for the orientation tracking error to $\mathbf{0}$ as desired, provided that the (diagonal) gain matrixes $\boldsymbol{K}_{\omega_1}$, $\boldsymbol{K}_{\omega_2}$, $\boldsymbol{K}_{\omega_3}$ define a Hurwitz polynomial.

3.2 Optimization of Additional Criteria

As a final step, we now discuss how to exploit the 2-dimensional actuation redundancy of the holocopter by exploiting vector $\boldsymbol{z}$ in (3.7).

Being projected onto the null space of $\boldsymbol{A}$, vector $\boldsymbol{z}$ does not produce actions interfering with the output tracking objective and can thus be exploited to fulfill additional tasks. In our case, a first mandatory requirement is to keep $\rho_A = 6$ at all times for avoiding singularities of the decoupling matrix $\boldsymbol{A}$ in (3.7). As explained, this objective can be easily met by ensuring $\boldsymbol{w} \neq \mathbf{0}$. Likewise another important requirement is to minimize the norm of $\boldsymbol{w}$ in order to reduce the energy consumption during flight since, for instance, the air drag torques $\boldsymbol{\tau}_{ext_i}$ in (2.2) are always performing a dissipative work against w_i.

A possible cost function $H(\boldsymbol{w})$ taking into account these two competing objectives is

$$H(\boldsymbol{w}) = \sum_{i=1}^{4} h(w_i)$$

with

$$h(w_i) = \begin{cases} k_{h_1} \tan^2(\gamma_1 |w_i| + \gamma_2) & w_{min} < |w_i| \leq w_{rest} \\ k_{h_2}(|w_i| - w_{rest})^2 & |w_i| > w_{rest} \end{cases}, \tag{3.12}$$

$\gamma_1 = \frac{\pi}{2(w_{rest} - w_{min})}$, $\gamma_2 = -\gamma_1 w_{rest}$, and $k_{h_1} > 0$, $k_{h_2} > 0$ suitable scalar gains. Here, $w_{min} > 0$ represents a minimum value for the propeller spinning velocities and $w_{rest} > w_{min}$ a suitable 'rest' speed. Furthermore, functions $h_i(w_i)$ are such that $h_i(w_i) \to \infty$ if either $|w_i| \to w_{min}$ or $|w_i| \to \infty$, and have a unique minimum (with continuous derivative) at w_{rest}. As for the placement of w_{rest}, in our implementation we chose

$$w_{rest} = \left(\frac{mg}{4k_f}\right), \tag{3.13}$$

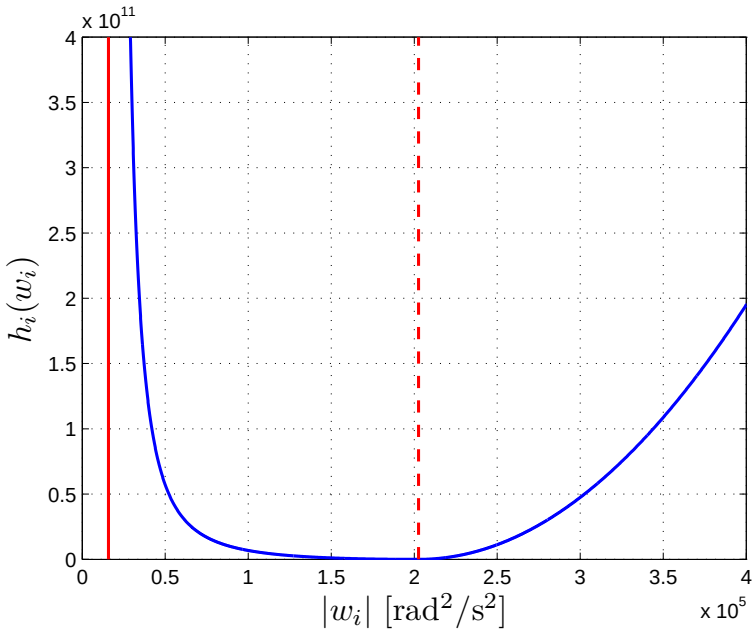

Figure 3.1: Example of a function $h_i(w_i)$ with $\bar{w}_{min} = 126$ [rad/s] (solid red vertical line), $\bar{w}_{rest} = 450$ [rad/s] (dashed red vertical line). Note that $h_i(w_i) \to \infty$ as $|w_i| \to w_{min}$ or $|w_i| \to \infty$, and that $h_i(w_i)$ has a unique minimum at w_{rest} with continuous derivative

that is, the (squared) spinning velocity needed by each propeller to hover.

An illustrative example for $h_i(w_i)$ with $w_{min} = 126^2$ [rad^2/s^2] and $w_{rest} = 450^2$ [rad^2/s^2] is shown in Fig. 3.1 (these values correspond to the ones used for the motor propeller combination of our holocopter prototype).

Minimization of $H(\boldsymbol{w})$, compatibly with the output tracking task, is then obtained by setting in (3.7)

$$\boldsymbol{z} = -k_H \begin{bmatrix} \nabla_{\boldsymbol{w}} H(\boldsymbol{w}) \\ \\ \mathbf{0} \end{bmatrix} \tag{3.14}$$

with $k_H > 0$ being a suitable step size. Note that, as a byproduct, this choice will also result in a beneficial 'velocity damping'-like action on the states $\boldsymbol{w}$ as, e.g., described in De Luca et al. (1992). We finally note that additional optimization actions could be embedded in vector $\boldsymbol{z}$, for instance by concurrently minimizing a second cost function $H_\alpha(\boldsymbol{\alpha})$ representing constraints on the range of the tilting angles $\boldsymbol{\alpha}$. Here a task specific optimization might be an interesting extension in this case the downwash of the propeller could be redirected away from an approximated target.

3.2.1 Dynamic adaptation of w_{rest}

The optimization as introduced in Sect. 3.2 guarantees a minimum energy consumption under a non-dynamic flight regime ($\ddot{\boldsymbol{p}} = 0$). In this case the internal forces are minimized. Under a dynamic fight regime ($\ddot{\boldsymbol{p}} \neq \mathbf{0}$) this is not given as the constant value of w_{rest} is determined as in (3.13), which is the minimum value for hovering condition but not the minimum value for a desired acceleration $\ddot{\boldsymbol{p}}$. Therefore the determination of the term w_{rest} can be extended by a dynamical term describing the currently desired vertical acceleration

$$w_{rest} = \begin{cases} \left(\frac{m}{4k_f}(g + \ddot{p}_z)\right) & k_s w_{min} \leq w_{rest} \\ k_s w_{min} = w_{rest} & k_s w_{min} > w_{rest} \end{cases}, \tag{3.15}$$

with $\ddot{p}_z$ being the z-component of the desired acceleration $\ddot{\boldsymbol{p}}_d$ in (3.9) and k_s being a safety margin to not let w_{min} and w_{rest} coincide (her $k_s = 1.1$ is used). Figure 3.2 shows the different behavior of the holocopter under a constant and a dynamic control of w_{rest}. Figure 3.2 (a) shows the desired trajectory for the vertical position, velocity and acceleration while all other values remain constant (position in x and y and orientation). Figure 3.2 (b) shows the internal forces under the two different regimes. The summed norm of the internal forces increases during the vertical acceleration in the case of a constant w_{rest} (blue line) while it remains almost 0 N in the case of a dynamic w_{rest} (red line).

3.3 Final Considerations

We conclude the section by noting that the position/orientation feedback terms in (3.9)–(3.11) require a measurement of the holocopter

1. position $\boldsymbol{p}$ and orientation ${}^{W}\boldsymbol{R}_{B}$;
2. linear velocity $\dot{\boldsymbol{p}}$ and angular velocity $\boldsymbol{\omega}_B$;
3. linear acceleration $\ddot{\boldsymbol{p}}$ and angular acceleration $\dot{\boldsymbol{\omega}}_B$.

Availability of the quantities in items 1–2 is a standard requirement for any UAV flight control scheme (see also the next Sect. 4.1.3), while measurement of the linear/angular accelerations of item 3 can pose some challenges in real-world scenarios because of the typical

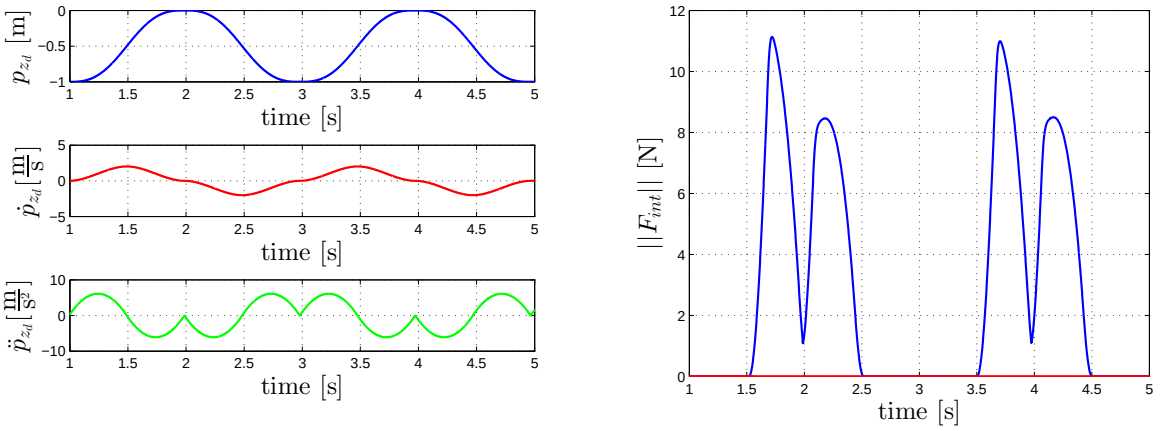

(a) (b)

Figure 3.2: (a): The desired trajectory is a movement along the z axis. The position in x and y and the orientation remain constant. (b): Summed norm of the internal forces: blue - constant w_{rest}, red - dynamic w_{rest}

high noise level of these signals when obtained from onboard sensors (e.g., accelerometers) or numerical differentiation of velocity-like quantities.

As an alternative, one can also exploit the holocopter model to evaluate the linear/angular acceleration ($\ddot{\boldsymbol{p}}$, $\dot{\boldsymbol{\omega}}_B$) in terms of sole velocity measurements (vector $\boldsymbol{w}$) since, from (3.3), it follows that

$$\begin{bmatrix} \ddot{\boldsymbol{p}} \\ \dot{\boldsymbol{\omega}}_B \end{bmatrix} = \boldsymbol{f} + \boldsymbol{J}_R \bar{\boldsymbol{J}}_\alpha(\boldsymbol{\alpha})\boldsymbol{w}. \tag{3.16}$$

Obviously this possibility assumes a good knowledge of the model parameters and of the system state: The practicability of this assumption is shown in figure 3.3 where measured and estimated values are plotted against each other. The simulation and experimental results of Sects. 5–6 are as well conducted by relying on (3.16) for obtaining ($\ddot{\boldsymbol{p}}$, $\dot{\boldsymbol{\omega}}_B$), and will thus confirm the appropriateness of this assumption for our setup.

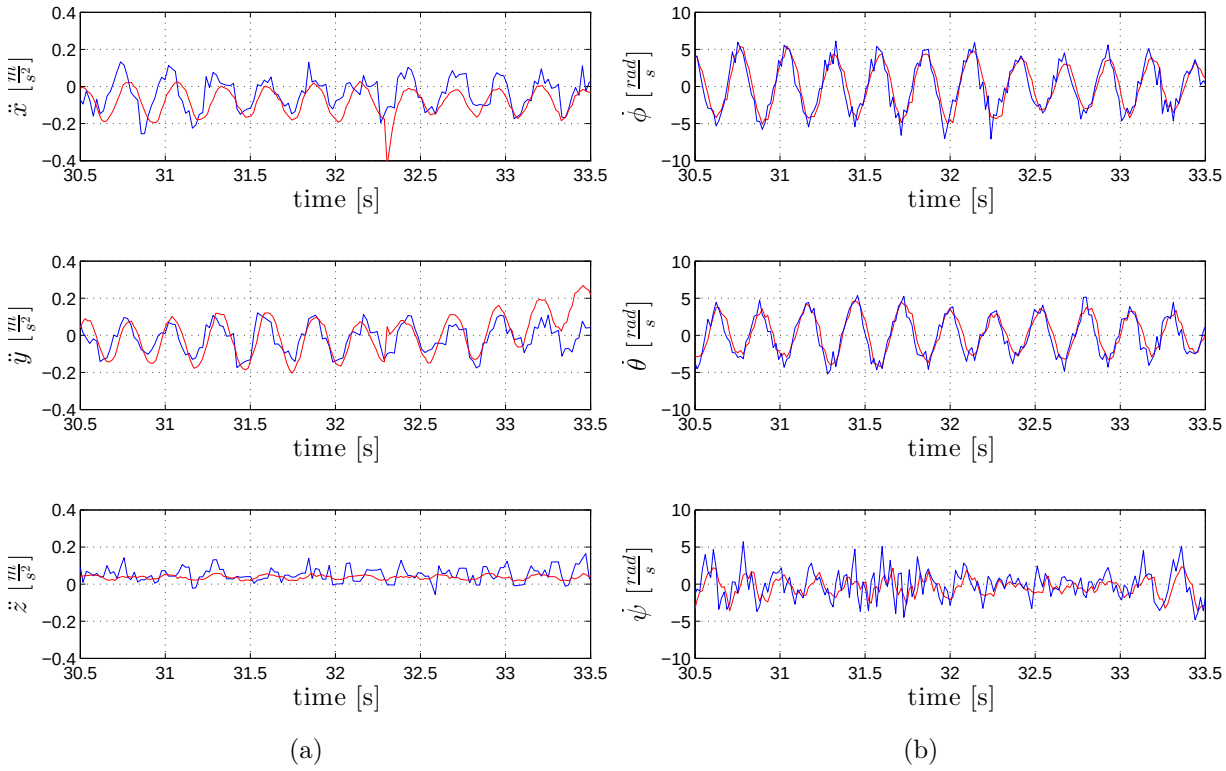

Figure 3.3: (a): Components of acceleration $\ddot{\boldsymbol{p}}$ in x, y and z. Blue line: obtained from onboard accelerometer; red line: acceleration estimates like in 3.16. (b): Components of angular acceleration $\dot{\boldsymbol{\omega}}_B$ in x, y and z. Blue line: numerical derivation of onboard gyroscope data; red line: Angular acceleration estimates like in 3.16

Chapter 4

Holocopter Prototype and System Architecture

Two prototypes have been designed, developed and built. The first prototype is designed as a limited first proof of concept prototype. While the second prototype is an advanced solution able to benefit from all advantages of an overactuated quadrotor. The second prototype is currently under final software development. Both prototypes will be discussed intensively in the following. If only the term holocopter is mention it always refers to the prototype of the current section.

4.1 Prototype I

This section has been mainly reproduced from an article published in ICRA 2013: Ryll et al. (2013)

As first prototype we opted for a very low cost solution with all parts available off-the-shelf. The overall cost including all mechanical and electrical parts and actuators is below 1000 €. The mechanical main frame of the holocopter is based on the MikroKopter[1] module, including the propeller (EPP1045 CF) and the brushless propeller motors (Roxxy 2827-35). At the end of every arm of the holocopter body, a rigidly connected axle allows rotation of the propeller groups containing the propeller motor and the servo motor for the tilting actuation (Robbe S3150 Digital), see Fig. 4.1. This has a maximum torque

[1] http://www.mikrokopter.de

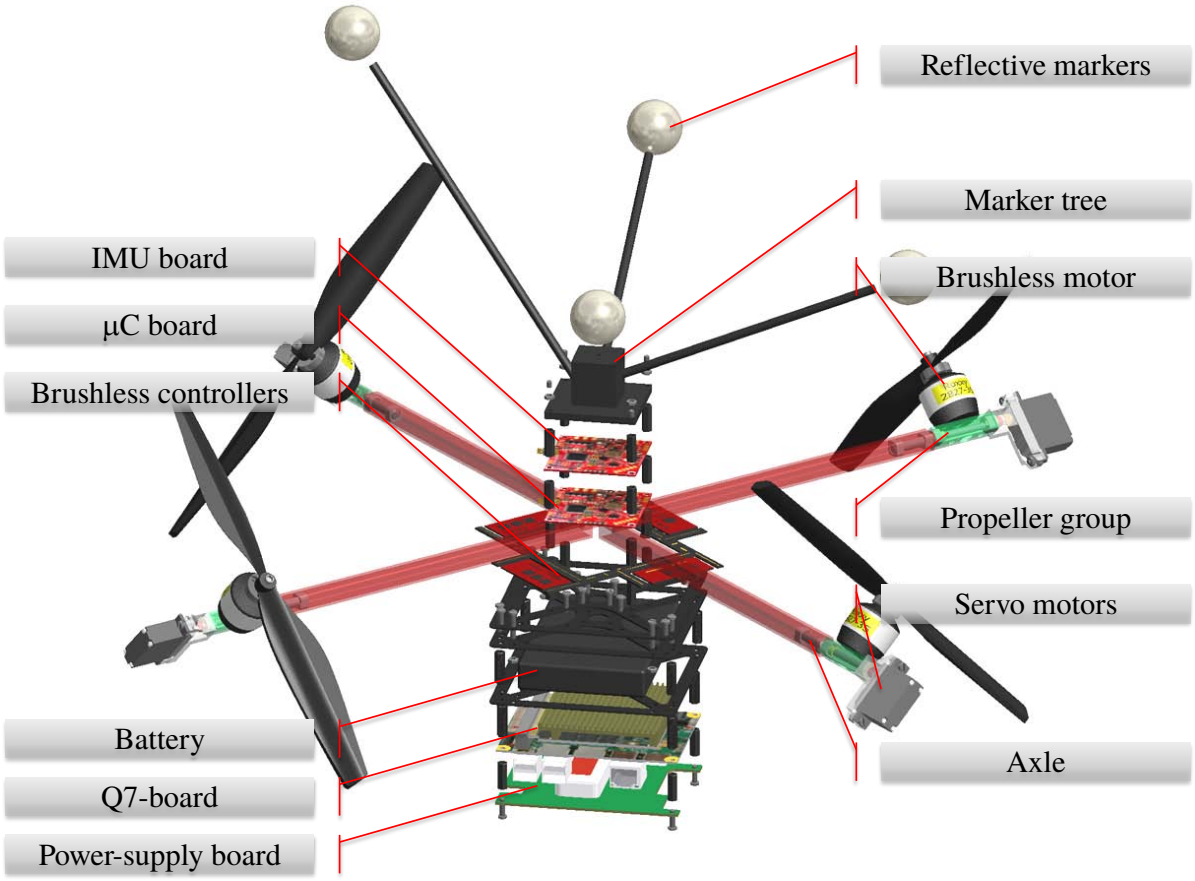

Figure 4.1: Exploded view of the various components of the holocopter. All the important parts are properly labeled

$\tau_{\alpha_{max}} = 0.37$ Nm and a maximum rotation speed $\dot{\alpha}_{max} = 4.1$ rad/s. The propeller group is designed in order to have its barycenter as close as possible to the axle, as assumed in the dynamical model developed in Sect. 2.

Furthermore, two microcontroller boards are mounted on top of the holocopter. The first contains the gyroscopes measuring $\boldsymbol{\omega}_B$, and is also in charge of reading the tilting angles α_i of the servo motors and the spinning velocities $\bar{w}_i$ of the propellers. The second microcontroller board sends the desired spinning velocities $\bar{w}_{Des_i}$ to the brushless controller and the desired angles α_{Desi} to the servo motors.

The trajectory tracking controller of Sect. 3 is implemented in Matlab/Simulink and, via the Real-Time Workshop toolbox, deployed and executed in real-time on an Intel Atom board (Quadmo747, from now on 'Q7-board') running the Linux Ubuntu10.10 real-time environment. The Q7-board is mounted below the battery and is equipped with a Wifi

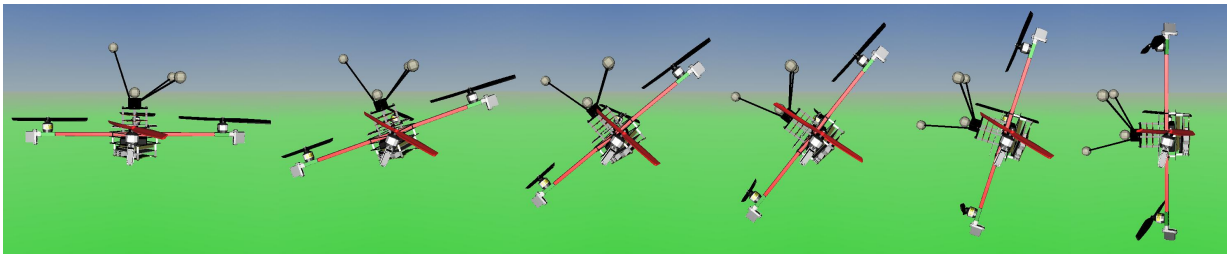

Figure 4.2: Illustrating snap shot series of the holocopter simulation. Holocopter performs a rotation of $\frac{\pi}{2}$ rad around x-axis. Please note the orientation of the propellers during the maneuver

USB-dongle for communication. As only one RS-232 port (TTL level) is available on the Q7-board, the second microcontroller board is connected via USB-port and an USBToSerial converter. The Q7-board is powered by a battery, with the necessary voltage conversion and stabilization performed by a power-supply board containing a 12V DC/DC power converter.

The nominal mass of the full holocopter is 1.32 kg. From a high detail CAD model of the body and propeller groups we also obtained the following inertia matrixes

$$\boldsymbol{I}_{P_i} = \begin{bmatrix} 8.450e^{-5} & 0 & 0 \\ 0 & 8.450e^{-5} & 0 \\ 0 & 0 & 4.580e^{-5} \end{bmatrix} \left[\mathrm{kg\,m^2}\right]$$

and

$$\boldsymbol{I}_{B} = \begin{bmatrix} 0.0154 & 0 & 0 \\ 0 & 0.0154 & 0 \\ 0 & 0 & 0.0263 \end{bmatrix} \left[\mathrm{kg\,m^2}\right].$$

In the current setup, the servo motors are limited in their rotation by mechanical end stops in the range of -90 deg $< \alpha_i <$ 90 deg. For our particular prototype, these limits translate into a maximum achievable rotation (in hover) of $\approx \pm 55$ deg around the roll or pitch axes for the body frame B (this value was experimentally determined) (Ryll et al. (2012)).

How the servo motor positions α_i are changing over a main body rotation maneuver can be seen in figure 4.2. The fourth holocopter from the left in the figure illustrates the maximum achievable rotation for the prototype and the servo motors with $-\alpha_1 = \alpha_3 \approx 90$ deg.

In order to obtain accurate values of k_f and k_m for the used motor-propeller combination, we made use of a testbed equipped with a 6-dof force/torque sensor (ATI Nano17-E, see

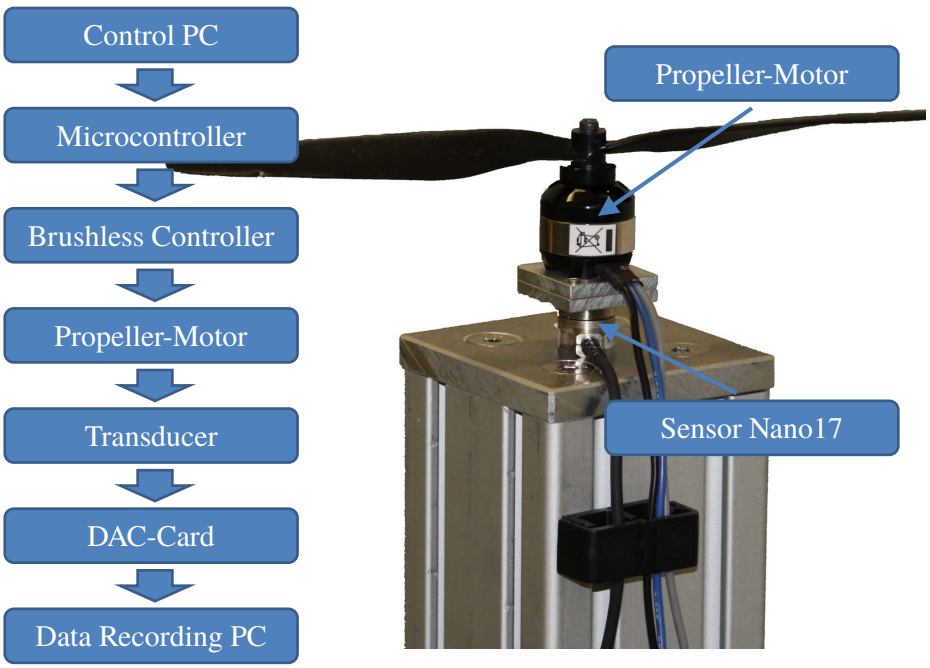

Figure 4.3: Left: Scheme of the measurement chain; Right: Motor testbed including Propeller motor combination and Nano17 sensor mounted at a height of 0.45 m

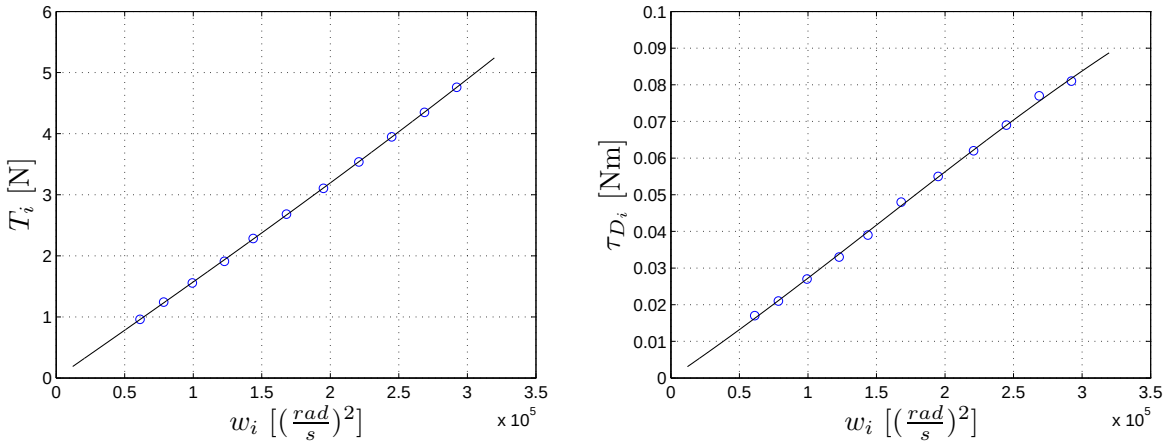

(a)

Figure 4.4: (a) and (b): Dots - measured values of the thrust T_i and torque τ_{D_i} vs. the signed squared spinning velocity w_i; Black lines - identified polynomial model (4.1) and (4.2)

Fig. 4.3) for identifying the mappings between the propeller spinning velocity and the generated thrust $\|\boldsymbol{T}_{P_i}\|$ and torque $\|\boldsymbol{\tau}_{ext_i}\|$, see (2.2–2.3). A linear model (k_f and k_m are constant) fits the measured thrust and torque for a maximum spinning velocity with a $\approx 5\%$ error. As this is considered as too imprecise the following polynomial models are used (shown in Fig. 4.4):

$$\|\boldsymbol{T}_{P_i}\| = 4.94e^{-18}|w_i|^3 + 9.62e^{-13}|w_i|^2 + 1.56e^{-5}|w_i| \tag{4.1}$$

and

$$\|\boldsymbol{\tau}_{ext_i}\| = -5.41e^{-19}|w_i|^3 + 2.50e^{-13}|w_i|^2 - 2.53e^{-7}|w_i| \tag{4.2}$$

where $w_i = \bar{w}_i|\bar{w}_i|$ is the signed square of the propeller spinning velocity as previously explained. The controller (3.7) was then implemented by directly exploiting the mappings (4.1–4.2) for obtaining ($\|\boldsymbol{T}_{P_i}\|$, $\|\boldsymbol{\tau}_{ext_i}\|$), and by replacing $k_f = \left.\frac{\partial\|\boldsymbol{T}_{P_i}\|}{\partial w_i}\right|_{w_i}$ and $k_m = \left.\frac{\partial\|\boldsymbol{\tau}_{ext_i}\|}{\partial w_i}\right|_{w_i}$, both evaluated upon the measured w_i.

4.1.1 Propeller motor brushless controller

The used brushless controller[2] drives the 3-phase brushless motor by a PWM signal. The board is equipped with an MEGA8-AI micro controller that controls the 3 power output stages (one for every stage). A single power output stage consists of an N-channel and a P-channel MOSFET. The resolution of the PWM is 8 bit (see GmbH HiSystems (2014)), e.g. up to 256 different speed values can be set. To check the control accuracy of the brushless controller with a dropping battery voltage we conducted an experiment with a constant desired spinning velocity w of a single propeller over a time of 16 minutes. The generated thrust F was measured over time. In figure 4.5 (a) it is clearly visible that the generated thrust is decreasing over time.

As a consequence an own control algorithm has been developed for the MEGA8-AI microcontroller on the brushless controller. Via a look-up table a PID controller was implemented that controls the spinning velocity w by measuring the time between the changes of two phases of the brushless motor. The result of a repeated experiment with the new controller is shown in figure 4.5 (b). It is clearly visible that the generated thrust

[2]BL-Ctrl V1.2 from mikrokopter

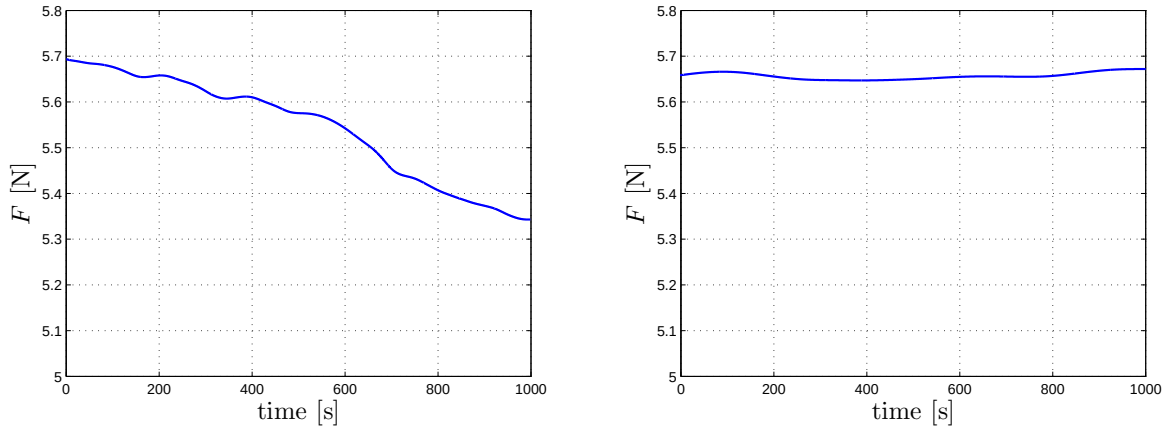

Figure 4.5: Generated thrust F of a single propeller over time. (a) - Original controller: With decreasing battery voltage the generated thrust F is decreasing as well. (a) - PID controller: The generated thrust F is not decreasing with a decreasing battery voltage

is not decreasing over time anymore.

4.1.2 OpenServo

The OpenServo project[3] is an open source community based project that intents to transforms standard analog RC servo motors into high quality digital servos with the option to either control position or the velocity of the servo motor. At the same time the current position, velocity, voltage and power can be read back. Any standard servo shall be transferable by changing the old internal controller by the OpenServo controller board. From the original servo motor the housing, bearings, motor and gearbox remain (see OpenServo.org (2014)). The new motor is then controlled via I^2C-Bus instead of a PWM signal. For the holocopter concept the OpenServo seemed to be beneficial for the following reasons:

- Control of either position α or velocity $\dot{\alpha}$
- Direct feedback of servo position α and velocity $\dot{\alpha}$
- Availability of the I^2C-Bus at the flight control

[3] http://openservo.com

- Shorter signal delay of I^2C-Bus compared with PWM
- Higher control frequency (standard servos /$approx$50 Hz)
- Very lightweight
- Directly available and cheap solution

For a first test an OpenServo v2-module has been used combined with a Robbe s3150 servo motor. The results were very disappointing. A stable or accurate control could not be achieved. Additionally in a final position the servo motor was still oscillating. Therefore it was decided to not use the OpenServo-modules any more but directly the original Robbe s3150 servo motors with a maximum torque of $\tau_{max} = 0.046Nm$ and a maximum velocity of $\dot{\alpha}_{max} \approx 4.133\frac{\text{rad}}{\text{s}}$ (see robbe Modellsport GmbH & Co. KG (2014)).

4.1.3 System architecture

The Q7-board runs a GNU-Linux Ubuntu 10.10 real time OS and executes the Matlab-generated code. The controller runs at 500 Hz and takes as inputs: (i) the desired trajectory ($\boldsymbol{p}_d(t)$, $\boldsymbol{R}_d(t)$) and needed derivatives ($\dot{\boldsymbol{p}}_d(t)$, $\ddot{\boldsymbol{p}}_d(t)$, $\dddot{\boldsymbol{p}}_d(t)$) and ($\boldsymbol{\omega}_d(t)$, $\dot{\boldsymbol{\omega}}_d(t)$, $\ddot{\boldsymbol{\omega}}_d(t)$), (ii) the current position/orientation of the holocopter ($\boldsymbol{p}$, ${}^W\boldsymbol{R}_B$) and its linear/angular velocity ($\dot{\boldsymbol{p}}$, $\boldsymbol{\omega}_B$), (iii) the spinning velocities of the propellers w_i, (iv) the tilting angles α_i.

The position $\boldsymbol{p}$ and orientation ${}^W\boldsymbol{R}_B$ of the holocopter are directly obtained from an external motion capture system[4] (MoCap) at 200 Hz. A marker tree consisting of five infra-red markers is mounted on top of the holocopter for this purpose. Knowing $\boldsymbol{p}$, the linear velocity $\dot{\boldsymbol{p}}$ is then obtained via numerical differentiation, while the angular velocity $\boldsymbol{\omega}_B$ is measured by the onboard IMU (3 ADXRS610 gyroscopes).

Due to performance reasons (bottleneck in serial communication), the sending of the desired motor speeds and tilting angles, and the reading of the IMU-data, of the actual spinning velocities, and of tilting angles is split among two communication channels and two microcontrollers (called, from now on, 'μC-Board' and 'IMU-Board'). The desired motor spinning velocities w_{Des_i} are sent from the Q7-board to the μC-Board via a serial connection at the frequency of 250 Hz and 8 bit resolution, and from the μC-Board to the

[4] http://www.vicon.com/products/bonita.html

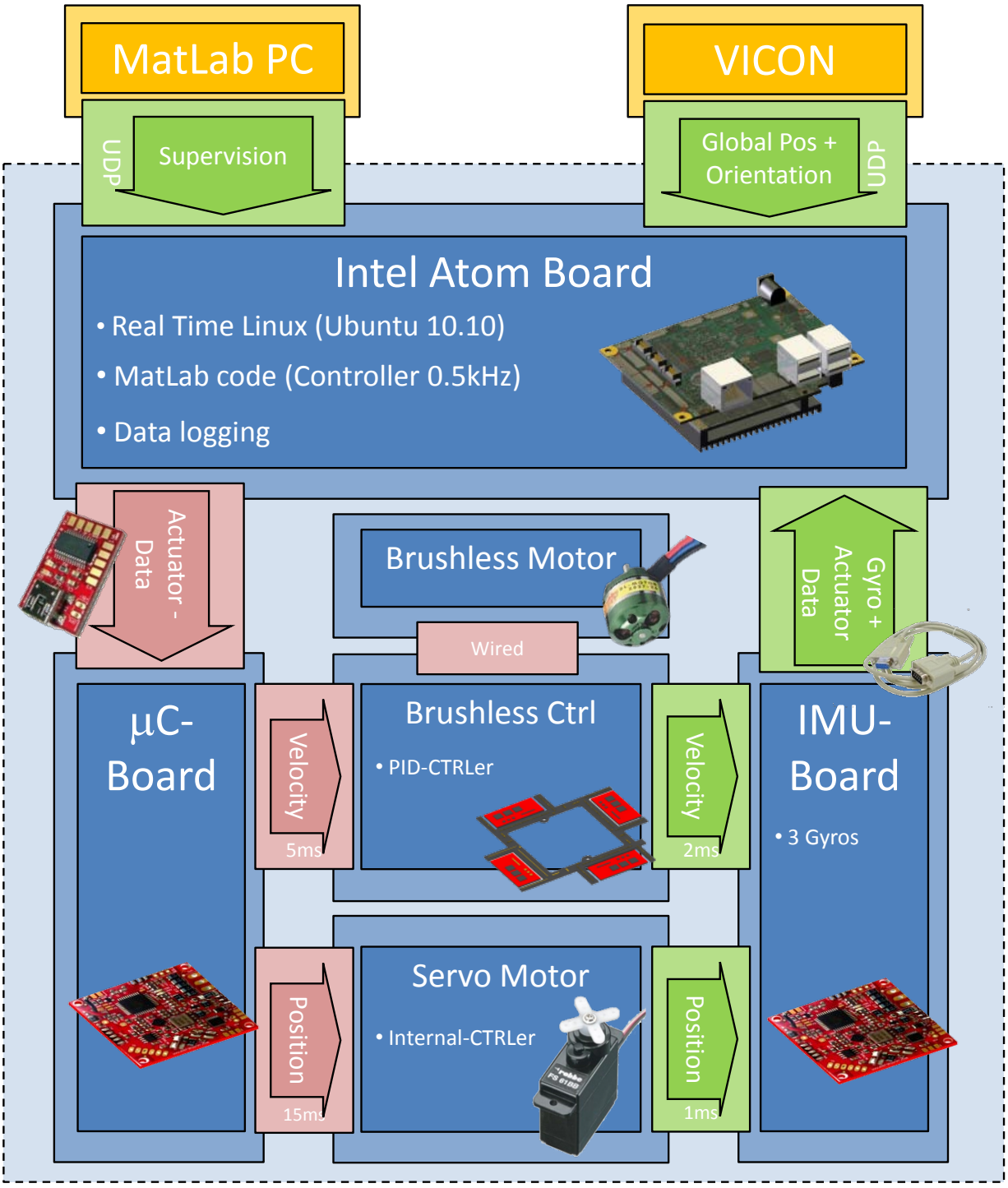

Figure 4.6: Overview of the holocopter architecture including update rates and delays

brushless controllers via I^{2}C-bus at again 250 Hz. In the same manner, the *actual* spinning velocities w_i of the 4 propellers can be read back at a frequency of 250 Hz and a resolution of 8 bit. As a matter of fact the I^{2}C-bus protocol allows only communication started by the master. That means receiving the w_i increases the load on the bus a lot. Therefore not the measured w_i is used in 3.16 but the integrated output w_i from 3.8. The brushless controllers implement a PID-controller for regulating the spinning velocity. The desired tilting angles α_{Des_i} are sent from the Q7-board to the μC-Board via the same serial connection at a frequency of 55 Hz and 10 bit resolution, and from the μC-Board to the servo motors via PWM (signal length 15 ms). We note that the trajectory tracking controller described in Sect. 3 assumes availability of the *tilting velocities* w_{α_i} as inputs, see (3.7), while the current architecture only allows for sending desired angles commands $\alpha_{Des_i}(t)$. This is addressed by numerically integrating over time the controller commands w_{α_i}, that is, by implementing

$$\alpha_{Des_i}(t) = \int_{t_0}^{t} w_{\alpha_i}(\tau)\mathrm{d}\tau + \alpha_i(t_0), \tag{4.3}$$

where $\alpha_i(t_0)$ represents the i-th *measured* tilting angle at the beginning of motion[5].

The IMU-Board reads the current angles α_i of the propeller groups P_i by a direct connection between the servo motor potentiometer and the A/D-converter of the microcontroller (10 bit resolution at 250 Hz). It also retrieves the current spinning velocities $\bar{w}_i$ of the propellers via the I^{2}C-Bus (8 bit resolution and 250 Hz). The gyroscope data are read at 250 Hz and converted with 10 bit resolution. Finally, the values of α_i, $\bar{w}_i$ and of the gyroscope data are transmitted from the IMU-Board to the Q7-board via the RS232-port at 250 Hz. All values of the controller can be monitored on a remote Windows PC which mirrors the running controller in real time using the matlab/simulink "external mode". This simplifies the development as most of the gains and settings can be changed online during flight tests.

The communication architecture for the tilting angles α_{Des_i} (in particular, the PWM modulation) unfortunately introduces a non-negligible roundtrip delay of about 18 ms form sent commands to read values. We experimentally found this delay to significantly degrade the closed-loop performance of the controller, and therefore propose in the next Sect. 4.1.4 a simple prediction scheme for mitigating its adverse effects.

[5]We note that, in order to avoid possible numerical drifts, one could also exploit the measured $\alpha_i(t)$ for resetting (4.3) when needed.

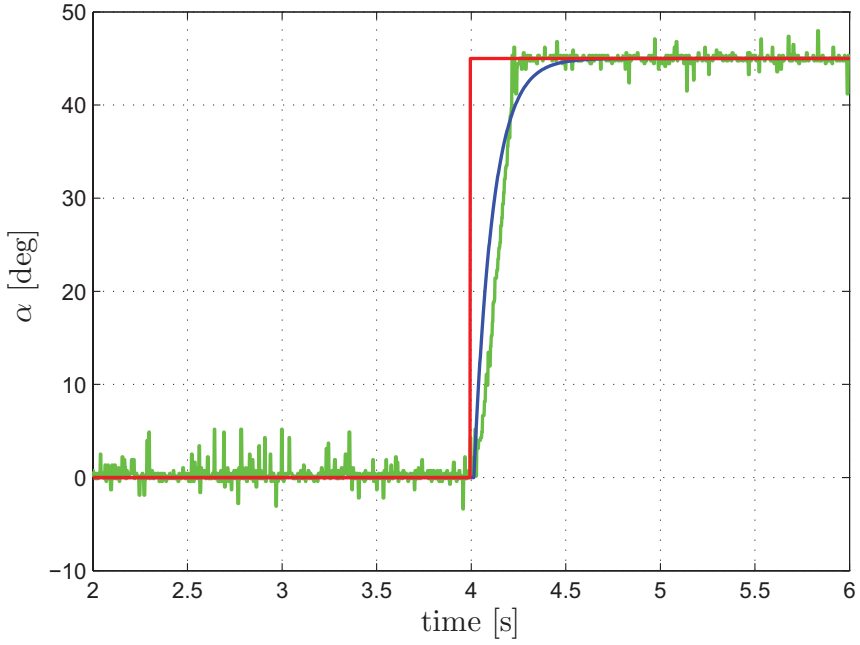

Figure 4.7: Modeling of the servo motor. Behavior of the real servo motor (green) and the model (blue) following a step input (red) of 45 deg after compensating for the (known) transport delay $T = 18$ ms

4.1.4 Coping with the non-idealities of the servo motors

The i-th servo motor for the tilting angles can be approximately modeled as a linear transfer function $G(s)$ with, in series, a transport delay of $T = 18$ ms, that is, as the delayed linear system $\alpha_i(s) = G(s)e^{-Ts}\alpha_{Des_i}(s)$. A model of the undelayed $G(s)$ was experimentally obtained by measuring the step response of the servo motors while having the propellers spinning at $\bar{w}_i = 450$ rad/s (the velocity corresponding to hovering), and by compensating offline for the known delay T, see Fig. 4.7. This resulted into the estimated transfer function

$$G_{est}(s) = \frac{0.4s + 6}{0.06s^2 + s + 6}. \tag{4.4}$$

The performance degradation of the cartesian trajectory controller (3.7)–(3.14) can then be ascribed to two main effects, namely presence of the transport delay T and slow dynamic response of $G_{est}(s)$ to fast changing inputs. In order to mitigate these shortcomings, we resorted to the following simple strategy (see Fig. 4.8): instead of feeding back the measured (i.e., delayed) angles α_i to the cartesian controller (3.7)–(3.14), we replaced them with

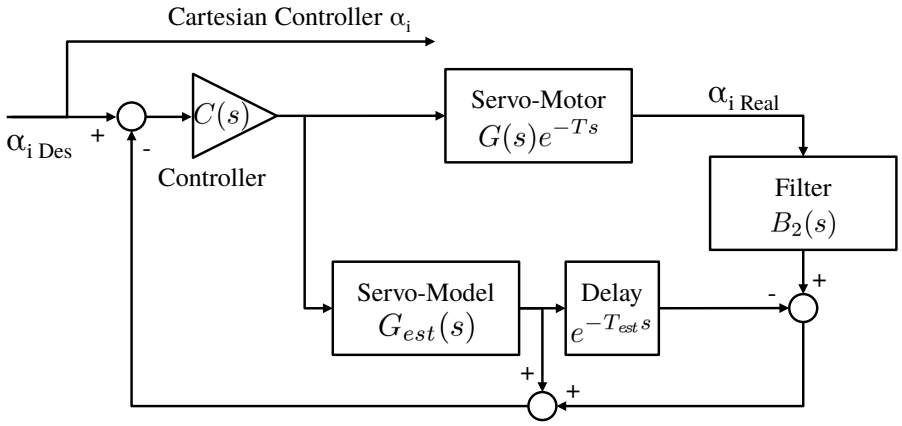

Figure 4.8: Scheme of the Smith predictor for α_i including the controller $C(s)$, the servo motor $G(s)e^{-Ts}$, the model of the servo motor $G_{est}(s)e^{-Ts}$, and the Butterworth filter $B_2(s)$

the (undelayed) desired angles α_{Des_i} from (4.3). In parallel, we aimed at improving the servo motor performance (i.e., making $G_{est}(s)$ more responsive) by resorting to a Smith predictor scheme Wolovich (1994). In fact, as well-known from classical control theory, the Smith predictor is an effective tool for coping with *known* delays affecting *known* stable linear systems. In our case, an additional outer PID controller $C(s)$ plugged into the Smith predictor loop, as shown in Fig. 4.8, allowed to improve the rising time of the servo controller. Finally, since we found the measured angles α_i to be affected by significant noise, we filtered their readings with a 2nd order Butterworth filter with a cutoff frequency of 20 Hz. The location of this cutoff frequency was experimentally determined by analyzing offline the power spectrum of the angles α_i recorded during a hovering flight of 40 s.

As experimental proof of the effectiveness of the above strategy in coping with the non-idealities of the holocopter actuation system, we ran the following two illustrative experiments involving a simple hovering on the spot task. In both experiments, the scheme of Fig. 4.8 was activated for an initial period $0 \leq t \leq t_{\text{off}}$ after which the scheme was instead 'switched off': for $t \geq t_{\text{off}}$ the trajectory controller was then fed back with the measured (and thus delayed) angles $\alpha_i(t)$ (case I), and with the desired angles $\alpha_{Des_i}(t)$ (case II).

The results are reported in Figs. 4.9(a–d). We first note how, in both cases, the hovering task is correctly realized during $0 \leq t \leq t_{\text{off}}$, i.e., when employing the scheme of Fig. 4.8. Then, in case I the holocopter becomes unstable almost instantaneously for $t > t_{\text{off}}$, while

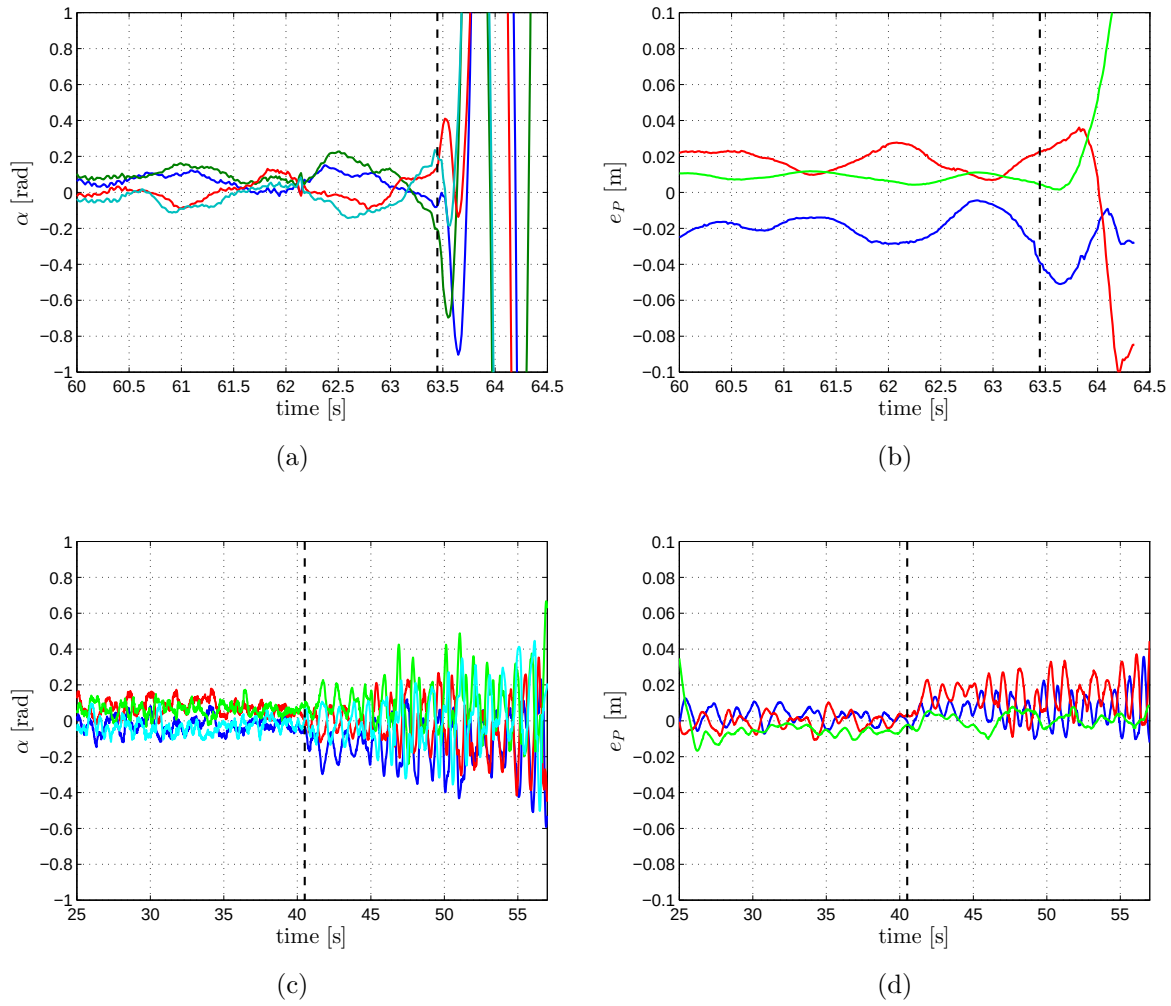

Figure 4.9: Results of the experiments assessing the effectiveness of the scheme in Fig. 4.8. In all the plots the vertical dashed black line indicates the time t_{off} after which the scheme is 'switched off'. (a) behavior of the tilting angles $\boldsymbol{\alpha}(t)$ during case I; (b) Position tracking error $\boldsymbol{e}_P(t)$ during case I; (c) behavior of tilting angles $\boldsymbol{\alpha}(t)$ during case II; (d) Position tracking error $\boldsymbol{e}_P(t)$ during case II. Note how in both cases the holocopter becomes unstable for $t \geq t_{\text{off}}$, thus confirming the validity of the scheme in Fig. 4.8 in coping with the non-idealities of the employed servo motors

in case II the servo motors start to slowly oscillate to then reach practical instability at about $t > t_{\text{off}} + 15$ s. These results allow us to then conclude the ability of the proposed strategy to cope with the shortcomings of the holocopter actuation system.

4.2 Prototype II

4.2.1 Mechanical design

After very promising experiments (see section 6) with the first prototype it has been decided to design and build a second prototype based on the experiences of the first holocopter. Based on simulations the low control rate and especially the communication delay of the servo motor have been identified as the bottleneck of precise position and orientation tracking of the first prototype (see section 5.2.3). Furthermore, a list of requirements has been defined to additionally improve the holocopter:

- Revision of the servo motors
  - Control frequency ≥ 200 Hz
  - Communication send delay ≤ 5 ms
  - Continuous rotation of the servo arm
- Reduction of weight by ≥ 20 %
- Reduction of inertia by ≥ 20 %
- Increase of computational power
- Center of gravity coincides with center of arm rotation
- Center of arm rotation in alignment with center of thrust and drag

To fulfill these requirements a complete redesign was necessary (see figure 4.10). To achieve an alignment between the arm rotation and the center of generated thrust as well as the center of gravity of the main body, it was mandatory to not let the propeller motors directly rotate around their arms. Therefore the servo motors of the second prototype are

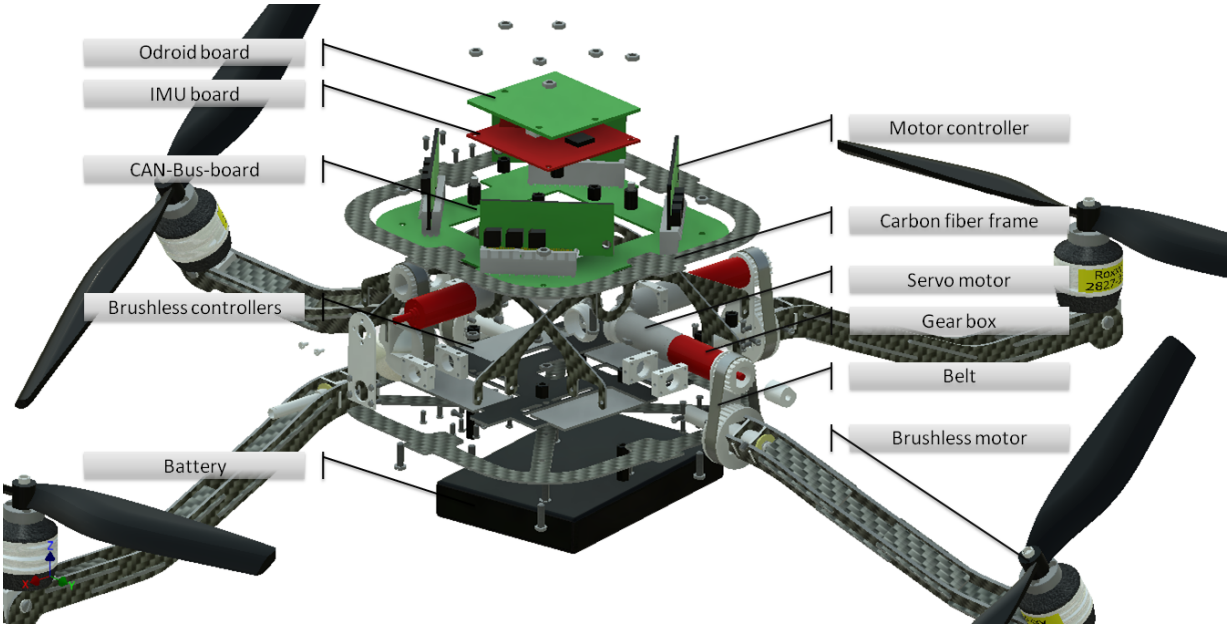

Figure 4.10: Exploded view of the various components of the holocopter version 2. All the important parts are properly labeled

not located at the end of every arm anymore but have been moved closer to the center of the main body which as well reduces the inertia of the whole system.

To allow an infinite rotation of the arms, the servo motors could not directly actuate the arms as the cables of the propeller motors have to be hosted in the hollow axles (see figure 4.11). Therefore the arms are actuated via two pulleys with a timing belt in between and a gear reduction of 1.6. To reduce the mass of the pulleys and to reduce the developing time of the second prototype, the pulleys are manufactured via rapid prototyping on an Objet Eden260 3d printer. Following the rapid prototype approach, several parts have been manufactured on the 3d printer. For more detailed information see appendix B.1. Slip rings inside the arms of the holocopter offer endless rotation of the arms without twisting the cables for the propeller motors. To reduce the mass and inertia of the holocopter, the frame is made of carbon-fiber-reinforced polymer. To increase the stiffness of the arms they consist of an agglutinated plug-in system.

To improve the actuation of the arms RC servo motors are not used anymore but high quality motor gear box systems from Maxon. The motors are equipped with encoders with a resolution of 256 counts per turn. The gearbox reduces the transmission by $67:1$. This allows a theoretical resolution of the arm angle of $4367.7\frac{1}{\text{rad}}$. The maximum torque of the

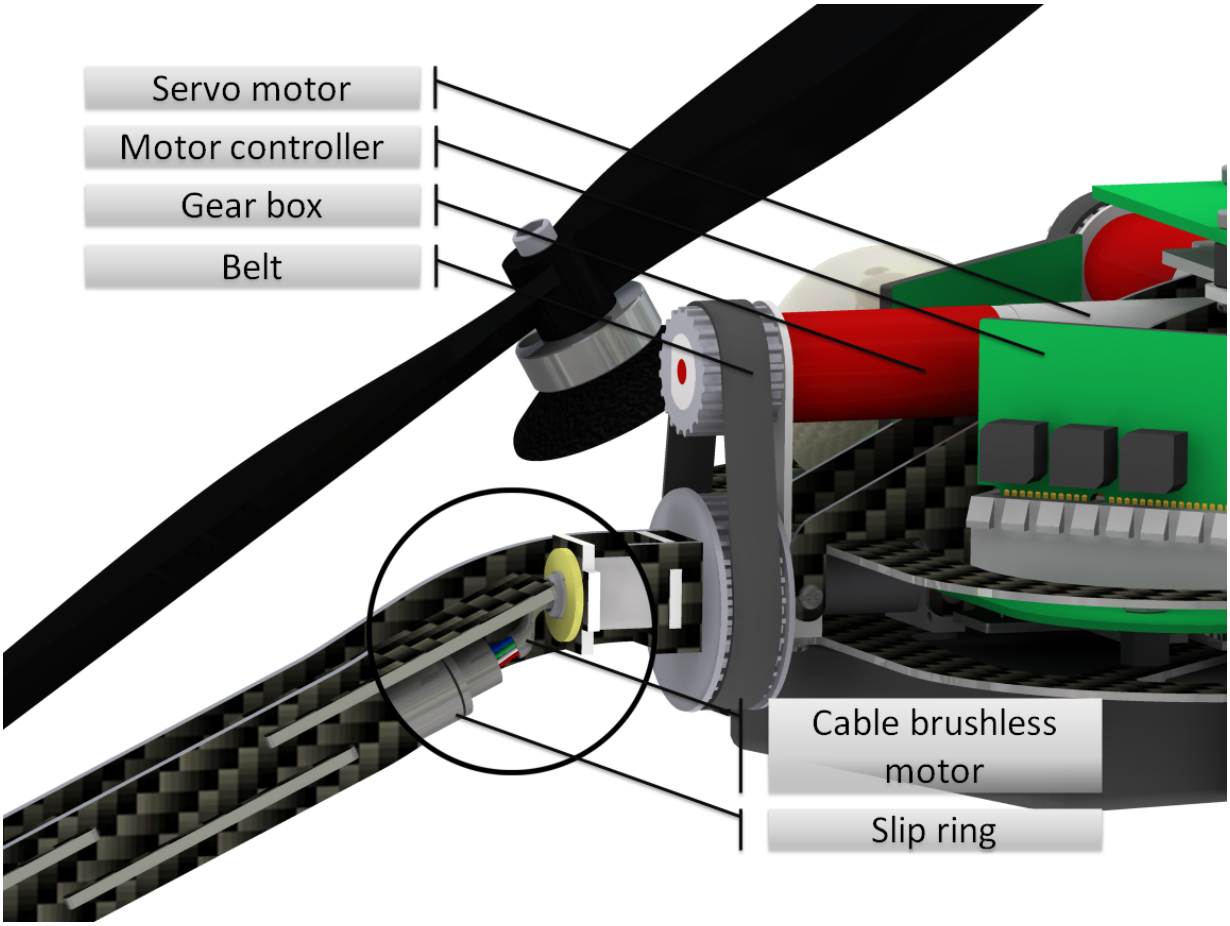

Figure 4.11: Close view of the actuation system of a holocopter arm. The arm has been made party transparent to see the slip ring and the cable route

whole actuation system including the transmission is $\tau_{max} = 0.497$ Nm and the maximum velocity is $\dot{\alpha} = 7.543\frac{\text{rad}}{\text{s}}$. The servo motors are driven by Maxon EPOS2 controllers.

The overall mass of the holocopter is $m = 1.03$ kg and from a high detail CAD model of the body and propeller groups we also obtained the following inertia matrices

$$\boldsymbol{I}_{P_i} = \begin{bmatrix} 7.15e^{-5} & 0 & 0 \\ 0 & 44.0e^{-5} & 0 \\ 0 & 0 & 41.3e^{-5} \end{bmatrix} \left[\text{kg m}^2\right]$$

and

$$\boldsymbol{I}_B = \begin{bmatrix} 7.92e^{-4} & 0 & 0 \\ 0 & 9.99e^{-4} & 0 \\ 0 & 0 & 12.38e^{-4} \end{bmatrix} \left[\text{kg m}^2\right].$$

The defined requirement for a reduction of the mass could be achieved with a nominal reduction of 22%. If the inertia of the whole holocopter prototypes is compared (main body including arms with $\alpha = 0$ for all arms referred as I_{HC}) a reduction of 20% has been achieved for $I_{HC_{11}}$ and $I_{HC_{22}}$ while for $I_{HC_{33}}$ only a negligible reduction of 1% has been achieved. This is due to a larger diameter of 52.5 mm of the second prototype and the fact that an essential part of the mass is concentrated in the propeller motors that are on the outer most of the diameter.

4.2.2 System architecture

The system architecture is similar to the first prototype but all parts have been updated to later products. On board of the holocopter is a pico ATX format computer board equipped with an Intel Atom D525, 1.83 GHz microprocessor and 4 GB DDR2 RAM. The OS running on board is Ubuntu 12.04 LTS on a compact flash card.

EPOS2 controllers are high quality miniaturized position or velocity controllers for a variety of motor types (e.g. brushed DC motors, brushless EC motors). They can either be interfaced via CANopen or RS232. A single controller can be used as a gateway to other EPOS controllers. As the computer module of the holocopter is not equipped with a CAN-bus port the latter option has been implemented. A carrier board that has been designed to host the 4 EPOS2 controllers is as well equipped with an USB to serial converter (see appendix B.2). Following, the Intel Atom board is connected to the carrier board via

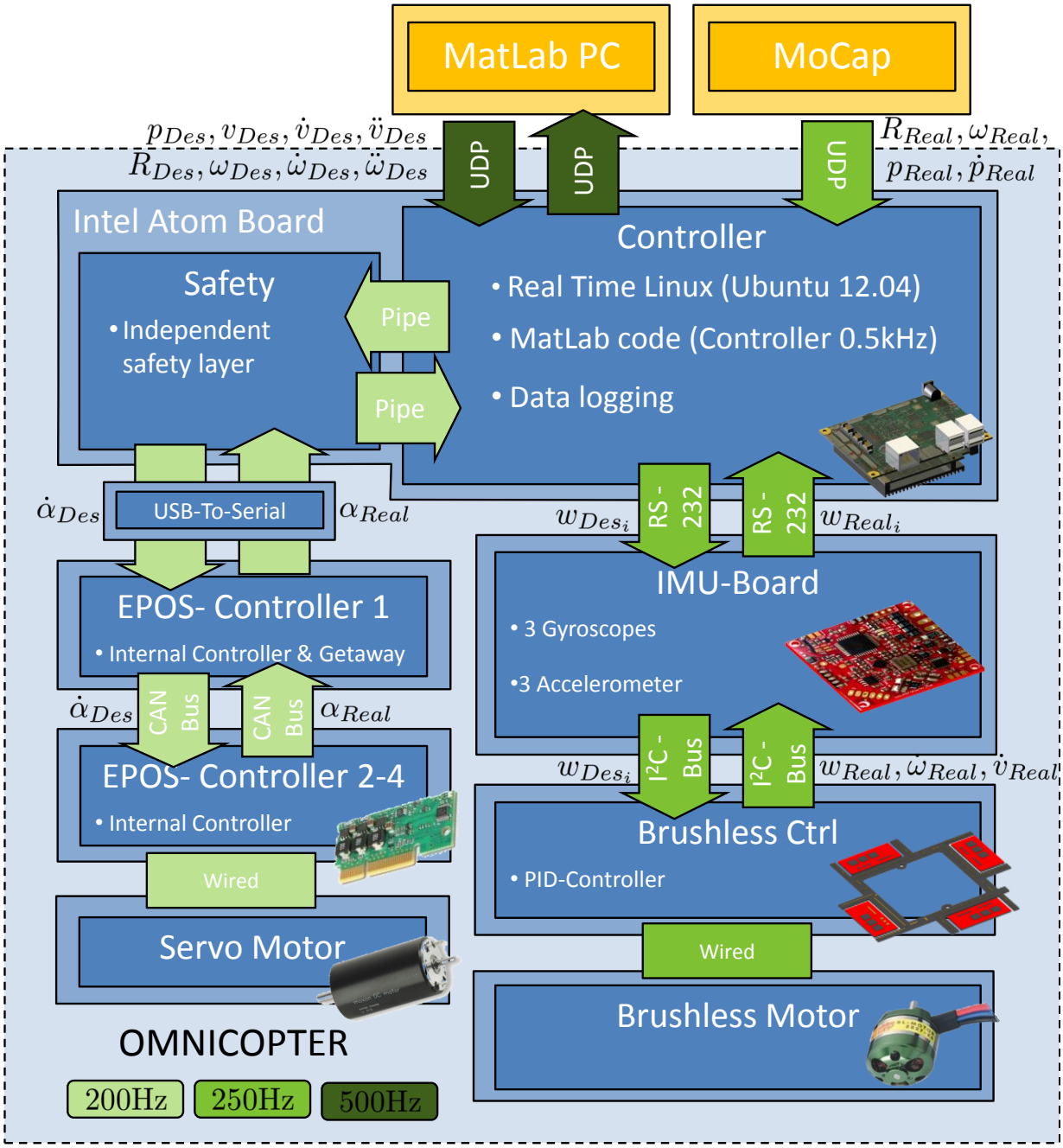

Figure 4.12: Overview of the holocopter architecture including update rates and delays

USB. Here the bus data are converted to RS232-bus and send to the first EPOS controller. The first EPOS controller is used as a gateway and connected to the three other EPOS controllers via CAN-Bus (see figure 4.12).

The IMU-board and the brushless controllers are purchased from mikrokopter. Compared to the first holocopter, IMU-board V2.1 (before V2.0) and brushless controller V2.0 (before V1.2) are used now. The new brushless controllers allow for a higher thrust and a more precise value resolution of the desired thrust of 11 bit (before 8 bit resolution). In the new control scheme the desired servo arm position α_{D_i} and the current position α_i is not transmitted via the IMU board anymore therefore the overall traffic on the serial bus is reduced. This allows for a general increase of the communication frequency of the desired motor speed w_i and the sensor reading frequency of the gyroscopes and accelerometers (increased to 250 Hz).

The new holocopter is currently under final software development. Therefore all reported flight experiments are performed with the first holocopter.

4.3 Energetic efficiency of the holocopter in hovering

As final consideration, we briefly discuss the energetic efficiency of the holocopter in a hovering condition. Indeed, we note that the holocopter energetic efficiency for arbitrary hovering orientations can be less than in the (standard) horizontal case ($\phi = 0,\ \theta = 0$), and also despite the optimization action (3.14). This is due to the adopted mechanical design which allows each propeller to 'only' rotate about one tilting angle (angles α_i): therefore, there will exist hovering orientations at which the thrust vectors $\boldsymbol{T}_{P_i}$ cannot be aligned against gravity, with thus some of the thrust lost in internal forces. This reduced efficiency cannot be completely avoided with the adopted design, but only partially mitigated via optimization actions such as (3.14). In this sense, the following Table 4.1 gives an illustration of the energetic efficiency of our prototype (in terms of the mean spinning velocity of the four propellers) obtained at several hovering conditions (including the horizontal one).

Pose	Mean spinning velocity $Avg(\bar{\boldsymbol{w}})$
$\theta = 0\ rad, \phi = 0\ rad, \psi = 0\ rad$	450 $\frac{rad}{s}$
$\theta = \frac{\pi}{4}\ rad, \phi = 0\ rad, \psi = 0\ rad$	504 $\frac{rad}{s}$
$\theta = \frac{\pi}{2}\ rad, \phi = 0\ rad, \psi = 0\ rad$	465 $\frac{rad}{s}$
$\theta = \frac{\pi}{2}\ rad, \phi = 0\ rad, \psi = \frac{\pi}{4}\ rad$	530 $\frac{rad}{s}$

Table 4.1: Mean spinning velocity $\bar{\boldsymbol{w}}$ of the four propellers for different hovering orientations

Chapter 5

Simulation Results

This chapter has been mainly reproduced from an article published in IEEE Transactions on Control Systems Technology: Ryll et al. (to be published 2014)

We now report simulation results aimed at validating the proposed control design. We first consider in Sect. 5.1 an 'ideal' case in which controller (3.7) is tested on the *complete* holocopter dynamical model of Sect. 2, that is, by including all the inertial and gyroscopic effects neglected at the control design stage. These results are meant to illustrate the flying performance of the holocopter in *ideal* conditions, that is, when not taking into account all the limitations and non-idealities affecting the real prototype as in Sect. 4.1.3.

Subsequently, we present in Sect. 5.2 an additional set of 'realistic' simulations that explicitly include the prototype main non-idealities (data exchange rates, control frequencies, and actuation delays). In these simulations the controller (3.7) is also complemented with the prediction scheme of Sect. 4.1.4 so as to replicate, as much as possible, the control architecture of the real prototype. The results are intended to show the robustness of the adopted control approach as the holocopter is still able to execute complex trajectories although with a poorer flight performance compared to the 'ideal' case (as expected). Furthermore, a comparison between both cases clearly shows the margin left for improving the actuation system of our prototype in its second generation (see Sect. 8).

5.1 Ideal Simulations

The aim of the following simulations is twofold: on one side, we want to highlight the tracking capabilities of the proposed controller and the beneficial action of the null-space term (19) in avoiding singularities for the decoupling matrix $\boldsymbol{A}(\boldsymbol{\alpha}, \boldsymbol{\omega})$. On the other side, we also want to show the robustness of the controller against all the inertial/gyroscopic effects neglected at the control design stage but included in the quadrotor dynamic model (2.1)–(2.4)–(2.5).

5.1.1 Rotation on spot

In this first simulation, we tested a simple trajectory involving a rotation of π rad on the spot along the $\boldsymbol{Y}_B$ axis[1]. The initial conditions were set to $\boldsymbol{p}(t_0) = \boldsymbol{0}$, $\dot{\boldsymbol{p}}(t_0) = \boldsymbol{0}$, $\boldsymbol{R}(t_0) = \mathbf{I}_3$, $\boldsymbol{\omega}_B(t_0) = \boldsymbol{0}$, $\boldsymbol{\alpha}(t_0) = \boldsymbol{0}$, $\dot{\boldsymbol{\alpha}}(t_0) = \boldsymbol{0}$, and $\boldsymbol{w}(t_0) = w_{rest}$. The desired trajectory was chosen as $\boldsymbol{p}_d(t) \equiv 0$ and $\boldsymbol{R}_d(t) = \boldsymbol{R}_X(\phi(t))$ with $\phi(t)$ following a smooth profile with maximum velocity $\dot{\phi}_{max} = 0.49$ rad/s and maximum acceleration $\ddot{\phi}_{max} = 0.16$ rad/s^2. The trajectory was executed twice by (i) including and (ii) not including the null-space term $\boldsymbol{z}$ (3.14) into (3.7) ($k_H = 1$ or $k_H = 0$). The gains in (3.9)–(3.11) were set to $\boldsymbol{K}_{p_1} = 28.5\mathbf{I}_3$, $\boldsymbol{K}_{p_2} = 271\mathbf{I}_3$, $\boldsymbol{K}_{p_3} = 857\mathbf{I}_3$ and $\boldsymbol{K}_{\omega_1} = 45\,\mathbf{I}_3$, $\boldsymbol{K}_{\omega_2} = 675\,\mathbf{I}_3$, and $\boldsymbol{K}_{\omega_3} = 3375\mathbf{I}_3$.

Figures 5.2(a–f) show the results of the simulation in these two cases. In particular, Fig. 5.2(a) shows the superimposition of $H(\boldsymbol{w})$ when including $\boldsymbol{z}$ (red dashed line, case (i)) and not including $\boldsymbol{z}$ (blue solid line, case (ii)). It is clear that, in the first case, $H(\boldsymbol{w})$ attains a lower value over time thanks to the optimization action in (3.14). As a consequence, this results in a lower value for $\|\boldsymbol{w}\|$ over time as depicted in Fig. 5.2(b) (same color pattern), showing that the given task (rotation on the spot) can be realized in a more 'energy-efficient' way when properly shaping the cost function $H(\boldsymbol{w})$. Note that, as a byproduct, the better performance of case (i) comes at the expense of a more complex reorientation of the propeller groups during the motion. This is shown in Figs. 5.2(c–d) which report the behavior of the 4 tilt angles α_i in cases (i) (left) and (ii) (right): compared to Fig. 5.2(d), note the rotation of two propellers starting from $t \approx 25.8$ $[s]$ in Fig. 5.2(c).

[1] This upside-down flip motion would be clearly unfeasible for a *standard* quadrotor. This trajectory is a continuation of the illustrated trajectory in figure 4.2 where the first half rotation is shown. It is (unfortunately) also unfeasible for the current experimental prototype because of the mechanical end stops in the propeller tilting actuation, see Sect. 4.1.

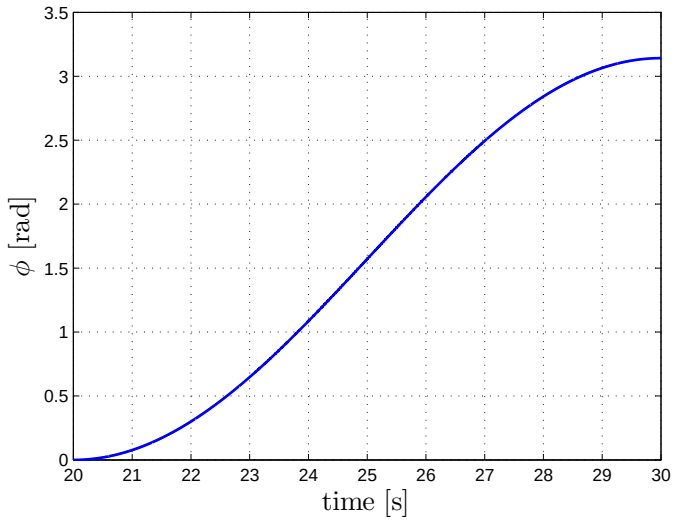

Figure 5.1: Profile of $\phi(t)$ for the first ideal simulation

Finally, Figs. 5.2(e–f) show, for case (i) only, the position tracking error $\boldsymbol{e}_P(t) = \boldsymbol{p}_d(t) - \boldsymbol{p}(t)$ and orientation tracking error $\boldsymbol{e}_R(t)$ as defined in (3.10). Despite the fast reorientation of two propellers highlighted in Fig. 5.2(c), the tracking errors stay small (note the scales) and eventually converge to zero as the desired trajectory comes to a full stop. Also, as one would expect, the largest peaks for the errors $\boldsymbol{e}_P(t)$ and $\boldsymbol{e}_R(t)$ occur at about $t \approx 25.8$ $[s]$, i.e., during the fast reorientation of the two propellers because of the internal gyroscopic effects treated as *external disturbances* by the controller.

These results then provide a first confirmation of the validity of our assumptions in Sect. 3, that is, robustness of the controller w.r.t. the gyroscopic/inertial effect due to the internal relative motion of the different bodies composing the quadrotor. For the reader's convenience, we also report in Figs. 5.3(a–b) a series of snapshots illustrating the quadrotor motion in these two cases (note the very different final configuration of the propeller group in cases (i) and (ii)).

5.1.2 Eight-shape trajectory

In this second simulation, the holocopter task is to track a planar 'eight-shape' trajectory $\boldsymbol{p}_d(t)$ while, at the same time, performing a sinusoidal rotation around the $\boldsymbol{Y}_B$ axis. The chosen desired trajectory $\boldsymbol{p}_d(t)$ is a horizontal eight-shape with size of 1.0 m by 1.4 m and

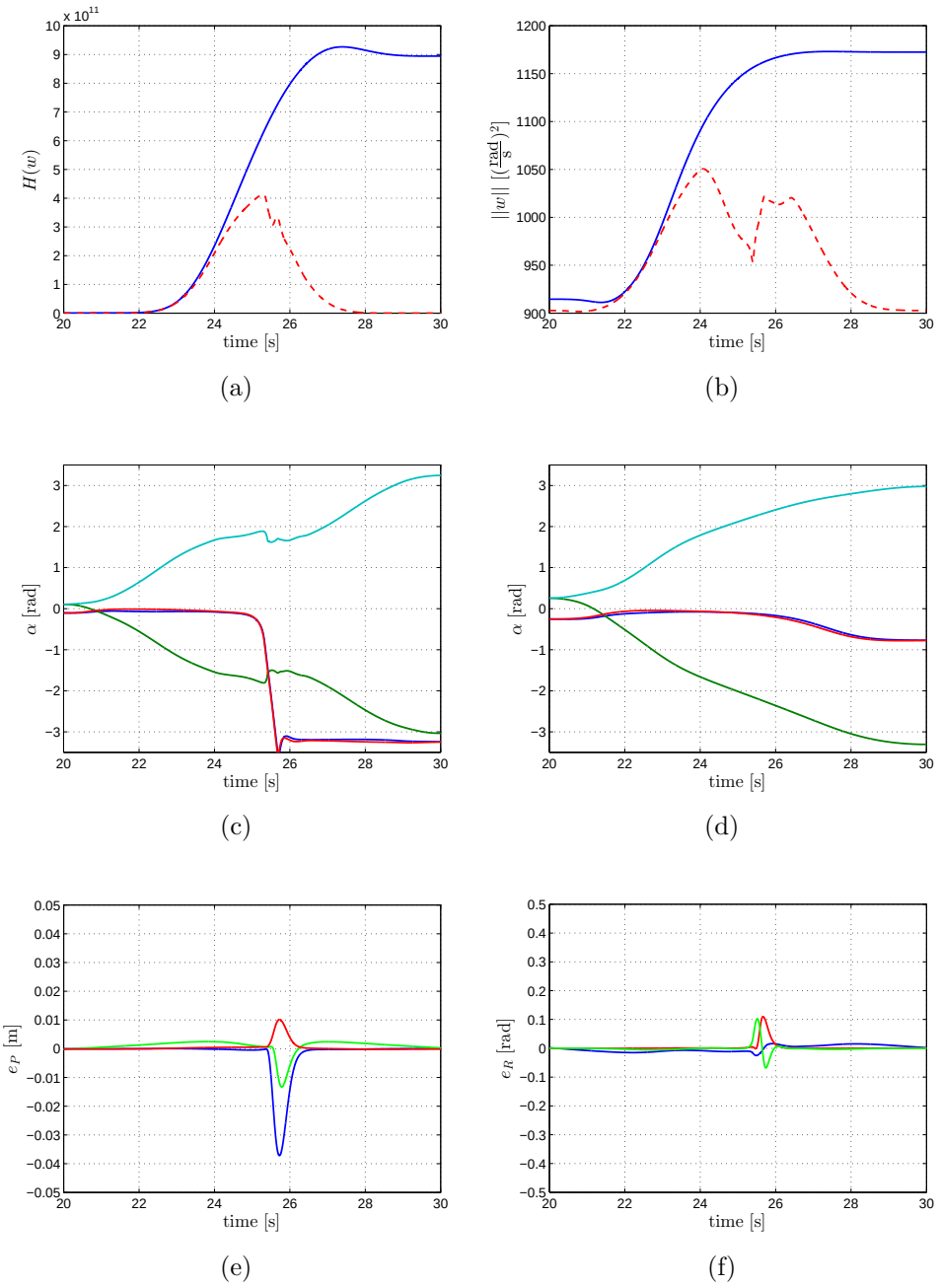

Figure 5.2: Results of the first ideal simulation with (*i*) and without (*ii*) exploiting the null-space term (3.14). 5.2(a): behavior of $H(\boldsymbol{w})$ for cases (*i*) (red dashed line) and (*ii*) (blue solid line). 5.2(b): behavior of $\|\boldsymbol{w}\|$ for cases (*i*) (red dashed line) and (*ii*) (blue solid line). 5.2(c–d): behavior of the tilt angles $\boldsymbol{\alpha}$ for cases (*i*) (left) and (*ii*) (right). 5.2(e–f): behavior of the position/orientation tracking errors ($\boldsymbol{e}_P$, $\boldsymbol{e}_R$) for case (*ii*).

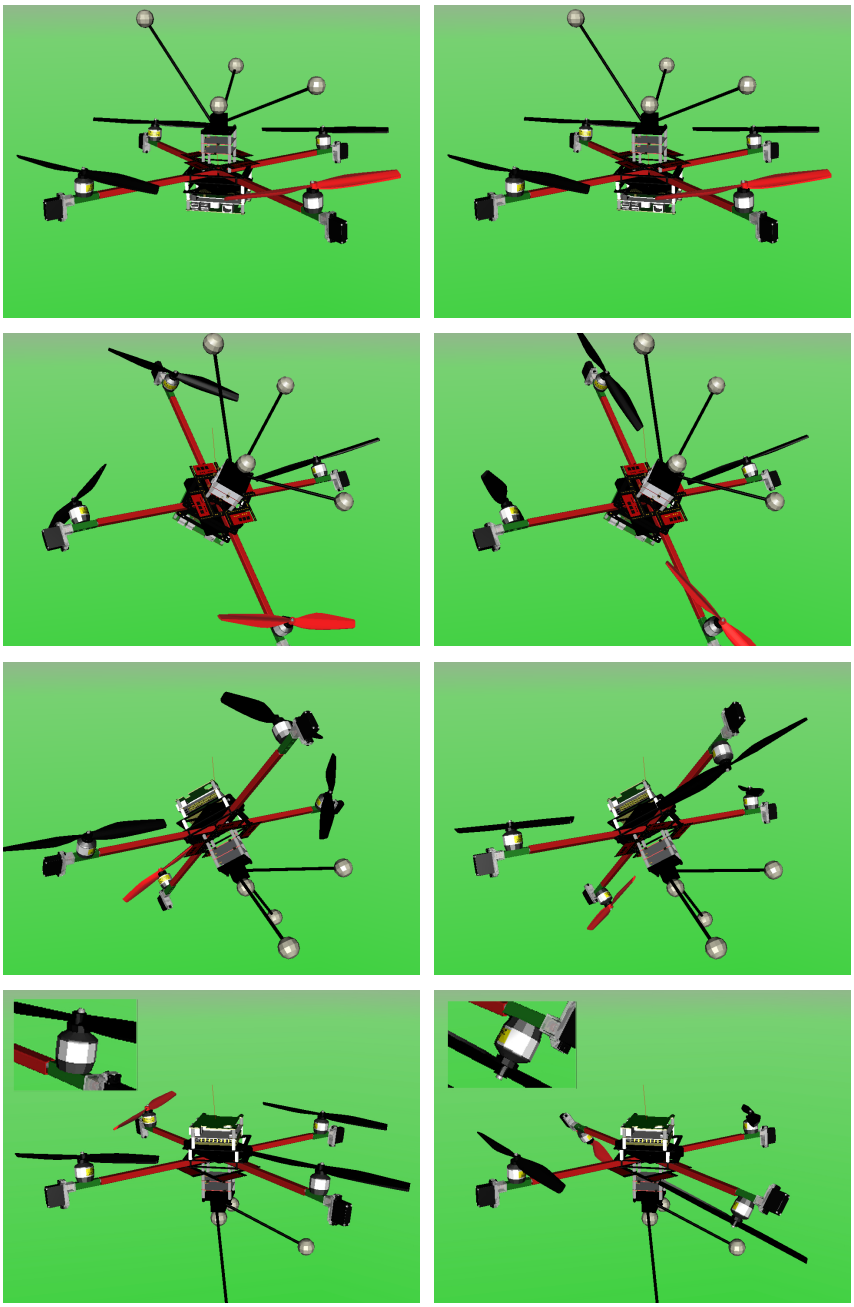

(a) (b)

Figure 5.3: Results of the first ideal simulation. Left column: holocopter motion while exploiting the null-space term (case (i)). Right column: holocopter motion without exploiting the null-space term (case (ii)). Note the large reorientation of the propeller groups in case (i) which, thanks to the action of the optimization term (3.14), end up in a full 'upright' position (minimum energy consumption) w.r.t. case (ii)

lying at a height of $z = 1.0$ m from ground, i.e.,

$$\boldsymbol{p}_d(t) = \begin{bmatrix} 0.5\sin(0.135t) \\ 0.7\sin(0.27t) \\ 1 \end{bmatrix} [m], \tag{5.1}$$

see Fig. 5.4(a).

As for the rotation about $\boldsymbol{Y}_B$, Fig. 5.4(b) depicts the chosen profile for the pitch angle $\theta(t)$. The main quantities of interest are in this case:

- Maximum speed along the trajectory: $v_{max} = 0.20\ \frac{m}{s}$
- Maximum acceleration along the trajectory: $a_{max} = 0.05\ \frac{m}{s^2}$
- Amplitude of the sinusoidal rotation: $\theta_{max} = 0.17\ rad$
- Maximum rotational velocity: $\dot{\theta}_{max} = 0.05\ \frac{rad}{s}$
- Maximum rotational acceleration: $\ddot{\theta}_{max} = 0.02\ \frac{rad}{s^2}$

Figures 5.5(a–b) show the position and orientation tracking errors ($\boldsymbol{e}_P(t)$, $\boldsymbol{e}_R(t)$) while performing the task, with maximum values of $e_{Pmax} \simeq 0.28$ mm and $e_{Rmax} \simeq 0.0035$ rad. Again, these errors can be ascribed to the unmodeled internal gyroscopic and inertial forces due to the propeller group rotations w.r.t. the body frame. The behavior of $\boldsymbol{\alpha}(t)$ is also reported in Fig. 5.5(c). The results of the simulation demonstrate again the tracking abilities of the proposed controller as the position and orientation errors keep very small values while following this more complex trajectory.

5.1.3 Squared trajectory

In the last simulation, we addressed the case of a more complex trajectory following a square path with vertexes $\{V_1, V_2, V_3, V_4, V_5\}$. Each vertex was associated with the following desired positions and orientations[2]

- $\boldsymbol{V}_1$: $\boldsymbol{p}_d = [0\ 0\ 0]^T$, $\boldsymbol{\eta}_d = [0\ \ 0\ \ 0]^T$

[2]Here, for the sake of clarity, we represent orientations by means of the classical roll/pitch/yaw Euler set $\boldsymbol{\eta} \in \mathbb{R}^3$.

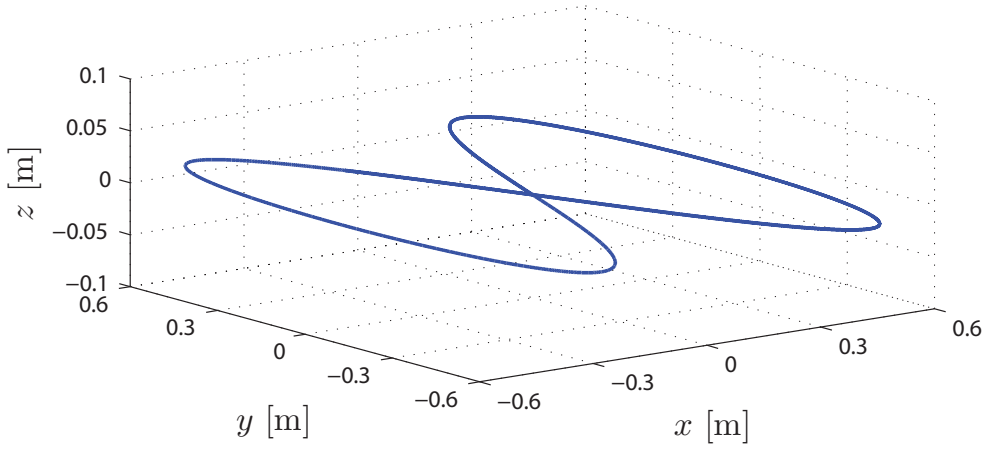

(a)

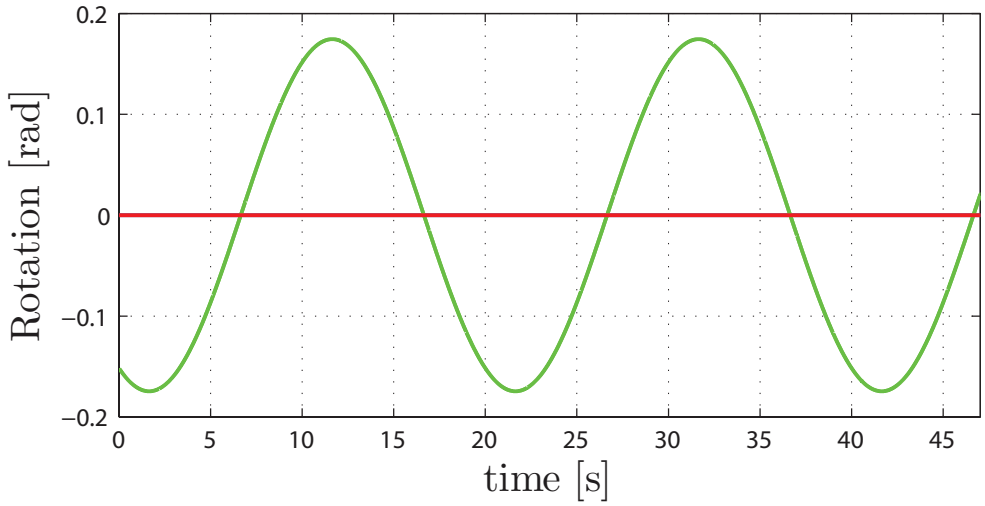

(b)

Figure 5.4: Results of the second ideal simulation. (a) - Desired eight-shape trajectory; (b) - Desired sinusoidal orientation over time, red line indicates desired pitch angle θ

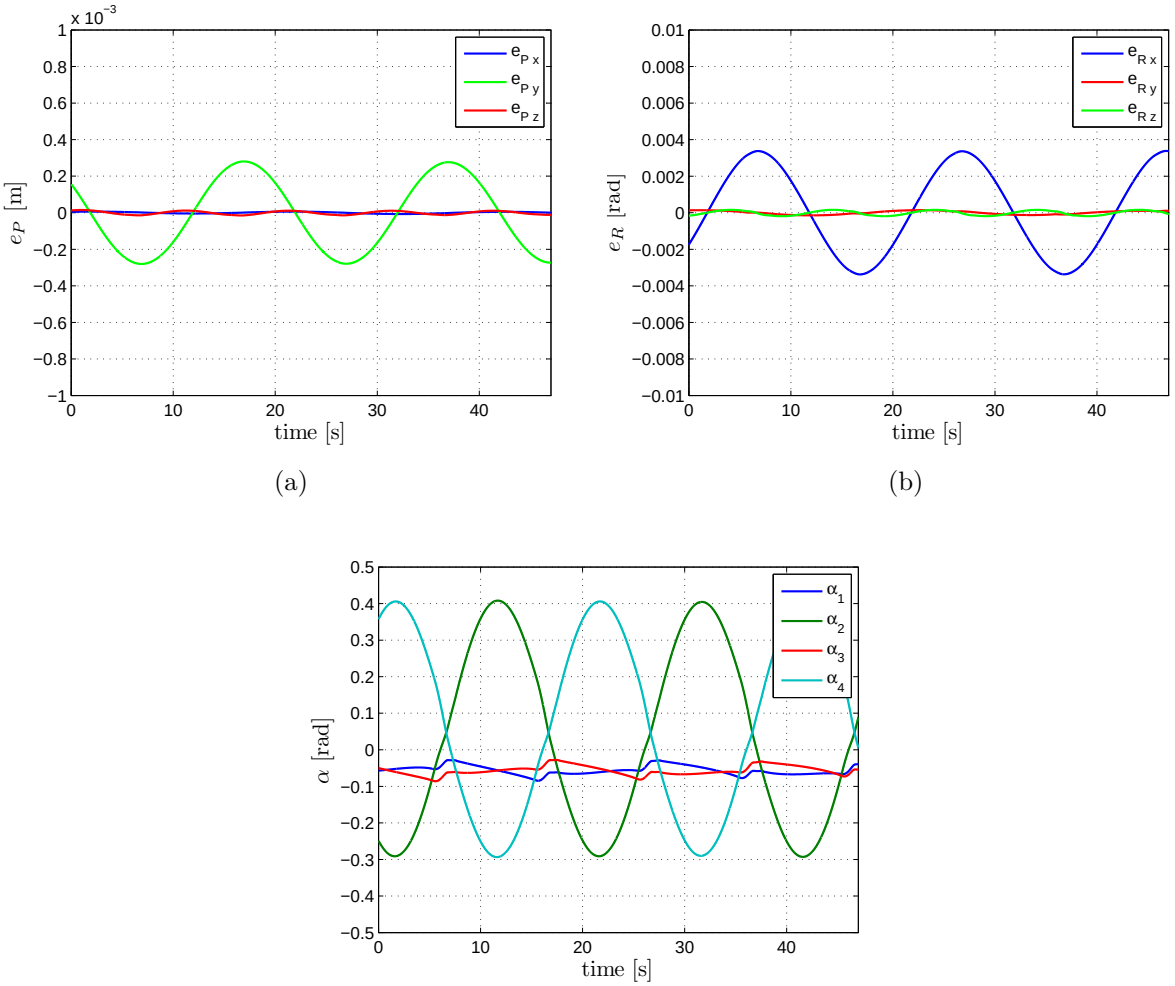

Figure 5.5: Results of the second ideal simulation. (a) Position tracking error $\boldsymbol{e}_P(t)$; (b) Orientation tracking error $\boldsymbol{e}_R(t)$; (c) behavior of the tilt angles $\boldsymbol{\alpha}(t)$ while tracking the trajectory

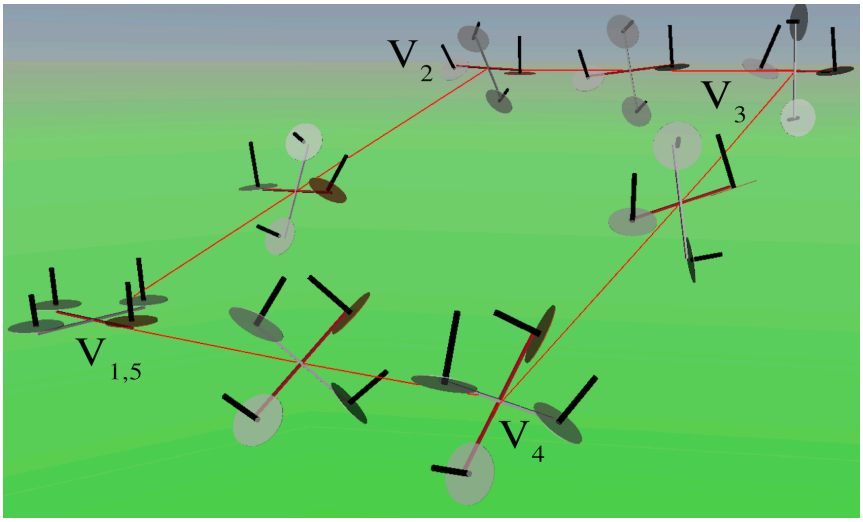

Figure 5.6: Trajectory (red line) with the holocopter visualized in according orientations during the maneuver

- $\boldsymbol{V}_2$: $\boldsymbol{p}_d = [0\ 3\ 1]^T$, $\boldsymbol{\eta}_d = [0\ \ -\pi/2\ \ 0]^T$
- $\boldsymbol{V}_3$: $\boldsymbol{p}_d = [2\ 3\ 1]^T$, $\boldsymbol{\eta}_d = [-\pi/4\ \ 0\ \ -\pi/4]^T$
- $\boldsymbol{V}_4$: $\boldsymbol{p}_d = [2\ 0\ 0]^T$, $\boldsymbol{\eta}_d = [-1.41\ \ -1.08\ \ 0.25]^T$
- $\boldsymbol{V}_5$: $\boldsymbol{p}_d = [0\ 0\ 0]^T$, $\boldsymbol{\eta}_d = [0.31\ \ -1.08\ \ 0.25]^T$

which were traveled along with rest-to-rest motions with maximum linear/angular velocities of 1 [m/s] and 1 [rad/s], and maximum linear/angular accelerations of 1 [m/s^2] and 0.2 [rad/s^2]. Figure 5.6 shows a series of snapshots illustrating the overall motion, while Figs. 5.7(a–d) show the desired trajectory ($\boldsymbol{p}_d(t)$, $\boldsymbol{\eta}_d(t)$), and the tracking errors ($\boldsymbol{e}_p(t)$, $\boldsymbol{e}_R(t)$). Note again how the tracking errors keep limited as before despite the more complex motion involving several reorientations of the propellers. This confirms again the validity of the controller proposed in the previous Section. The interested reader can also refer to the video attached to the paper for a more exhaustive illustration of the quadrotor motion capabilities.

5.2 Realistic Simulations

As explained, the 'realistic' simulations of this section have been obtained by including in the holocopter model all the non-idealities of our real prototype, in particular by replicating

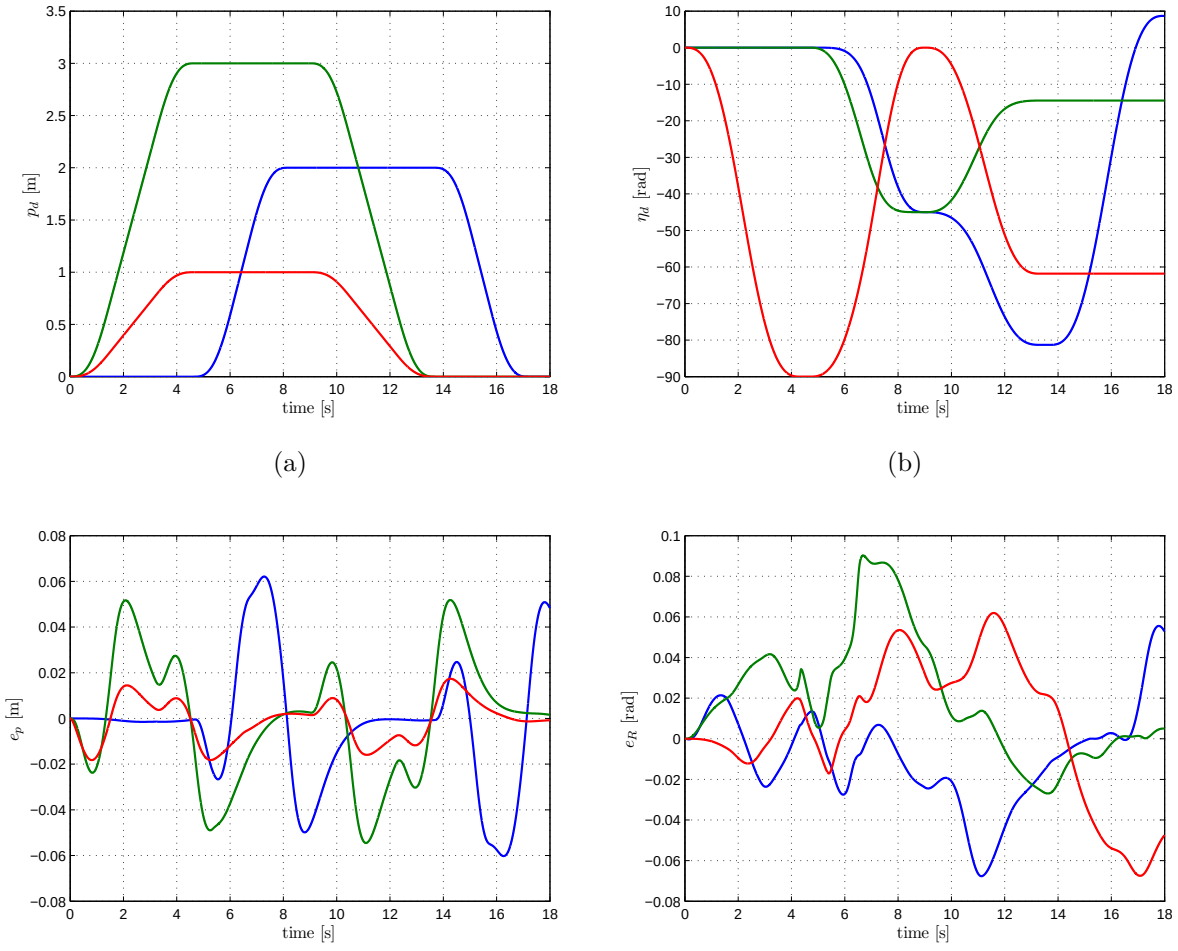

Figure 5.7: Fig. 5.7-a: Desired position p_d in x, y and z; Fig. 5.7-b: Desired orientation η in roll, pitch and yaw; Fig. 5.7-c: Position tracking error e_p; Fig. 5.7-c: Orientation tracking error e_R;

the various signal and control frequencies (e.g., motion capture frequency at 200 Hz, servo motor frequency at 70 Hz) and delays (e.g., servo motor delay of 18 ms). In addition, we also considered the noise of onboard sensor readings (gyroscopes, accelerometers and measurement of angles $\boldsymbol{\alpha}$), of the actuators (servo and propeller motors), and of the motion capture system by either obtaining the noise characteristics from data sheets, or via a preliminary off-line identification. Finally, the prediction scheme of Sect. 4.1.4 was implemented in the control loop.

To identify the noise level of the used motion capture system two experiments have been conducted. In the first experiment the position and orientation of a static object has been measured over time while in the second experiment the object was in motion. The standard variation of the position and orientation has been calculated in both cases. For the static case the noise has been found as being negligible with a standard deviation of

$$V(p_{static}) = \begin{bmatrix} 2.7472e^{-10} \\ 5.1316e^{-10} \\ 2.3642e^{-10} \end{bmatrix} [\mathrm{m}^2], V(R_{static}) = \begin{bmatrix} 1.6769e^{-08} \\ 1.7920e^{-08} \\ 1.5669e^{-08} \end{bmatrix} [\mathrm{rad}^2]. \tag{5.2}$$

For the dynamic case the standard deviation has been found as

$$V(p_{dynamic}) = \begin{bmatrix} 4.5375e^{-4} \\ 4.4425e^{-4} \\ 2.2471e^{-7} \end{bmatrix} [\mathrm{m}^2], V(R_{dynamic}) = \begin{bmatrix} 7.7348e^{-7} \\ 8.1188e^{-7} \\ 1.0425e^{-4} \end{bmatrix} [\mathrm{rad}^2]. \tag{5.3}$$

Here the error is not negligible anymore. The simulated MoCap position and orientation data have thus been modeled with a standard deviation according to the values obtained from the lalter case.

Despite assessing the effects of these non-idealities on the overall flight performance, the results of this section are also helpful for saving development time as they allow a pre-tuning of the various control gains for the deployment on the real prototype, and the identification of the most influential parameters to be optimized in view of a second-generation prototype.

5.2.1 Rotation on Spot

Because of the limited range of the tilting angles $\boldsymbol{\alpha}$ in the real prototype, it is not possible to perform a full rotation on the spot as in the previous ideal case of Sect. 5.1.1. Therefore

we opted for a (more feasible) sinusoidal rotation around the $\boldsymbol{Y}_B$-axis (pitch), i.e., with $\boldsymbol{R}_d(t) = \boldsymbol{R}_Y(\theta(t))$ with $\theta_{max} = 0.436$ rad and $\dot{\theta}_{max} = 0.07$ rad/s. The initial conditions were set to hovering ($\boldsymbol{p}(t_0) = \mathbf{0}$, $\dot{\boldsymbol{p}}(t_0) = \mathbf{0}$, $\boldsymbol{R}(t_0) = \mathbf{I}_3$, $\boldsymbol{\omega}_B(t_0) = \mathbf{0}$, $\boldsymbol{\alpha}(t_0) = \mathbf{0}$, and $\boldsymbol{w}(t_0) = w_{rest}$), and the controller gains were chosen as $\boldsymbol{K}_{p_1} = 30\mathbf{I}_3$, $\boldsymbol{K}_{\omega_1} = 55.5\mathbf{I}_3$, $\boldsymbol{K}_{p_2} = 300\mathbf{I}_3$, $\boldsymbol{K}_{\omega_2} = 1027\mathbf{I}_3$, $\boldsymbol{K}_{p_3} = 1000\mathbf{I}_3$, $\boldsymbol{K}_{\omega_3} = 6331\mathbf{I}_3$.

The results are reported in Fig. 5.8(a–d): Fig. 5.8(a) shows the behavior of the quadrotor orientation during flight (blue - roll, green - pitch, red - yaw) and Fig. 5.8(b) the behavior of the orientation error $\boldsymbol{e}_R(t)$. The maximum rotation errors are 0.240 rad (roll), 0.079 rad (pitch), and 0.144 rad (yaw). Figure 5.8(c) shows the behavior of the position tracking error $\boldsymbol{e}_P(t)$ characterized by a mean value $\text{avg}(\|\boldsymbol{e}_P(t)\|) \approx 1.6$ cm and a maximum value $\max(\|\boldsymbol{e}_P(t)\|) \approx 4.4$ cm. Finally, Figure 5.8(d) shows the behavior of the tilting angles $\boldsymbol{\alpha}(t)$ over time.

Therefore, despite the (expected) worse overall performance w.r.t. the 'ideal' case, in this 'realistic' case the holocopter is still able to fulfill the assigned motion task with a good enough accuracy.

5.2.2 Eight-shape trajectory

In this simulation we considered the same eight-shape trajectory of Sect. 5.1.2. Figures 5.9(a–b) report the behavior of the position and orientation error vectors ($\boldsymbol{e}_P(t)$, $\boldsymbol{e}_R(t)$) over time. The average position tracking error results about 0.034 m with a maximum of 0.050 m. The maximum rotation errors are 0.097 rad (roll), 0.061 rad (pitch), and 0.039 rad (yaw). Finally, Fig. 5.9(c) shows the behavior of the tilting angles $\alpha_i(t)$ while following the trajectory.

It is interesting to compare these results with those of the 'ideal' simulation of Sect. 5.1.2 (Figs. 5.5(a–c)): again, the overall tracking performance results degraded w.r.t. the ideal case, although the holocopter can still realize the task with a sufficient accuracy. Also, note how the angles $\alpha_i(t)$ in Fig. 5.9(c) follow essentially the same behavior as those of the ideal case in Fig. 5.5(c) despite the higher noise level present in the system.

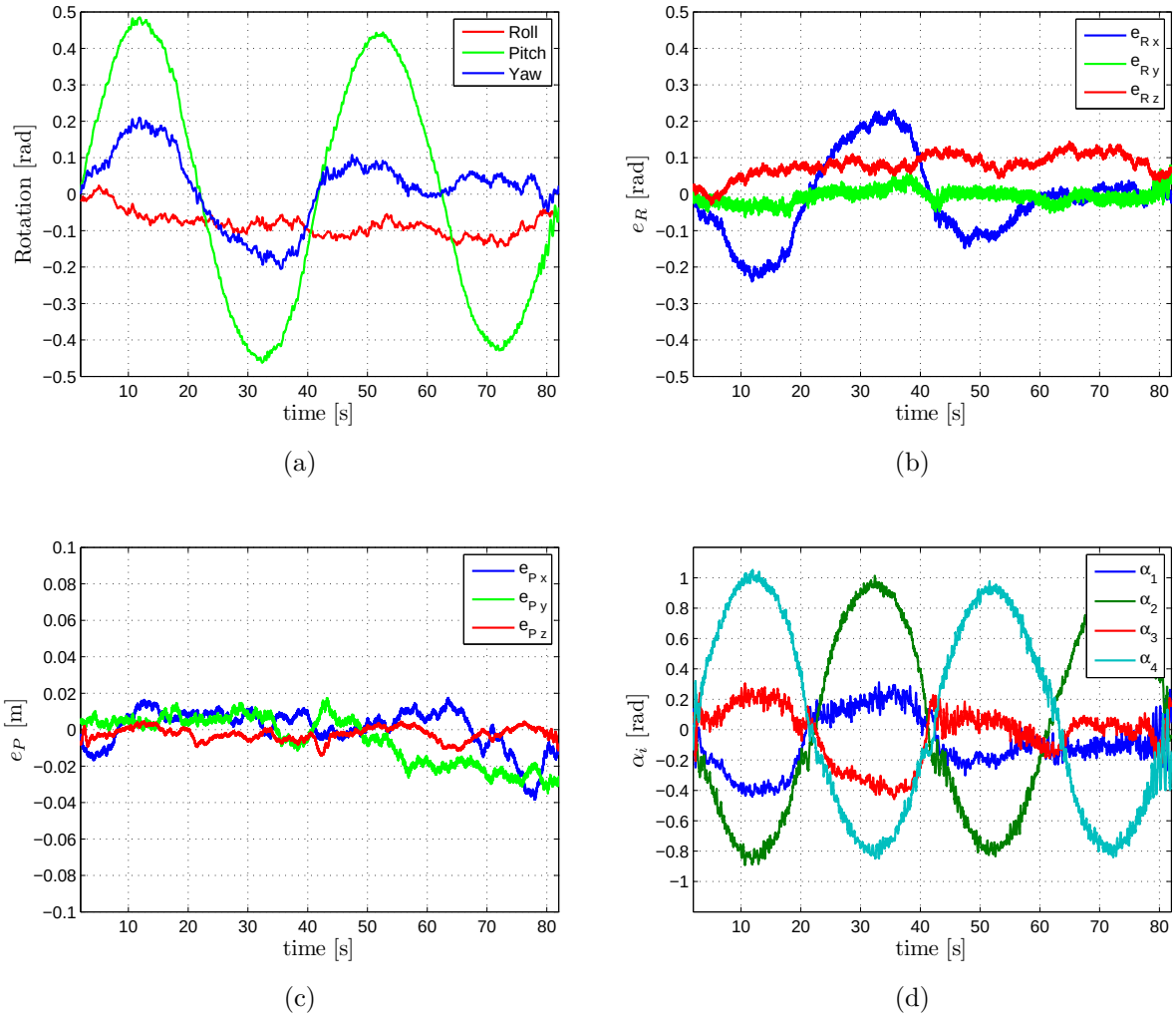

Figure 5.8: Results of the first realistic simulation. Rotation on the spot around the $\boldsymbol{Y}_B$-Axis: (a) Orientation of the main body B; (b–c) orientation tracking error $\boldsymbol{e}_R(t)$ and position tracking error $\boldsymbol{e}_P(t)$; (d) behavior of the tilting angles $\boldsymbol{\alpha}(t)$

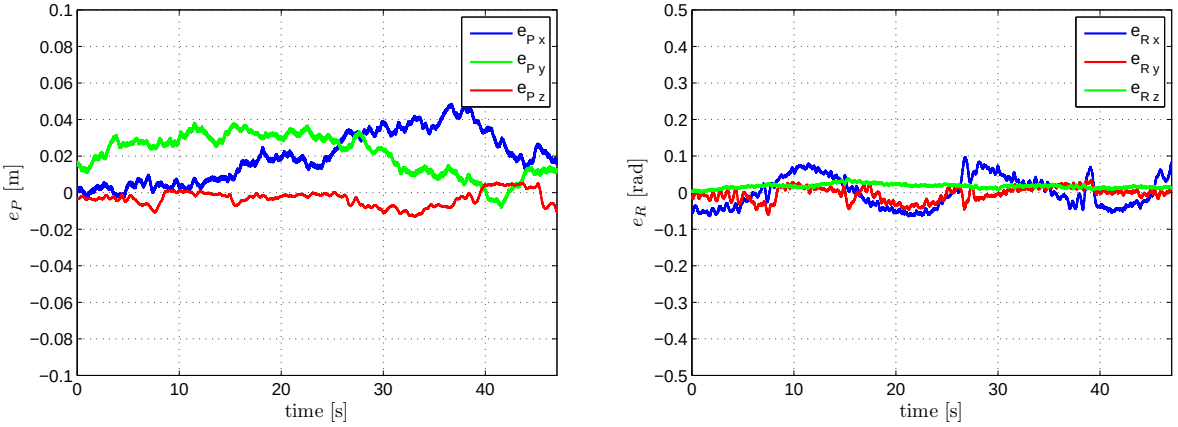

(a)

(b)

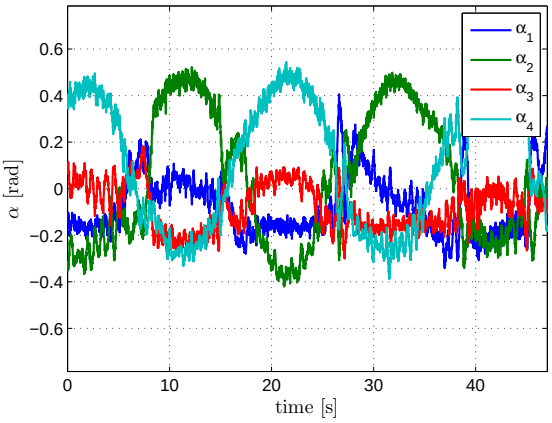

(c)

Figure 5.9: Results of the second realistic simulation. (a) Position tracking error $\boldsymbol{e}_P(t)$; (b) Orientation tracking error $\boldsymbol{e}_R(t)$; (c) behavior of the tilting angles $\boldsymbol{\alpha}(t)$

5.2.3 Effect of servo control frequency

As previously stated, the low control rate and the delayed response of the employed servo motors are expected to be the main cause of the flight performance degradation in the realistic case (and, of course, in the real prototype). The servo motors are controlled via a pulse-width modulated (PWM) signal with a signal length of 14 ms and a control frequency of 55 Hz. To assess the effects of these parameters, we ran several instances of the previous realistic simulation of Sect. 5.2.2 by employing increasing control frequencies and correspondingly decreasing delays for the servo motor PWM while keeping all the other parameters (e.g., control gains) constant.

As flight performance measure, we considered the mean position error $\text{avg}(\|\boldsymbol{e}_P(t)\|)$ and the standard deviation of the position error $\text{stdev}(\|\boldsymbol{e}_P(t)\|)$ during the trajectory. Figure 5.10 shows the results: with an increasing control frequency, the mean position error and the standard deviation are clearly decreasing from, e.g., $\text{avg}(\|\boldsymbol{e}_P\|)_{55\ Hz} = 0.042$ m to $\text{avg}(\|\boldsymbol{e}_P\|)_{500\ Hz} = 0.003$ m, thus approaching the performance of the 'ideal' case.

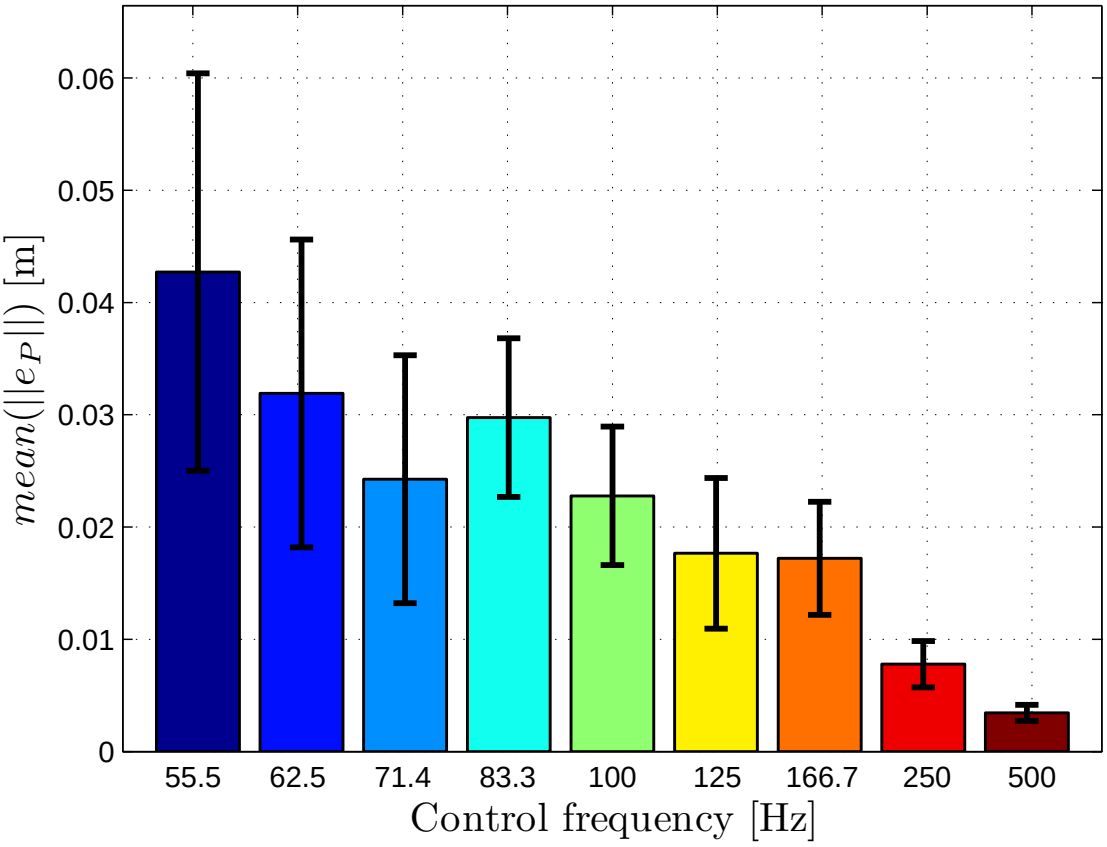

Figure 5.10: Mean position error avg($\|\boldsymbol{e}_P\|$) and standard deviation of the position error stdev($\|\boldsymbol{e}_P\|$) for different PWM control frequencies of the servo motors while following the eight-shape trajectory reported in Sect. 5.2.2

Chapter 6

Experimental Results

This chapter has been mainly reproduced from an article published in IEEE Transactions on Control Systems Technology: Ryll et al. (to be published 2014)

In this last section we finally present results from three experiments conducted with the holocopter prototype. The first experiment is a hovering task meant to show the overall performance in the simplest scenario, and also to highlight again the importance of having included the null-space optimization term (3.14) in the control strategy. The other two experiments involve instead the more complex trajectories of Sect. 5.2.1 and Sect. 5.2.2. Finally we encourage the reader to watch the video clip available at `http://youtu.be/hA-uNHW8MLE` where several holocopter maneuvers are shown along with additional details on the employed prototype.

6.1 Hovering on the spot

In the first experiment, following what was done in the 'ideal' case of Sect. 5.1.1, we show the importance of having included the minimization of the cost function $H(\boldsymbol{w})$ in the proposed controller. To this end, we report the results of a simple hovering on the spot by (i) including and (ii) not including the null-space optimization term (3.14).

The quadrotor starts from the initial state of $\boldsymbol{p}(t_0) = \mathbf{0}$, $\dot{\boldsymbol{p}}(t_0) = \mathbf{0}$, $\boldsymbol{R}(t_0) = \mathbf{I}_3$, $\boldsymbol{\omega}_B(t_0) = \mathbf{0}$, $\boldsymbol{\alpha}(t_0) = \mathbf{0}$, and $\boldsymbol{w}(t_0) = w_{rest}$, and is commanded to stay still while maintaining the desired attitude $\boldsymbol{R}_d = \mathbf{I}_3$. The gains in (3.9) and (3.11) were set to $\boldsymbol{K}_{p_1} = 30\mathbf{I}_3$, $\boldsymbol{K}_{\omega_1} = 55.5\mathbf{I}_3$, $\boldsymbol{K}_{p_2} = 300\mathbf{I}_3$, $\boldsymbol{K}_{\omega_2} = 1027\mathbf{I}_3$, $\boldsymbol{K}_{p_3} = 1000\mathbf{I}_3$, $\boldsymbol{K}_{\omega_3} = 6331\mathbf{I}_3$ (these values

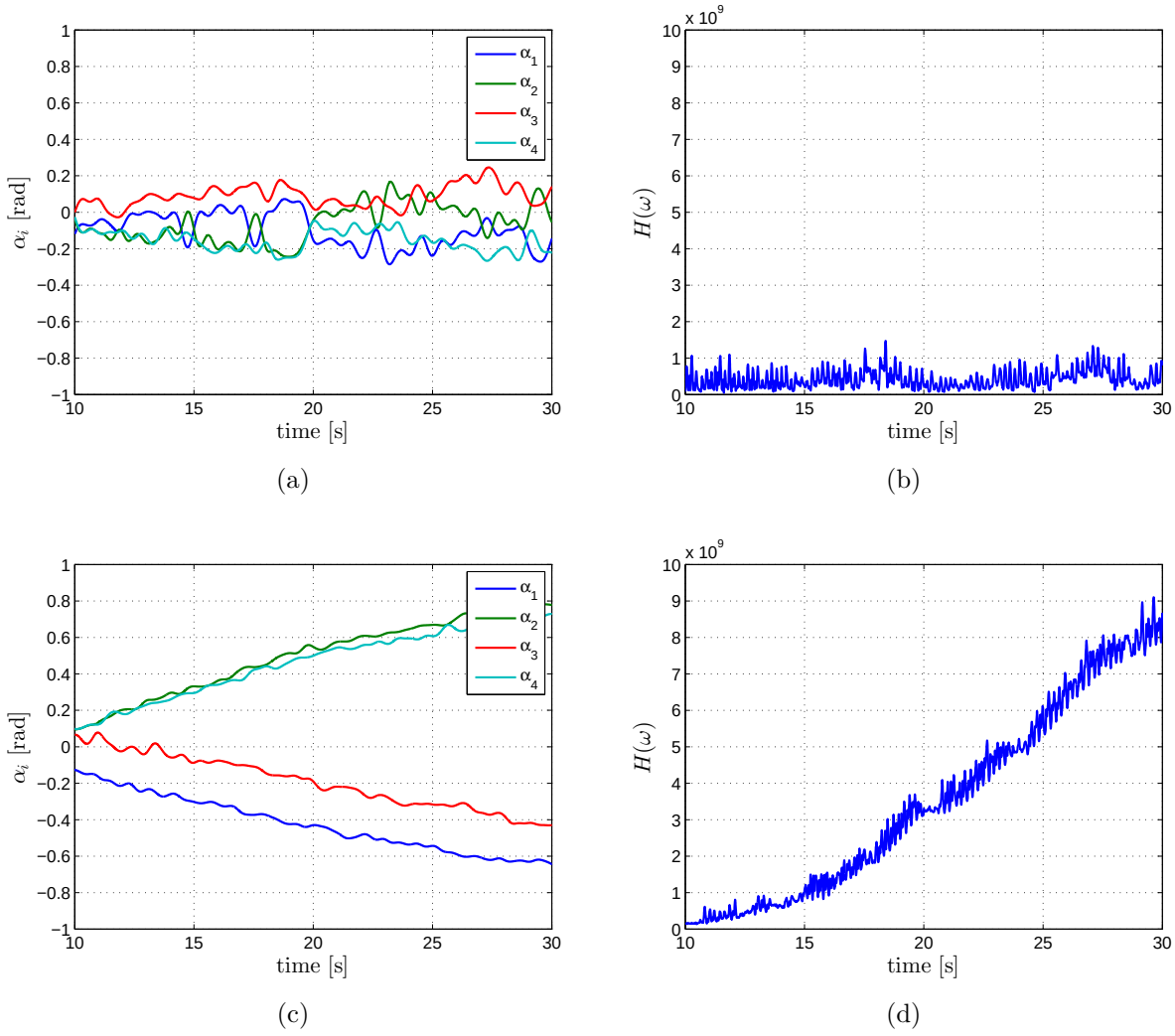

Figure 6.1: First experiment. Results for hovering on spot with (i) and without (ii) including the null-space term (3.14): (a) α_i for case (i) while hovering; (b) $H(\boldsymbol{w})$ for case (i) while hovering; (c) α_i for case (ii) while hovering; (d) $H(\boldsymbol{w})$ for case (ii) while hovering

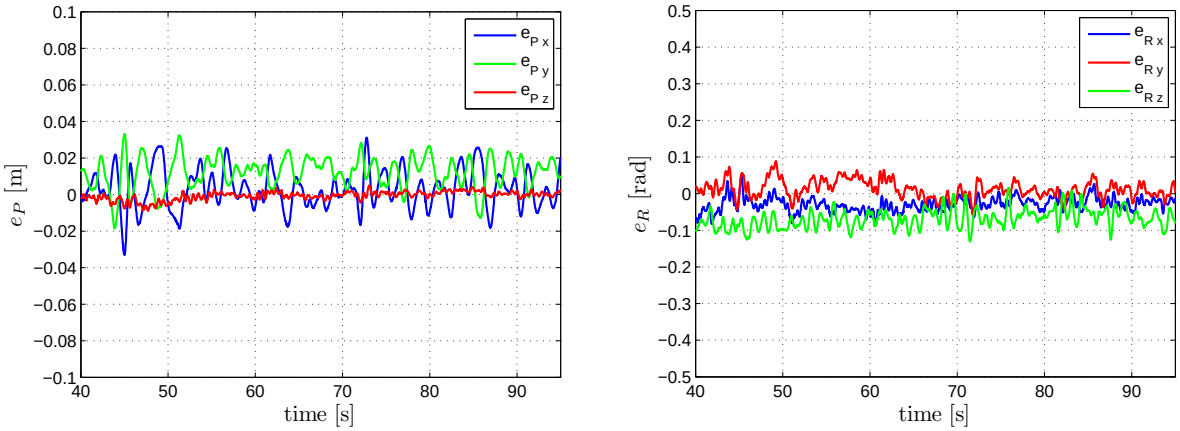

(a) (b)

Figure 6.2: First experiment. Tracking error while hovering: (a) position tracking error $\boldsymbol{e}_P(t)$; (b) orientation tracking error $\boldsymbol{e}_R(t)$

were experimentally tuned).

Figures 6.1(a–b) report the results for case (i): the angles α_i stay close to 0 rad over time, as expected for such a hovering maneuver, and $H(\boldsymbol{w})$ keeps a constant and low value as the propellers spin with a speed close to the allowed minimum. In case (ii), however, the situation looks completely different: the lack of any minimization action on $H(\boldsymbol{w})$, coupled with the presence of noise and non-idealities, makes the angles α_i to eventually diverge over time from their (expected) vertical direction and, accordingly, the value of $H(\boldsymbol{w})$ to increase as the propellers need to accelerate in order to keep the quadrotor still in place (Figs. 6.1(c–d)).

Finally, Figs. 6.2(a–b) show the position error $\boldsymbol{e}_P(t)$ and orientation error $\boldsymbol{e}_R(t)$ during the experiment. The average position tracking error is about 0.017 m with a maximum of 0.047 m. The maximum rotation errors are 0.082 rad (roll), 0.131 rad (pitch), and 0.089 rad (yaw).

6.2 Rotation on Spot

In this second experiment we replicate the 'realistic simulation' case of Sect. 5.2.1 by commanding the holocopter to follow a given orientation profile $\boldsymbol{R}_d(t)$ while remaining still in space. The initial conditions, control gains and trajectory parameters are the same as

those reported in Sect. 5.2.1.

Figures 6.3(a–d) show the results of the flight: in particular, Fig. 5.9(a) reports the quadrotor orientation during flight (blue - roll, green - pitch, red - yaw), and Fig. 5.9(b) the orientation tracking error $\boldsymbol{e}_R(t)$. The position tracking error $\boldsymbol{e}_P(t)$ is shown in Fig. 5.9(c), with a maximum of $\max(\|\boldsymbol{e}_P(t)\|) = 0.062$ m. Finally, Fig. 5.9(d) depicts the behavior of the tilting angles $\alpha_i(t)$ during the maneuver, and Fig. 6.4 the behavior of $H(\boldsymbol{w})$. As clear from the plots, this experiment involving a rotation on the spot still confirms the capabilities of the holocopter and the robustness of the proposed control strategy in coping with all the non-idealities of real-world conditions.

6.3 Eight-shape trajectory

This last experiment shows the performance of the holocopter in tracking the same eight-shape trajectory with superimposed sinusoidal rotation of Sect. 5.1.2 and Sect. 5.2.2. Figure 6.5 shows an overlay of several snapshots taken during flight.

Figure 6.6(a) reports the position tracking error $\boldsymbol{e}_P(t)$ of the holocopter while following the trajectory, while Fig. 6.6(b) reports the orientation tracking error $\boldsymbol{e}_R(t)$. The maximum position error $\max(\|\boldsymbol{e}_P(t)\|)$ while following the path was approximately 3.9 cm, with $\text{avg}(\|\boldsymbol{e}_P(t)\|) \approx 2.2$ cm. The maximum orientation errors were 0.10 rad for roll, 0.06 rad for pitch and 0.15 rad for yaw. Figures 6.6(b) shows the behavior of the tilting angles $\alpha_i(t)$. Note how these experimental results match very well those of the 'realistic' simulation of Sect. 5.2.2, thus also confirming the validity of the employed holocopter model. The interested reader is also appreciated to watch the execution of this task in the video available at `http://youtu.be/hA-uNHW8MLE`.

6.4 Combined trajectory

Finally an experiment with a combined trajectory including a vertical take-off and landing maneuver was conducted. Hereby the holocopter followed a path of predefined vertexes. Each vertex was associated with the following desired position and orientation[1]:

[1] Here, for the sake of clarity, we represent orientations by means of the classical roll/pitch/yaw Euler set $\boldsymbol{\eta} \in \mathbb{R}^3$.

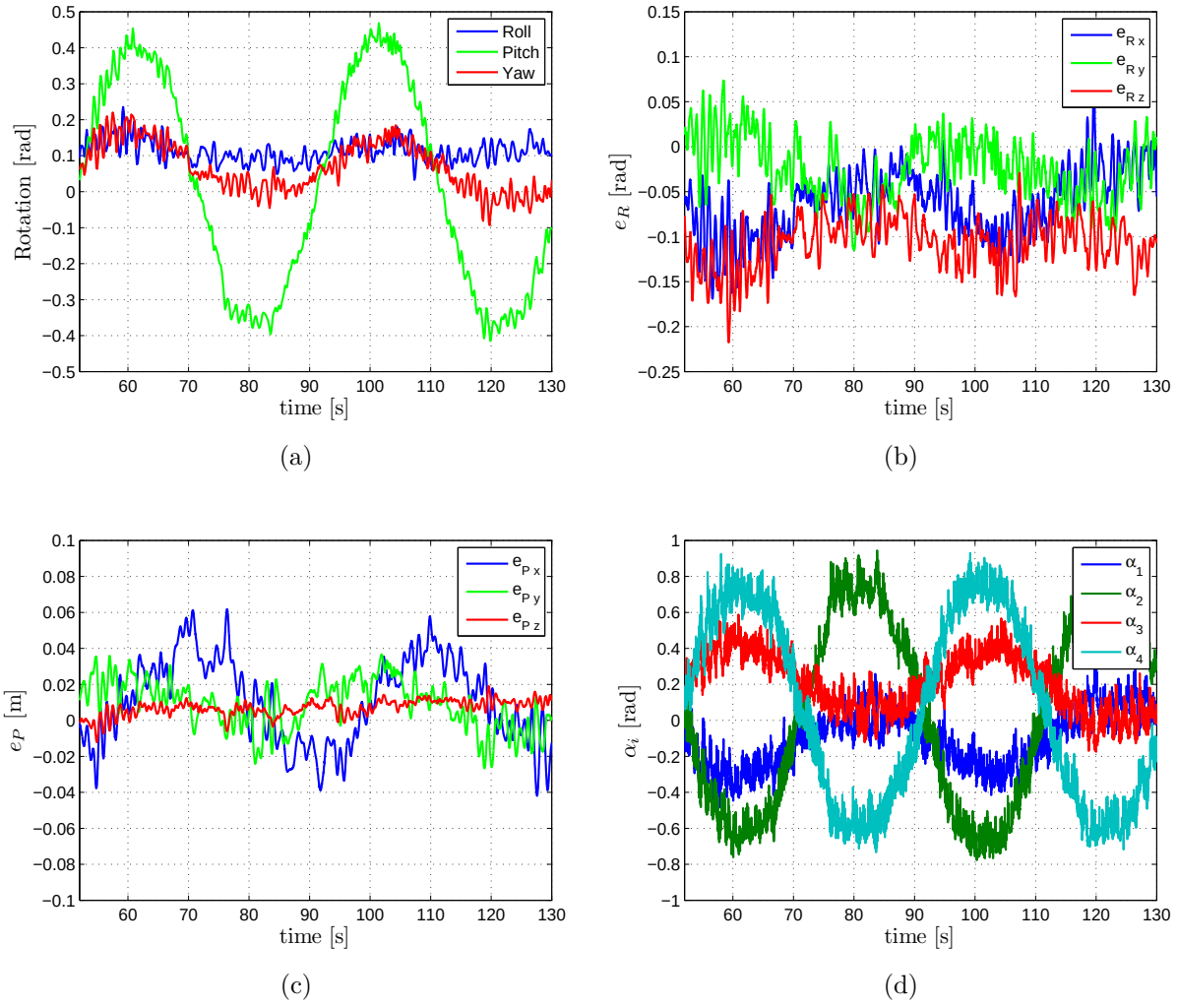

Figure 6.3: Second experiment. Rotation on the spot around the $\boldsymbol{Y}_B$-Axis: (a) Orientation of the main body B; (b) and (c) orientation error vector $\boldsymbol{e}_R(t)$ and position error vector $\boldsymbol{e}_P(t)$; (d) behavior of the tilting angles α_i

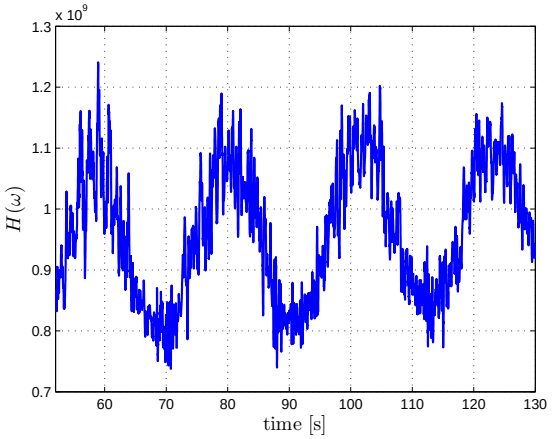

Figure 6.4: Second experiment. Behavior of $H(\boldsymbol{w})$ while rotating on the spot

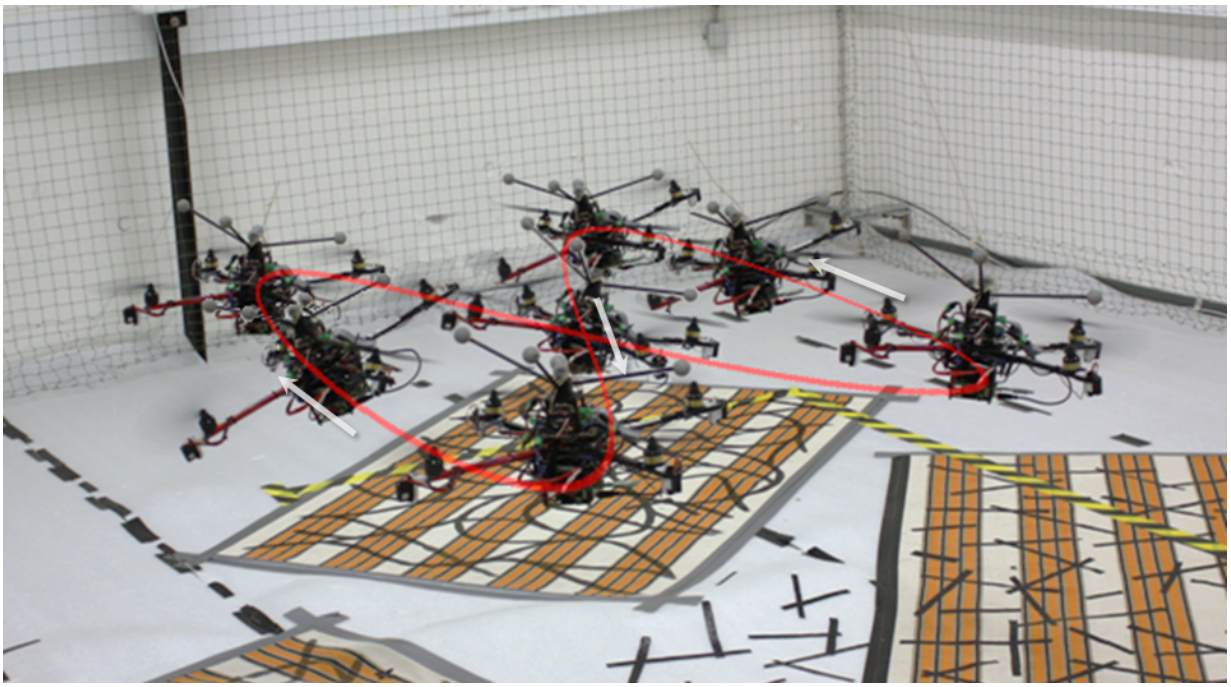

Figure 6.5: Third experiment. Overlay of several snapshots of the holocopter while performing eight-shape trajectory

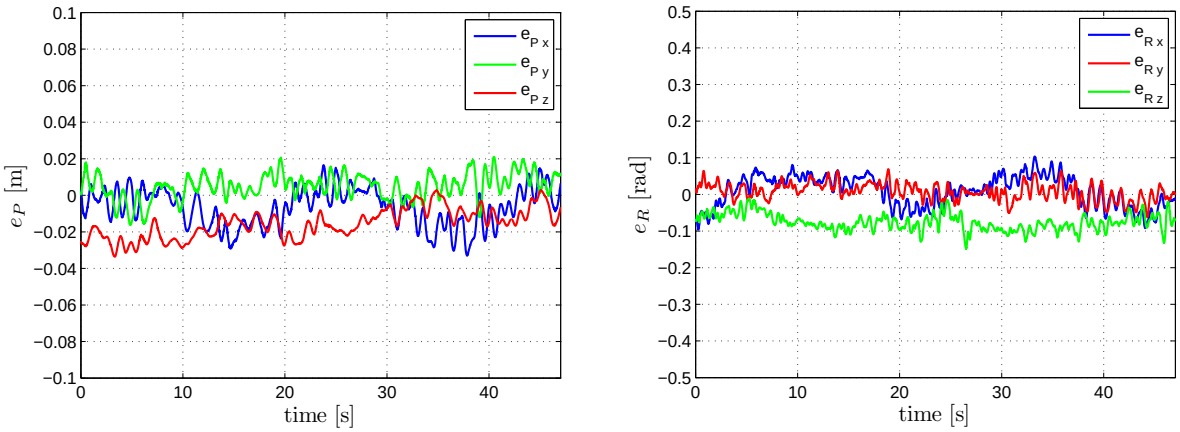

(a)

(b)

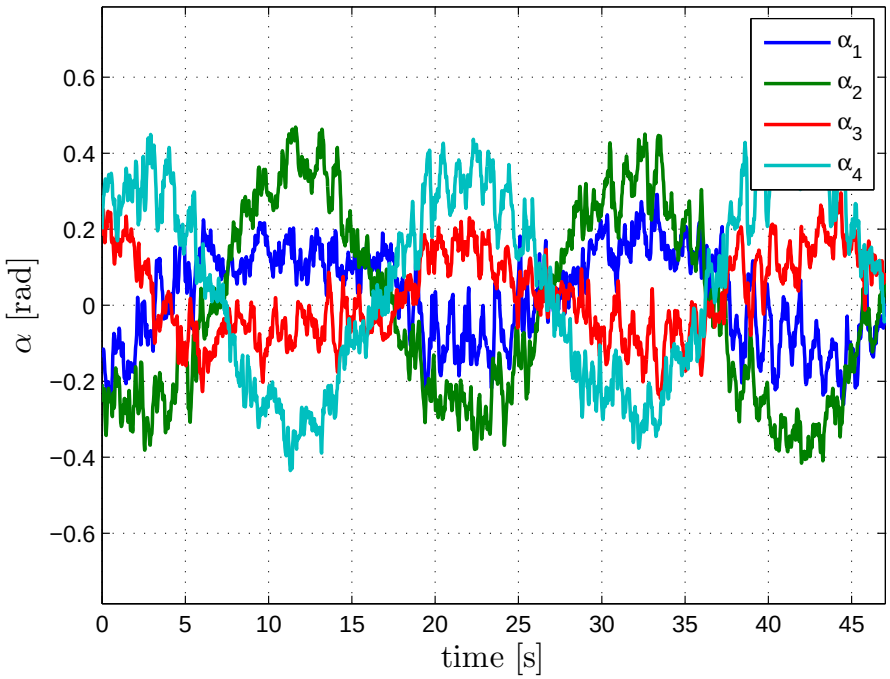

(c)

Figure 6.6: Third experiment. (a) Position tracking error e_P - x (blue), y (green) and z (red); (b) Orientation tracking error e_R - roll (blue), pitch (red) and yaw (green); (c) behavior of the tilting angles α_i

- $\boldsymbol{V}_1$: $\boldsymbol{p}_d = [0.33 \quad -0.17 \quad 0.7]^T$, $\boldsymbol{\eta}_d = [0 \quad 0 \quad 0]^T$
- $\boldsymbol{V}_2$: $\boldsymbol{p}_d = [0.33 \quad -0.17 \quad 1.0]^T$, $\boldsymbol{\eta}_d = [0 \quad 0 \quad 0]^T$
- $\boldsymbol{V}_3$: $\boldsymbol{p}_d = [0.0 \quad 0.0 \quad 1.05]^T$, $\boldsymbol{\eta}_d = [0 \quad 0 \quad 0]^T$
- $\boldsymbol{V}_4$: $\boldsymbol{p}_d = [0.0 \quad 0.0 \quad 1.05]^T$, $\boldsymbol{\eta}_d = [\frac{\pi}{12} \quad 0 \quad 0]^T$
- $\boldsymbol{V}_5$: $\boldsymbol{p}_d = [0.0 \quad 0.0 \quad 1.05]^T$, $\boldsymbol{\eta}_d = [\frac{\pi}{12} \quad 0 \quad 2\pi]^T$
- $\boldsymbol{V}_6$: $\boldsymbol{p}_d = [0.0 \quad 0.0 \quad 1.05]^T$, $\boldsymbol{\eta}_d = [0 \quad 0 \quad 2\pi]^T$
- $\boldsymbol{V}_7$: $\boldsymbol{p}_d = [0.33 \quad -0.17 \quad 1.15]^T$, $\boldsymbol{\eta}_d = [0 \quad 0 \quad 2\pi]^T$
- $\boldsymbol{V}_8$: $\boldsymbol{p}_d = [0.33 \quad -0.17 \quad 0.7]^T$, $\boldsymbol{\eta}_d = [0 \quad 0 \quad 2\pi]^T$

The performed trajectory is plotted in figure 6.7-(a) and (b). The take-off and landing platform was located at the position $p_d = [0.33 \quad -0.17 \quad 0.8]^T$. The actually desired landing and starting positions V_1 and V_8 could therefore not be achieved. The mismatch between desired and actual landing position was consciously chosen to achieve a more stable behavior in the lift-off and touch-down moment. The maximum translational velocity is $||\dot{\boldsymbol{p}}_{B_{max}}|| = 0.21 \ \frac{\mathrm{m}}{\mathrm{s}}$ and the maximum rotational velocity during the trajectory is $||\boldsymbol{\omega}_{B_{max}}|| = 0.26 \ \frac{\mathrm{rad}}{\mathrm{s}}$.

The maximum position error $\max(\|\boldsymbol{e}_P(t)\|)$ while following the path was approximately 9.8 cm, with $\mathrm{avg}(\|\boldsymbol{e}_P(t)\|) \approx 3.7$ cm. The maximum orientation errors were 0.10 rad for roll, 0.25 rad for pitch and 0.07 rad for yaw. Figure 6.7-(d) shows the advanced and continuous reorientation of the servo motors.

6.5 Summary

In this section we presented a broad variety of experimental results starting from 'Hovering on Spot'-maneuvers where the benefit and importance of the optimization from Section 3.2 over simple trajectories (see Sect. 6.2) although impossible for common quadrotors to finally more advanced trajectories with multiple overlaid transitions and rotation including take-off and landing in Section 6.4. We showed that the presented controller from Section 3 is able to control the holocopter main body independently in position and orientation as originally

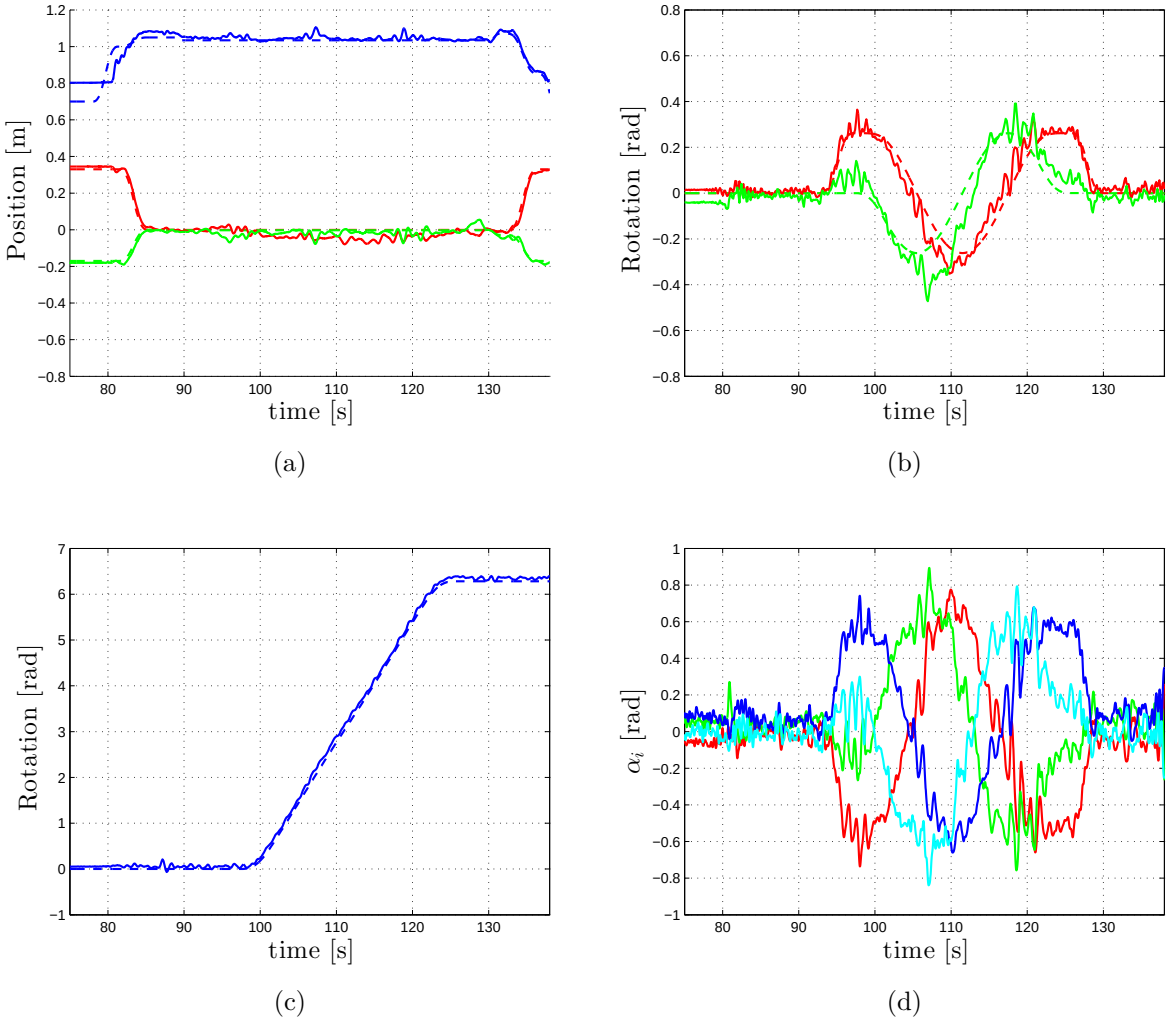

Figure 6.7: (a) - Dashed line: Desired position in x (red), y (green) and z (blue); Solid line: Actual position in x (red), y (green) and z (blue). (b) - Dashed line: Desired attitude in roll (red) and pitch (green); Solid line: Actual attitude in roll (red) and pitch (green). (c) - Dashed line: Desired yaw attitude; Solid line: Actual yaw attitude. (d) - Servo motor orientation: α_1 (red), α_2 (green), α_3 (blue) and α_4 (cyan)

proposed. With this section the experimental results end and we will now present an outline on possible interaction control scenarios with the holocopter.

Chapter 7

Perspectives on Aerial Interaction

Aerial manipulation of the environment and cooperative interaction with other robots (UAVs or ground robots) is an emerging field of research. In cooperative arrangements, UAVs are used to collectively transport higher payloads (e.g. Fink et al. (2010)) or to manipulate a single airborne object (e.g. Michael et al. (2009) and Sreenath and Kumar (2013)). Different approaches aim to use a single UAV to interact with the environment either for inspection scenarios where a constant force has to be applied to an object (see Forte et al. (2012a)) or more general a single UAV can also be used to apply arbitrary forces on an object (see Gioioso et al. (2013)). A general drawback of standard UAVs for manipulation is their intrinsic underactuation which results in a limited interaction with the environment. As in the aforementioned publications several UAVs are needed to manipulate an object or only a subset of possible forces and torques can be applied on an object. This limitation does not hold for the holocopter where one clearly benefits from the full actuation of the main body B. This final chapter will provide some guidelines for possible future applications involving the interaction between the holocopter and the physical world.

To get an insight on the importance of a well designed control scheme for interaction tasks, one can note that tracking a desired end-effector trajectory will always imply presence of some tracking errors (especially in the context of aerial manipulation). In an interaction task this may result in a contact force and an additional deviation of the end effector position. A standard control scheme will try to generate forces which attempt to reduce the tracking error, and this will additionally increase the contact forces. A high stiffness

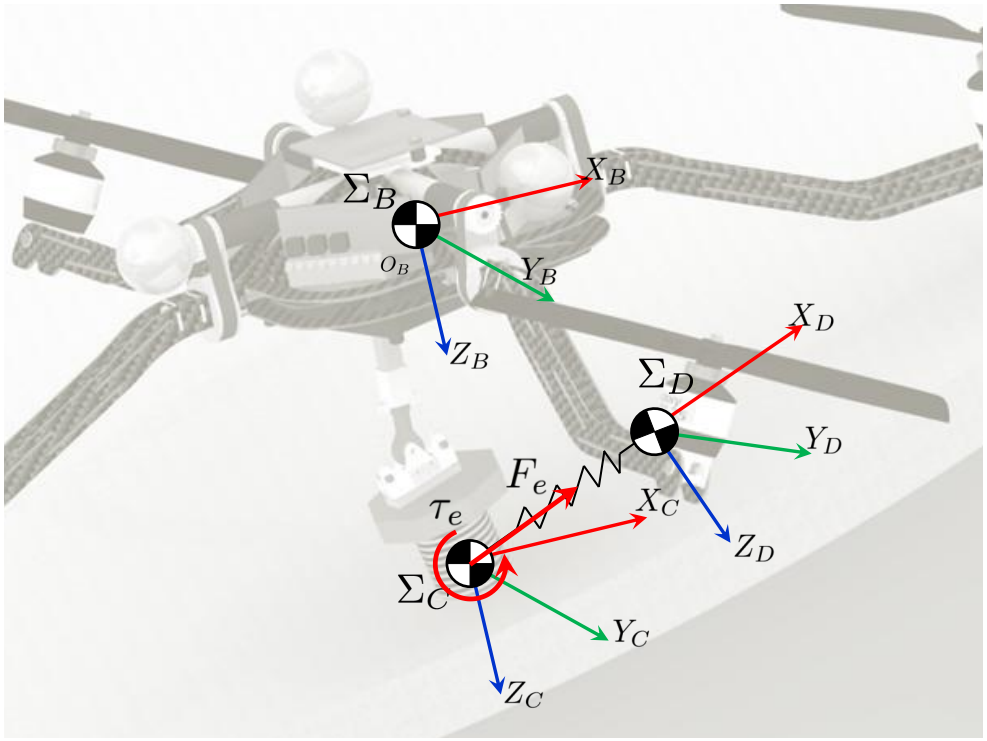

Figure 7.1: Position of the desired frame Σ_D and the compliant frame Σ_C with respect to the holocopter body in the presence of external forces $\boldsymbol{F}_e$ and torques $\boldsymbol{\tau}_e$

of the end-effector and the environment as well as high gains for the position control will additionally raise the contact forces. Finally this might lead to damage of the robot, the end-effector or the environment. For this reason a compliant behavior is needed during interaction scenarios as clearly discussed in Siciliano and Khatib (2008).

7.1 Admittance control

The control design of the holocopter introduced in Section 3 can be easily adapted for position based interaction control schemes that are often used in industrial robot applications. Typical position based compliant control schemes are impedance and admittance control. Due to the difficulty of gain tuning in the case of impedance control, an admittance control scheme will be discussed in the following. Hereby an additional reference frame the compliant frame Σ_C is introduced. A desired frame Σ_D corresponds to the desired end-effector position.

The coupling between the desired frame and the compliant frame is described as a

six-dimensional mass-spring-damper mechanical system. In case of no acting forces or torques on the desired frame the compliant frame will coincide with the latter one.

Based on Siciliano and Khatib (2008) chapter 7, one has

$$\boldsymbol{K}_M \boldsymbol{\Delta \dot{v}^c}_{dc} + \boldsymbol{K}_D \boldsymbol{\Delta v}^c_{dc} + \boldsymbol{h}^c_\Delta = \boldsymbol{h}^c \tag{7.1}$$

where h^c_Δ is the elastic wrench in the presence of a finite displacement between the desired frame Σ_d and the compliant frame Σ_c:

$$\boldsymbol{h}^c_\Delta = \boldsymbol{h}_{\Delta t} + \boldsymbol{h}_{\Delta o} \tag{7.2}$$

with

$$\boldsymbol{h}_{\Delta t} = \begin{bmatrix} K'_{Pt} \Delta p_{dc} \\ K''_{Pt} \Delta p_{dc} \end{bmatrix} \tag{7.3}$$

with

$$\boldsymbol{K''} = \frac{1}{2} S(\boldsymbol{\Delta p}_{dc}) \boldsymbol{R}_d \boldsymbol{K}_{Pt} \boldsymbol{R}_d^T \tag{7.4}$$

and

$$\boldsymbol{h}_{\Delta o} = \begin{bmatrix} 0 \\ \boldsymbol{K'}_{Po} \boldsymbol{R}_c^T \boldsymbol{\epsilon}^c_{dc} \end{bmatrix} \tag{7.5}$$

.

Furthermore K_M and K_D are (6×6) symmetric and positive definite matrices, $\Delta \dot{v}^c_{dc} = \dot{v}^c_d - \dot{v}^c_c$, $\Delta v^c_{dc} = v^c_d - v^c_c$, $\dot{v}^c_d$ and v^c_d are the acceleration and the velocity of a desired frame Σ_d referred to the compliance frame Σ_c.

The constant K_M represents a true 6-DOF mechanical impedance in case Σ_d is constant with

$$\boldsymbol{K}_M = \begin{bmatrix} m\boldsymbol{I} & 0 \\ 0 & \boldsymbol{M} \end{bmatrix} \tag{7.6}$$

where m is an arbitrary mass and $\boldsymbol{M}$ is an arbitrary (3×3) inertia tensor. This body is attached to the virtual frame Σ_c through a 6-DOF ideal spring with stiffness matrix $\boldsymbol{K}_P$ ((6×6) symmetric and positive definite matrix) and is subject to viscous forces and moments with damping $\boldsymbol{K}_D$. If $\boldsymbol{K}_P$ and $\boldsymbol{K}_D$ are chosen as diagonal matrices a maximum decoupling between the single forces and torques is achieved. Mechanical systems with this property are called Remote Center of Compliance devices.

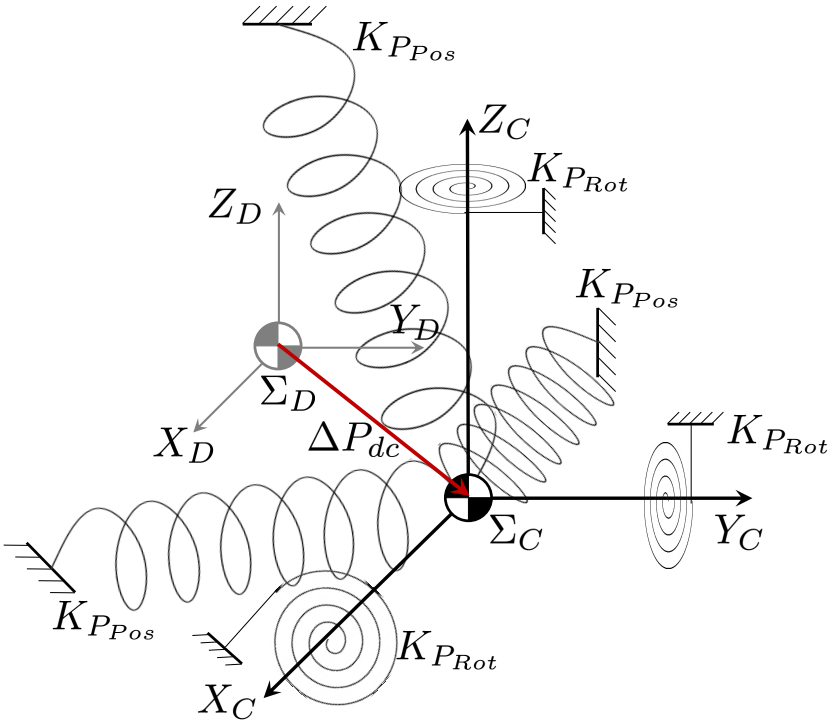

Figure 7.2: Mechanical system consisting of a 6-DOF spring system. Pure translation from desired frame O_D to compliant frame O_C due to a not visualized external wrench $\boldsymbol{h}_e$. For clarity damping components are not visualized

The arbitrary selection of m and M allows a redesign of the dynamical behavior of the holocopter. The actual mass and inertia are transparent to the interaction task. With $\boldsymbol{K}_D = diag\{K_{Dp}, K_{Dp}, K_{Dp}, K_{Dr}, K_{Dr}, K_{Dr}\}$, $\boldsymbol{K}_D = diag\{K_{Pp}, K_{Pp}, K_{Pp}, K_{Pr}, K_{Pr}, K_{Pr}\}$ and $\boldsymbol{K}_M = diag\{m, m, m, M_1, M_2, M_3\}$ equation (7.1) results in

$$\begin{bmatrix} m\ddot{p}_{cx}(t) \\ m\ddot{p}_{cy}(t) \\ m\ddot{p}_{cz}(t) \\ M_1\ddot{o}_{cx}(t) \\ M_2\ddot{o}_{cy}(t) \\ M_3\ddot{o}_{cz}(t) \end{bmatrix} = \begin{bmatrix} m\ddot{p}_{dx}(t) + K_{Dp}(\dot{p}_{dx}(t) - \dot{p}_{cx}(t)) + K_P(p_{dx}(t) - p_{cx}(t)) - F_x \\ m\ddot{p}_{dy}(t) + K_{Dp}(\dot{p}_{dy}(t) - \dot{p}_{cy}(t)) + K_P(p_{dy}(t) - p_{cy}(t)) - F_y \\ m\ddot{p}_{dz}(t) + K_{Dp}(\dot{p}_{dz}(t) - \dot{p}_{cz}(t)) + K_P(p_{dz}(t) - p_{cz}(t)) - F_z \\ M_1\ddot{o}_{dx}(t) + K_{Dr}(\dot{o}_{dx}(t) - \dot{o}_{cx}(t)) - \tau_x \\ M_2\ddot{o}_{dy}(t) + K_{Dr}(\dot{o}_{dy}(t) - \dot{o}_{cy}(t)) - \tau_y \\ M_3\ddot{o}_{dz}(t) + K_{Dr}(\dot{o}_{dz}(t) - \dot{o}_{cz}(t)) - \tau_z \end{bmatrix} \tag{7.7}$$

From (7.7) the decoupling between the single forces and torques becomes clear.

7.2 Force Observer

For closing the control loop knowledge of the reaction force and torques (wrench $\boldsymbol{h}_c$) is needed. This can be achieved by an onboard force torque sensor inside the end-effector. However this solution has several drawbacks (Iida and Ohnishi (2003), Katsura et al. (2003)), amongst others:

- High additional payload for sensor, digital measuring and evaluation system and mechanics
- Sensor noise: especially a problem on UAVs due to vibrations of the propellers
- Narrow bandwidth: due to vibrations the sensor signals have to be filtered by a low pass

A possibility to circumvent these problems is the use of a force observer. In a similar manner the state of a quadrotor is estimated in Benallegue et al. (2006) for the attitude control and in Jeong et al. (2012) for estimating external disturbances such as wind gusts. The complete admittance control scheme including an observer is presented in figure 7.3.

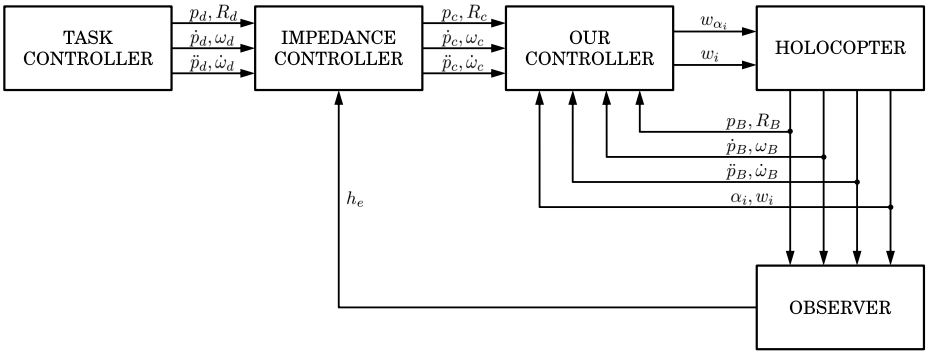

Figure 7.3: Admittance control scheme including force observer

Hereby the bandwidth of the position controller must be higher than the bandwidth of the outer admittance control loop to guarantee stability of the collective system.

A possibly simplest utilizable observer is based on the disturbance observer scheme. Hereby the reaction forces and torques have to be decoupled from the disturbance forces and torques. For a proper construction of the observer precise parameter identification is mandatory as e.g. proposed in Khalil and Sabanovic (2010a). The external reaction force can be estimated as (Ahmad (2011))

$$\boldsymbol{f}_{ext} = \frac{g_{reac}}{s + g_{reac}}(I_a^{ref} k_{tn} + g_{reac} m_n \dot{q} - V\dot{q} - C(q, \dot{q}) - G(q)) - g_{reac} m_n \dot{q} \tag{7.8}$$

where g_{reac} correspondence to a low-pass cut-off frequency, m_n is the nominal system mass and inertia. k_{tn} is the torque and force constant to the system input I_a^{ref}. From (7.8) it becomes clear that f_{ext} can be estimated only by measurements of q and $\dot{q}$ and knowledge of the system input I_a^{ref}.

7.3 Outline

The complete derivation of the force observer and the stability analysis of the entire interaction system will not be detailed here. Completion is therefore left for future work. As an outline for this work the following problems have to be tackled and special attention will be needed:

- Mismatch between center of gravity of holocopter and end-effector.

- The bandwidth of the outer loop admittance controller has to be lower than the bandwidth of the position controller. Additionally the measurements of force observer are low pass filtered to find a good balance between response and noise attenuation. These might lead to a low reaction time of the force observer.

- The measurements of $\boldsymbol{q}$ and $\dot{\boldsymbol{q}}$ together with the parameter identification might not be accurate to utilize the introduced observer. In this case either an observer without any sensor information could be used (see Khalil and Sabanovic (2010b)) or a parameter non-sensitive observer scheme would be required (e.g. sliding mode observer).

Chapter 8

Conclusions

In this Ph.D. thesis a novel overactuated quadrotor UAV - the 'holocopter' - has been presented. Exploiting these additional 4 control inputs which yield overactuation, the holocopter can achieve full controllability over its 6-dof body pose in space. Hereby the holocopter overcomes the usual limitations of most other UAVs including quadrotors and helicopters where for any desired trajectory the attitude (roll and pitch) of the UAV is coupled with its desired position. In the presented concept the 'holocopter' 4 additional degrees of freedom are implemented by individual control of the tilting angles of its four propellers (vertically fixed for standard quadrotors). This new set of $4 + 4$ available control inputs guarantees as proven in this thesis full controllability over the 6-dimensional pose of the holocopter main body in space.

In a detailed modeling section the holocopter equations of motion have been derived and the influence of aerodynamic effects under the desired flight regime has been investigated. Based on these results a control scheme was developed and adjusted so as to cope with the practical shortcomings of the first prototype.

A broad variety of ideal and realistic simulations have been conducted, discussed and reported to assess the effectiveness of the control strategy, to optimize the tuning process of the various gains and to identify deficits of the first prototype. Satisfactory flight performances could be presented in a broad variety of real experiments where complex maneuvers could be presented - impossible for standard quadrotor UAVs.

Additionally the second prototype, a completely revised system has been presented, that is currently under final software development (see figure 8.1). The new prototype aims

Figure 8.1: Photograph of the second prototype of the holocopter

at overcoming limitations and drawbacks of the first prototype. In particular, we were focusing on improving the holocopter actuation system (see Sect. 4.1.4), as well as obtaining a reduced overall weight, better onboard sensors, higher onboard computational power, and a more robust mechanical design. This will enable better tracking performance and allow for a full exploitation of the holocopter 6-dof motion capabilities in the planned interaction tasks with the environment.

Our future goal is to exploit the holocopter as a 'flying service robot' capable of advanced interaction tasks with the environment. Into this direction led the last section of this thesis (see Section 7) where an outline of possible environment-interactive control schemes was given.

Appendix

Appendix A

Technical Proofs

Proposition A.1. *If $w_i \neq 0$, $i = 1 \dots 4$, then $\rho_A = \text{rank}(\boldsymbol{A}) = 6$.*

Proof. From (3.5), note that $\text{rank}(\boldsymbol{A}) = \text{rank}(\boldsymbol{J}_R \boldsymbol{J}'_\alpha) = \text{rank}(\boldsymbol{J}'_\alpha)$ since $\boldsymbol{J}_R$ is a square nonsingular matrix. We now look for suitable nonsingular matrixes $\boldsymbol{M} \in \mathbb{R}^{6\times 6}$ and $\boldsymbol{N} \in \mathbb{R}^{8\times 8}$ such that $\boldsymbol{M}\boldsymbol{J}'_\alpha\boldsymbol{N}$ is in row canonical form, that is

$$\boldsymbol{M}\boldsymbol{J}'_\alpha\boldsymbol{N} = \left[\begin{array}{c|c} \mathbf{I}_6 & * \end{array}\right]. \tag{A.1}$$

If this manipulation is possible, then $\text{rank}(\boldsymbol{A}) = \text{rank}(\boldsymbol{J}'_\alpha) = \text{rank}(\boldsymbol{M}\boldsymbol{J}'_\alpha\boldsymbol{N}) = 6$. By inspection of $\boldsymbol{J}'_\alpha$, and after some (tedious) manipulations, a suitable $\boldsymbol{M}$ can be found as

$$\boldsymbol{M} = \begin{bmatrix} M_{11} & M_{12} & M_{13} & M_{14} & M_{15} & M_{16} \\ M_{21} & 0 & 0 & M_{24} & 0 & 0 \\ M_{31} & M_{32} & M_{33} & M_{34} & M_{35} & M_{36} \\ M_{41} & M_{42} & M_{43} & M_{44} & M_{45} & M_{46} \\ M_{51} & 0 & 0 & M_{54} & 0 & 0 \\ M_{61} & M_{62} & M_{63} & M_{64} & M_{65} & M_{66} \end{bmatrix}$$

with

$$\begin{cases} M_{11} = -\dfrac{k_m k_f L s_1 + (2k_m^2 + k_f^2 L^2) c_1}{2L^2 k_f^3 w_1}, & M_{12} = -\dfrac{L k_f c_1 - k_m s_1}{2L k_f^2 w_1}, \\ M_{13} = -\dfrac{L k_f s_1 + k_m c_1}{2L k_f^2 w_1}, & M_{14} = \dfrac{L k_f s_1 + 2k_m c_1}{2L^2 k_f^2 w_1}, \\ M_{15} = \dfrac{s_1}{2L k_f w_1}, & M_{16} = -\dfrac{c_1}{2L k_f w_1}, \\ M_{21} = -\dfrac{L k_f c_2 + k_m s_2}{L k_f^2 w_2}, & M_{24} = \dfrac{s_2}{L k_f w_2}, \\ M_{31} = -\dfrac{-L k_m k_f c_3 + (2k_m^2 + L^2 k_f^2) s_3}{2L^2 k_f^3}, & M_{32} = \dfrac{L k_f s_3 + k_m c_3}{2L k_f^2}, \\ M_{33} = \dfrac{L k_f c_3 - k_m s_3}{2L k_f^2}, & M_{34} = -\dfrac{L k_f c_3 - 2k_m s_3}{2L^2 k_f^2}, \\ M_{35} = \dfrac{c_3}{2L k_f}, & M_{36} = -\dfrac{s_3}{2L k_f}, \\ M_{41} = -\dfrac{-L k_m k_f c_1 + (2k_m^2 + L^2 k_f^2) s_1}{2L^2 k_f^3}, & M_{42} = -\dfrac{L k_f s_1 + k_m c_1}{2L k_f^2}, \\ M_{43} = \dfrac{L k_f c_1 - k_m s_1}{2L k_f^2}, & M_{44} = -\dfrac{L k_f c_1 - 2k_m s_1}{2L^2 k_f^2}, \\ M_{45} = -\dfrac{c_1}{2L k_f}, & M_{46} = -\dfrac{s_1}{2L k_f}, \\ M_{51} = -\dfrac{L k_f s_2 - k_m c_2}{L k_f^2}, & M_{54} = -\dfrac{c_2}{L k_f}, \\ M_{61} = -\dfrac{L k_f k_m s_3 + (2k_m^2 + L^2 k_f^2) c_3}{2L^2 k_f^3 w_3}, & M_{62} = \dfrac{L k_f c_3 - k_m s_3}{2L k_f^2 w_3}, \\ M_{63} = -\dfrac{L k_f s_3 + k_m c_3}{2L k_f^2 w_3}, & M_{64} = \dfrac{L k_f s_3 + 2k_m c_3}{2L^2 k_f^2 w_3}, \\ M_{65} = -\dfrac{s_3}{2L k_f w_3}, & M_{66} = -\dfrac{c_1}{2L k_f^2 w_3}, \end{cases}$$

and $\det(\boldsymbol{M}) = -\dfrac{1}{4L^3 k_f^6 w_1 w_2 w_3}$. As for $\boldsymbol{N}$, it is just a column permutation matrix

$$\boldsymbol{N} = \begin{bmatrix} 1 & 0 & 0 & 0 & 0 & 0 & 0 & 0 \\ 0 & 1 & 0 & 0 & 0 & 0 & 0 & 0 \\ 0 & 0 & 1 & 0 & 0 & 0 & 0 & 0 \\ 0 & 0 & 0 & 0 & 0 & 0 & 1 & 0 \\ 0 & 0 & 0 & 1 & 0 & 0 & 0 & 0 \\ 0 & 0 & 0 & 0 & 1 & 0 & 0 & 0 \\ 0 & 0 & 0 & 0 & 0 & 1 & 0 & 0 \\ 0 & 0 & 0 & 0 & 0 & 0 & 0 & 1 \end{bmatrix}.$$

It is then easy to see that, if $w_1 \neq 0$, $w_2 \neq 0$ and $w_3 \neq 0$, matrix $\boldsymbol{M}$ is always well-defined and (A.1) always holds, proving that $\rho_A = \text{rank}(\boldsymbol{A}) = 6$. Note that in this case, because of

the particular choice made for $\boldsymbol{M}$, no condition is present on w_4 (w_4 could vanish). This is coherent with the intuition that three actuated propellers can be sufficient to provide full mobility to the quadrotor body (6 inputs for 6 rigid body dofs). However, presence of a fourth active propeller ($w_4 \neq 0$ in this case) guarantees the needed actuation redundancy exploited in Sect. 3. □

Appendix B

Schematics

B.1 Mechanical schematics

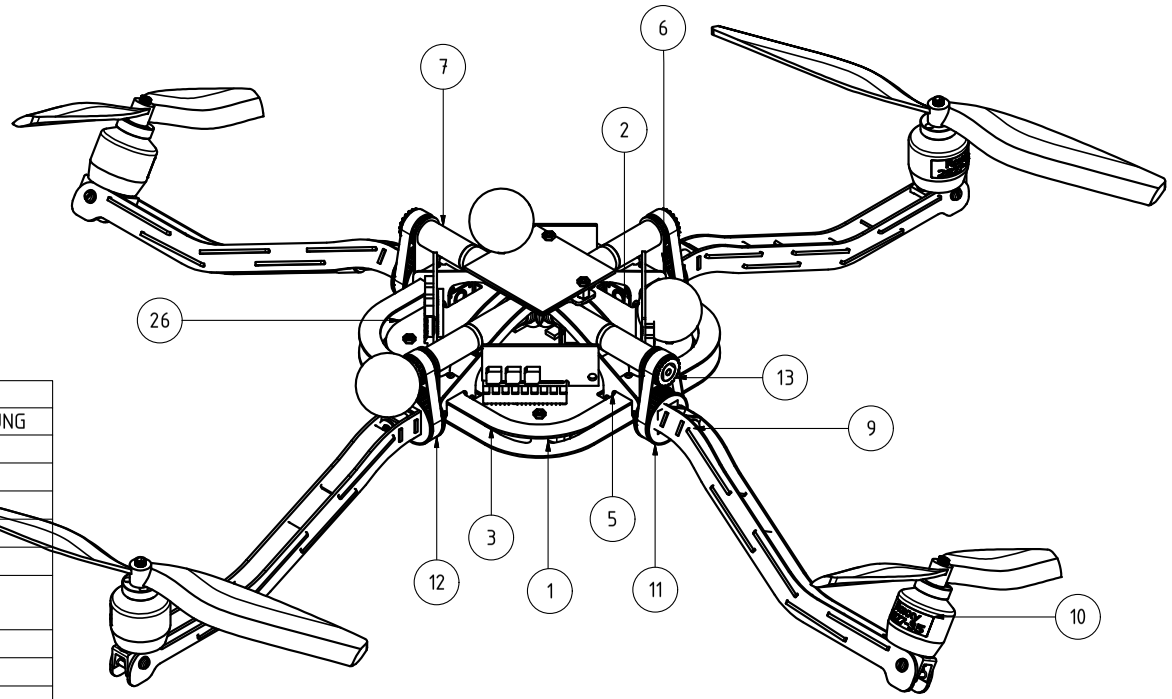

TEILELISTE			
OBJEKT	ANZAHL	BAUTEILNUMMER	BESCHREIBUNG
1	1	Rahmentraeger	
2	8	Wellentraeger	
3	1	Rahmentraeger_2	
5	4	Bruecke	
6	4	Motortraeger	
7	4	Motor_Combination_13	
9	4	Hauptwelle	
10	4	Arm	
11	4	Synchrone Riemenscheibe2	
12	4	Zahnriemen	
13	4	Synchrone Riemenscheibe1	
18	1	PowerDistBoard	
19	1	FlightControl	
20	1	Odroid_U2_Traeger	
21	1	Odroid_U2	
23	4	Brushless_Ctrler	
24	1	Akku_2200mAh	
26	1	EPOS2_Module	
32	4	Motor_Stuetze	
33	3	Marker	

	DATUM	Name
Gezeichnet	30.05.2013	Markus
Kontrolliert		
Norm		

Status	Aenderungen	DATUM	Name

SQC2_final

1

A3

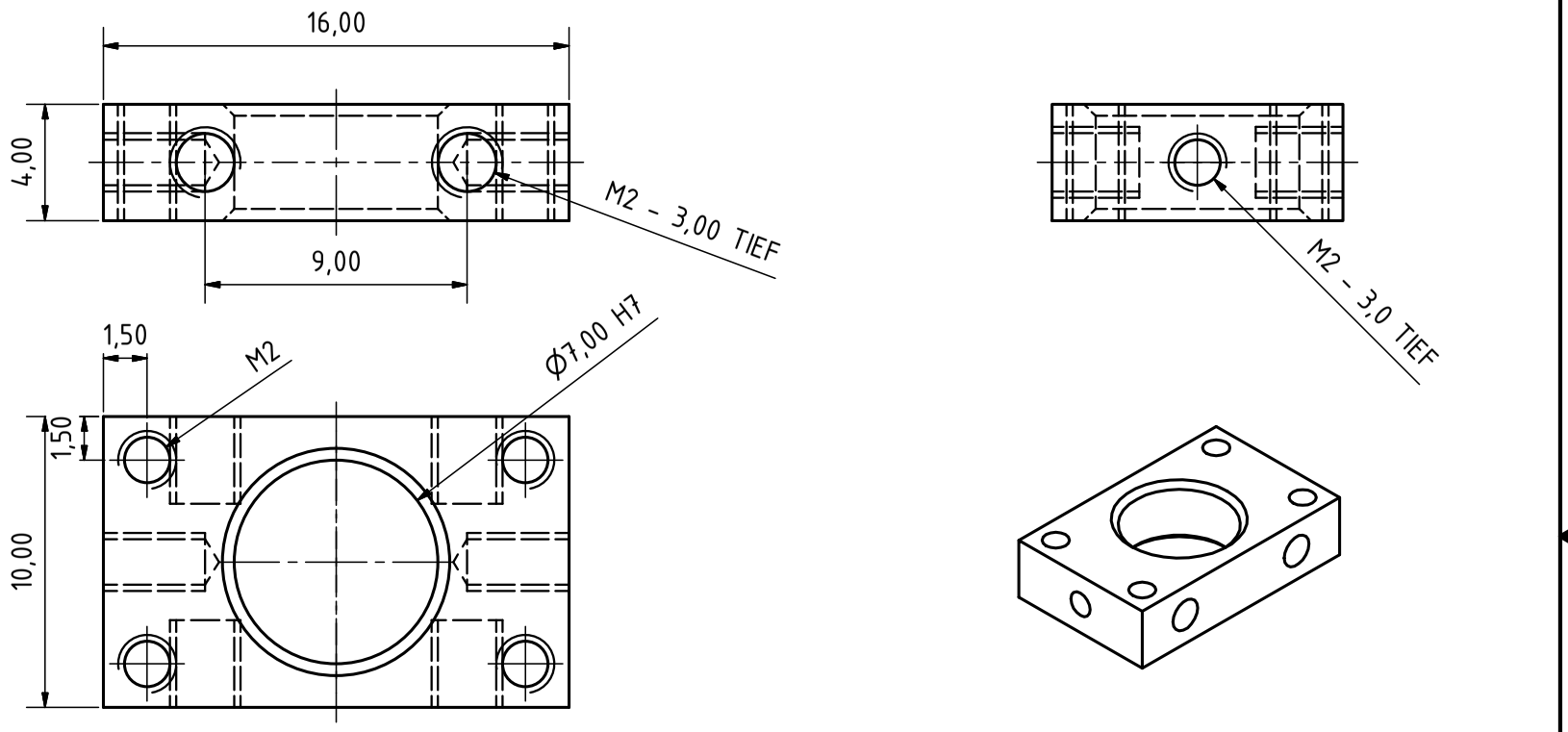

					DATUM	Name
				Gezeichnet	30.05.2013	Markus
				Kontrolliert		
				Norm		
Status	Änderungen	DATUM	Name			

Aluminium

Wellentraeger

1

A4

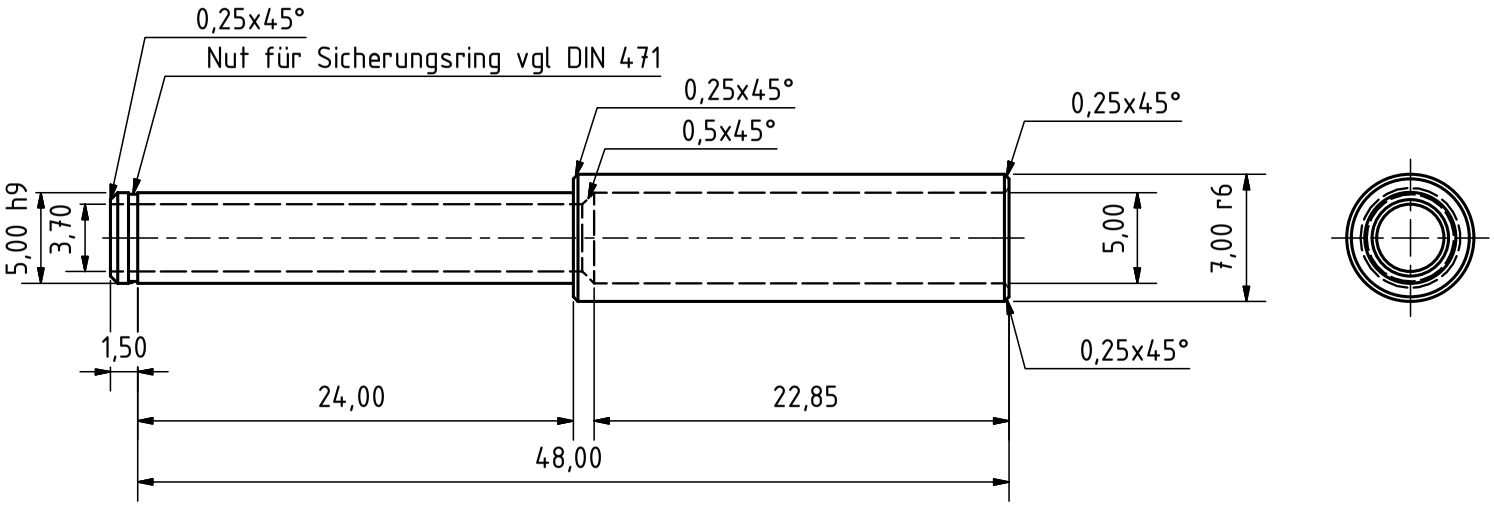

					DATUM	Name
				Gezeichnet	29.05.2013	Markus
				Kontrolliert		
				Norm		
Status	Änderungen	DATUM	Name			

Rostfreier Edelstahl
z.B.: X20Cr13

Hauptwelle

1

A4

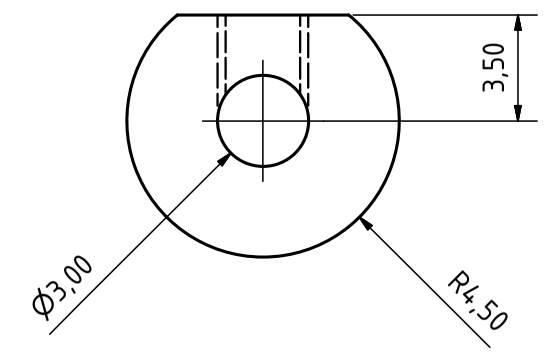

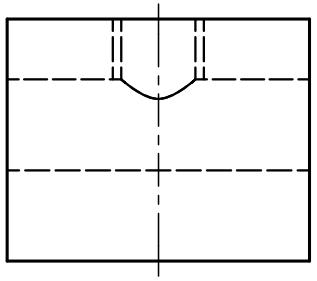

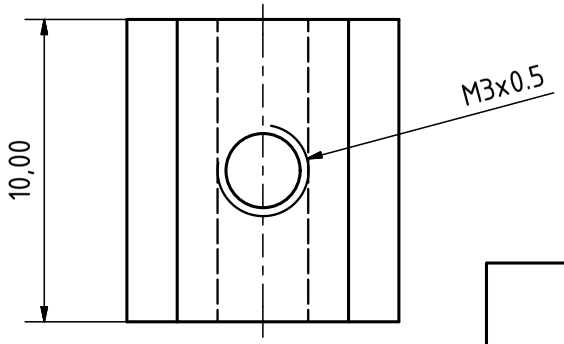

					DATUM	Name
				Gezeichnet	18.06.2013	Markus
				Kontrolliert		
				Norm		
Status	Änderungen	DATUM	Name			

Aluminium

Motor_Fitting

1

A4

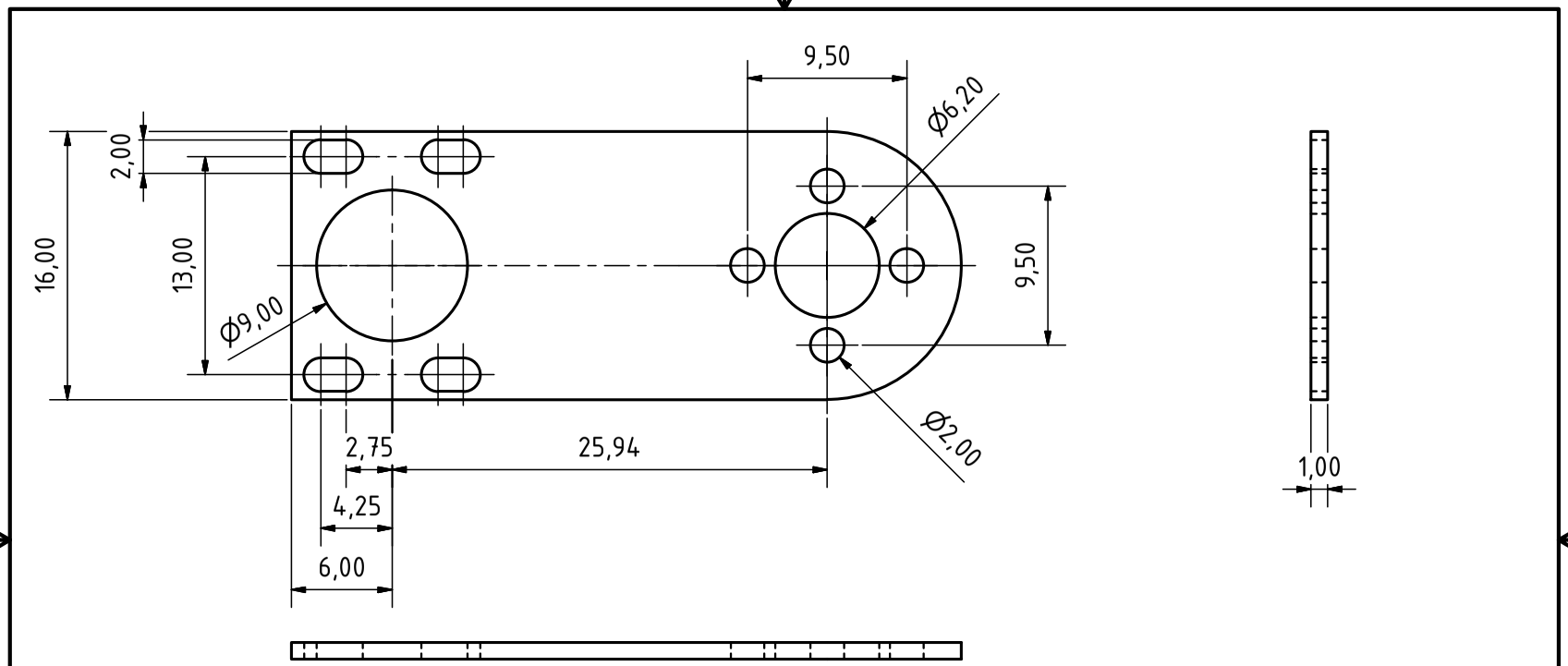

					DATUM	Name
				Gezeichnet	30.05.2013	Markus
				Kontrolliert		
				Norm		
Status	Änderungen	DATUM	Name			

Aluminium

Motortraeger

1

A4

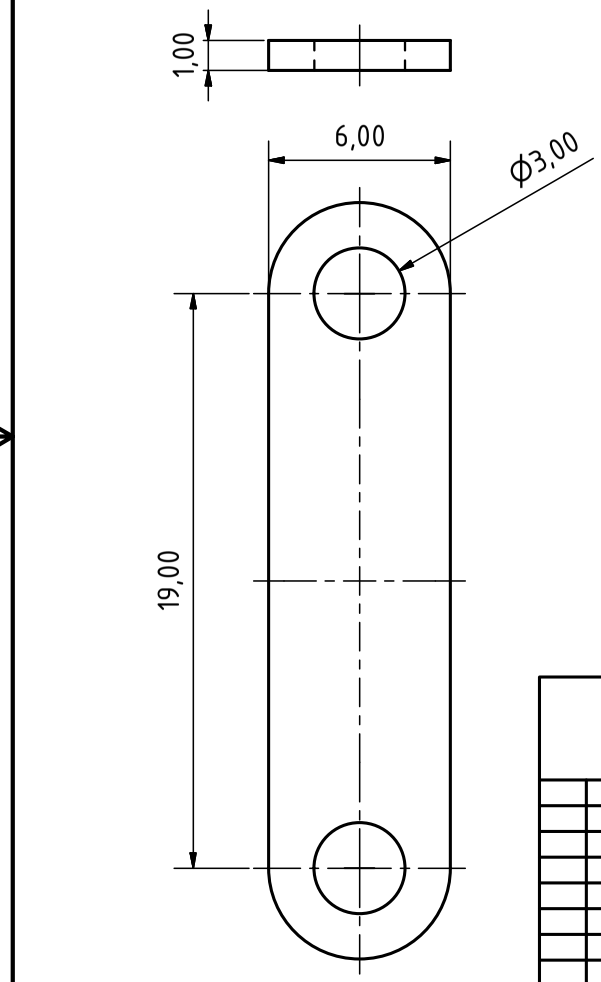

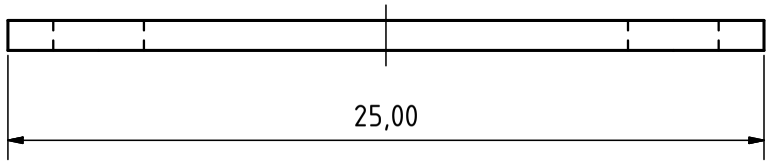

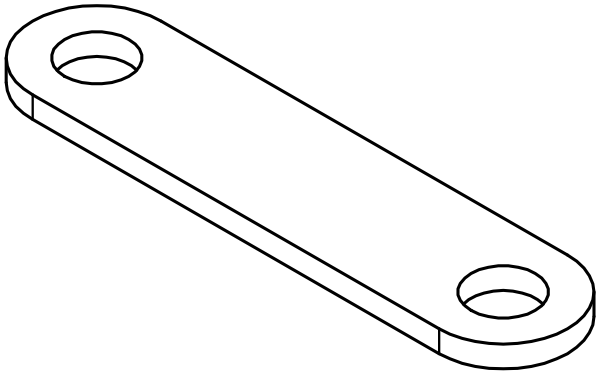

					DATUM	Name	
				Gezeichnet	30.05.2013	Markus	Aluminium
				Kontrolliert			
				Norm			
							Motor_Blech 1
Status	Änderungen	DATUM	Name				A4

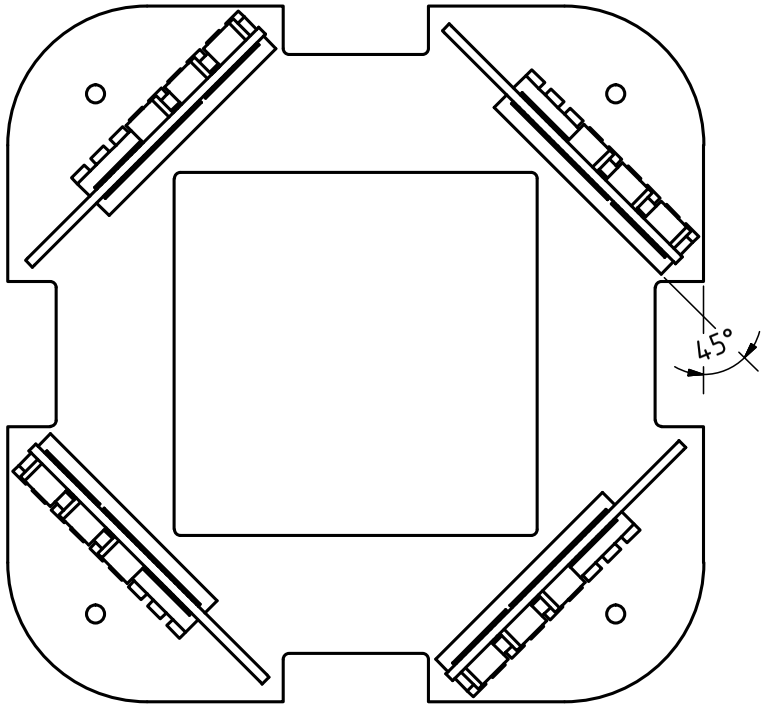

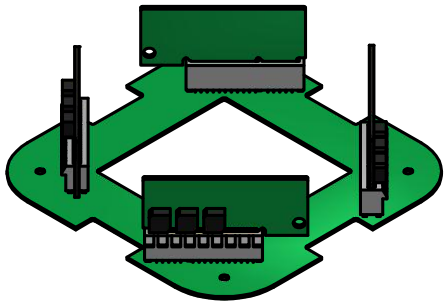

					DATUM	Name
				Gezeichnet	19.06.2013	Markus
				Kontrolliert		
				Norm		
Status	Änderungen	DATUM	Name			

EPOS2_Module

1

A4

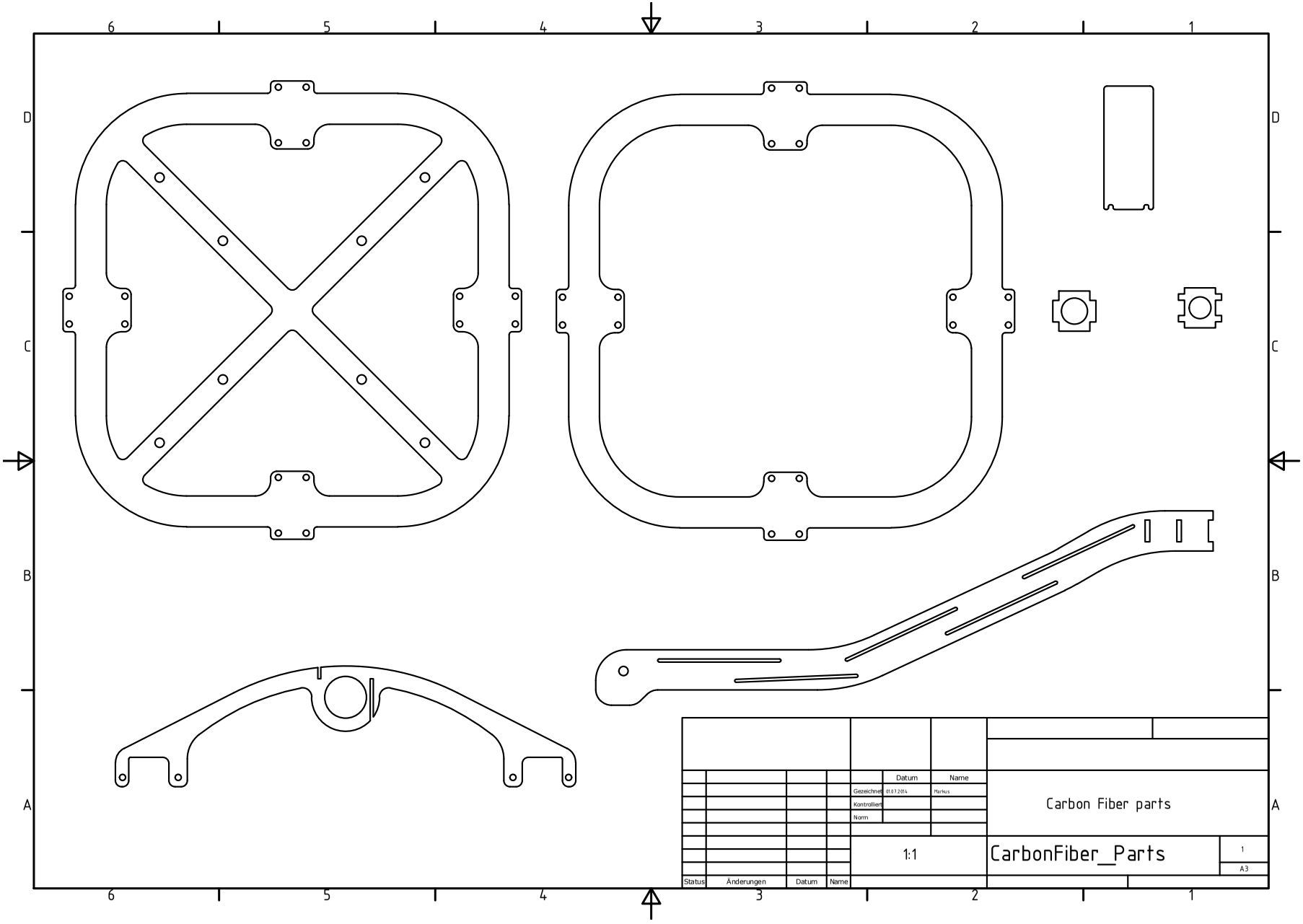
6
5
4
3
2
1
D
C
B
A
Datum
Name
Gezeichnet
01.07.2014
Markus
Kontrolliert
Norm
Carbon Fiber parts
1:1
CarbonFiber_Parts
1
A3
Status
Änderungen
Datum
Name

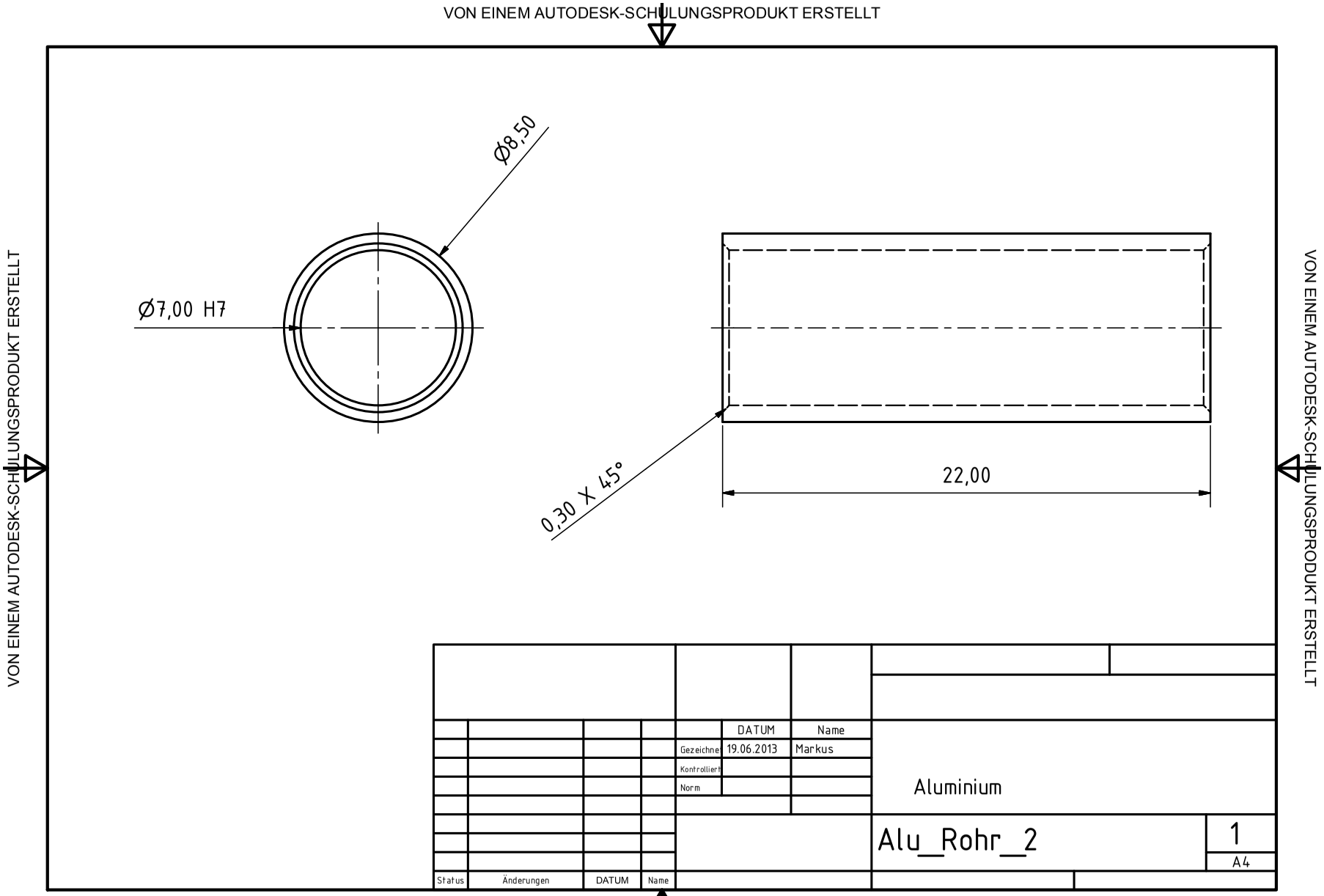

					DATUM	Name
				Gezeichnet	19.06.2013	Markus
				Kontrolliert		
				Norm		
Status	Änderungen	DATUM	Name			

Aluminium

Alu_Rohr_2

1

A4

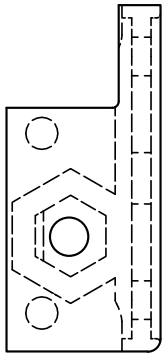

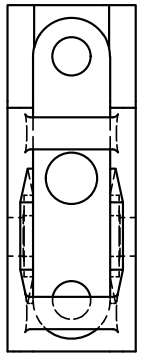

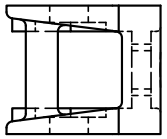

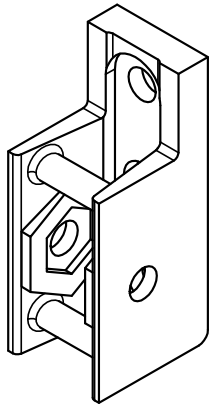

Brushless Motor Holder

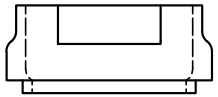

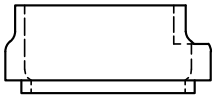

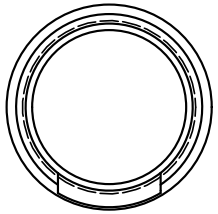

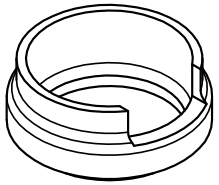

Servo Motor Holder

					Datum	Name	
				Gezeichnet	01.07.2014	Markus	
				Kontrolliert			
				Norm			
						3D_printer_I	1
							A3
Status	Änderungen	Datum	Name				

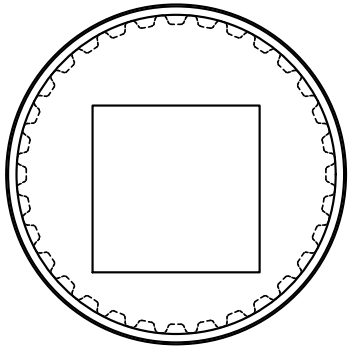

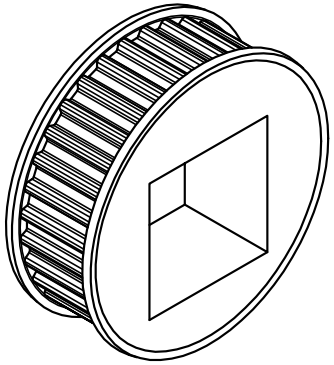

Pulley I

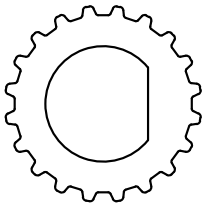

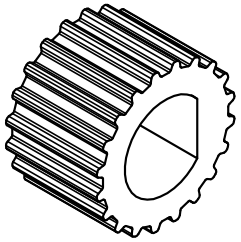

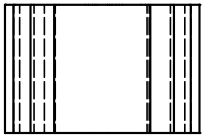

Pulley II

					Datum	Name	
				Gezeichnet	01.07.2014	Markus	
				Kontrolliert			
				Norm			
					3:1	3D_printer_II	1
							A3
Status	Änderungen	Datum	Name				

B.2 Electrical schematics

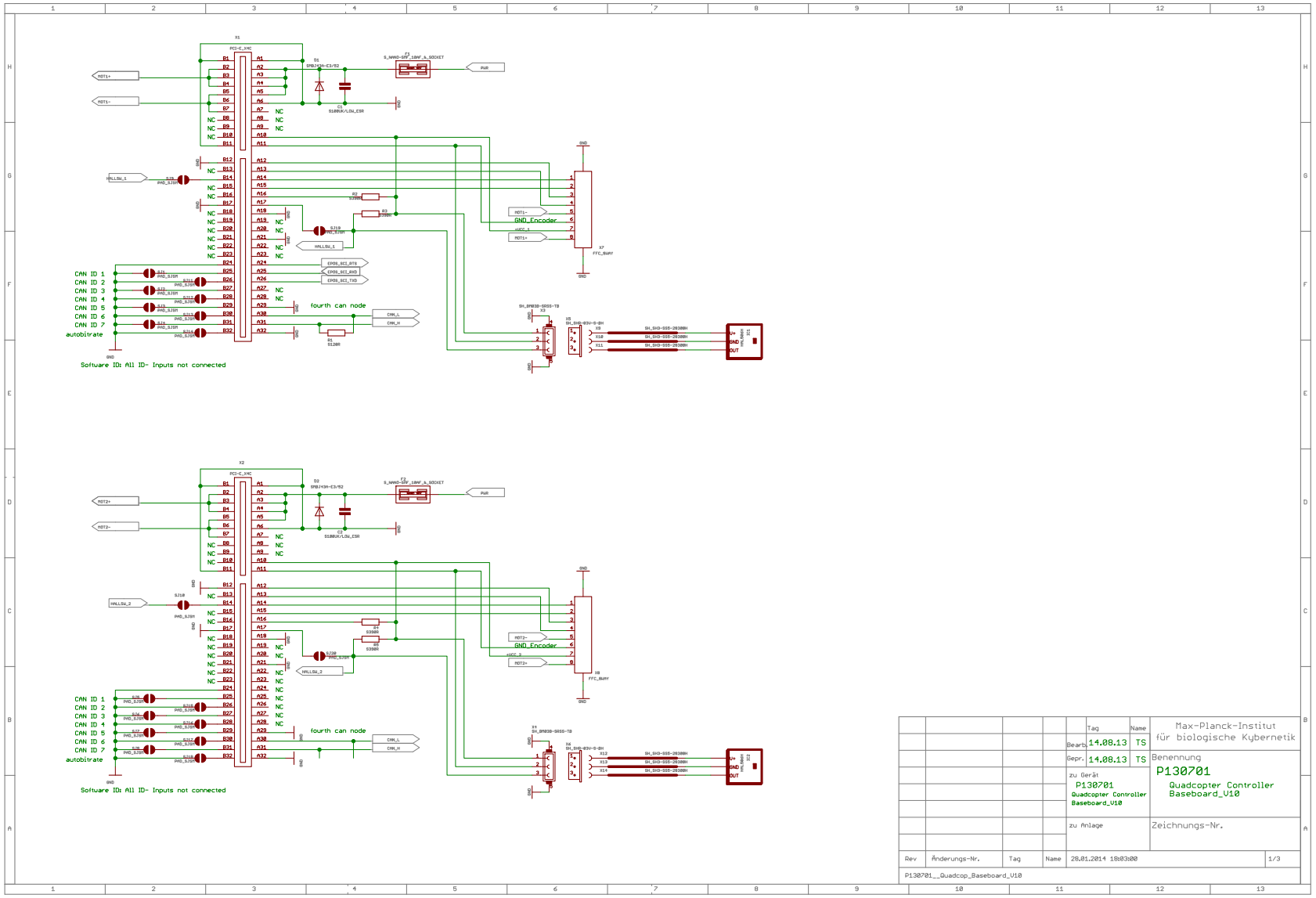

					Tag	Name	Max-Planck-Institut für biologische Kybernetik
				Bearb.	14.08.13	TS	
				Gepr.	14.08.13	TS	Benennung
				zu Gerät	P130701 Quadcopter Controller Baseboard_V10		P130701 Quadcopter Controller Baseboard_V10
				zu Anlage			Zeichnungs-Nr.
Rev	Änderungs-Nr.	Tag	Name	28.01.2014 18:03:00			1/3
P130701__Quadcop_Baseboard_V10							

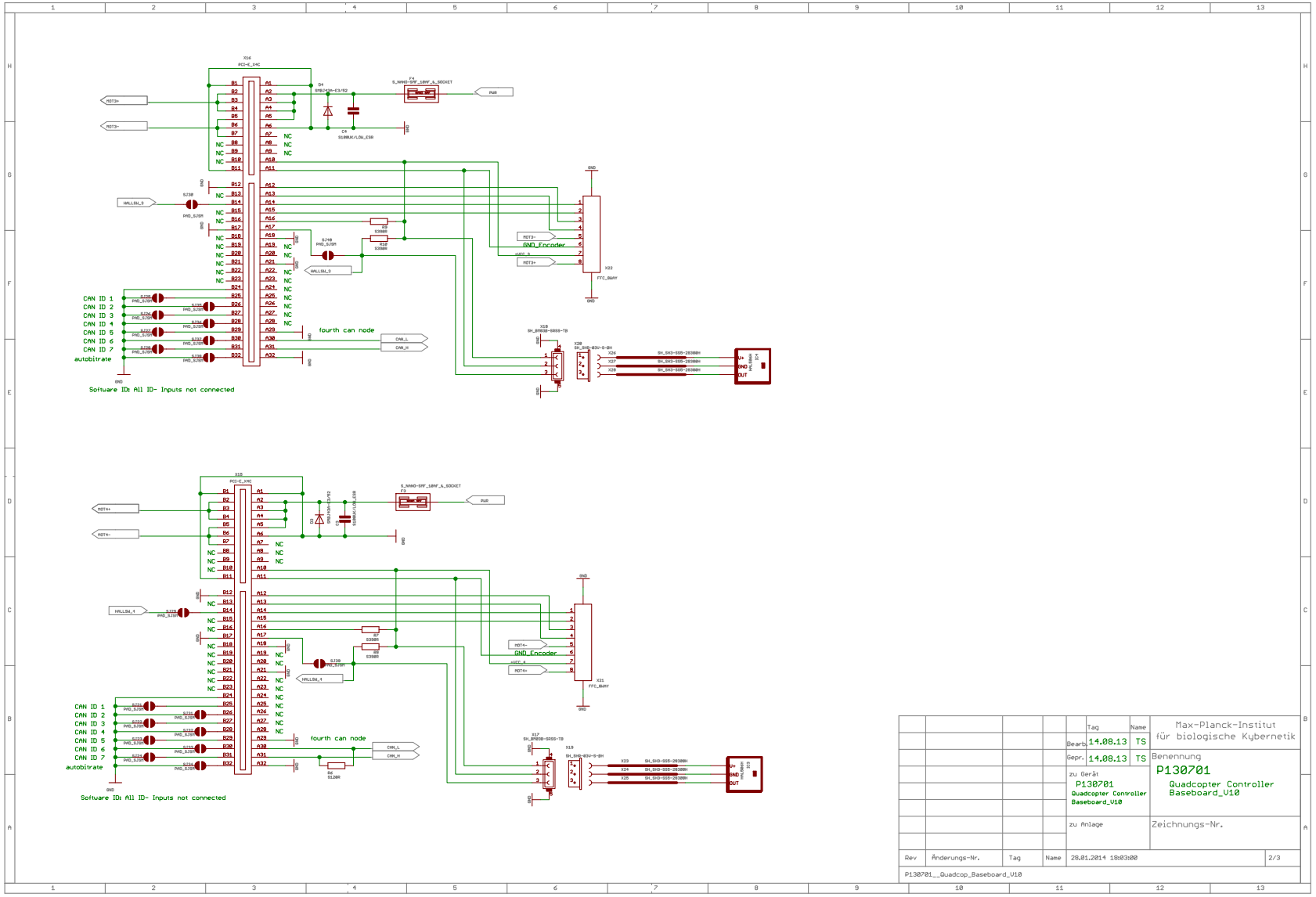

					Tag	Name
				Bearb.	14.08.13	TS
				Gepr.	14.08.13	TS
				zu Gerät	P130701 Quadcopter Controller Baseboard_V10	
				zu Anlage		

Max-Planck-Institut für biologische Kybernetik

Benennung

P130701

Quadcopter Controller Baseboard_V10

Zeichnungs-Nr.

Rev	Änderungs-Nr.	Tag	Name	28.01.2014 18:03:00	2/3

P130701__Quadcop_Baseboard_V10

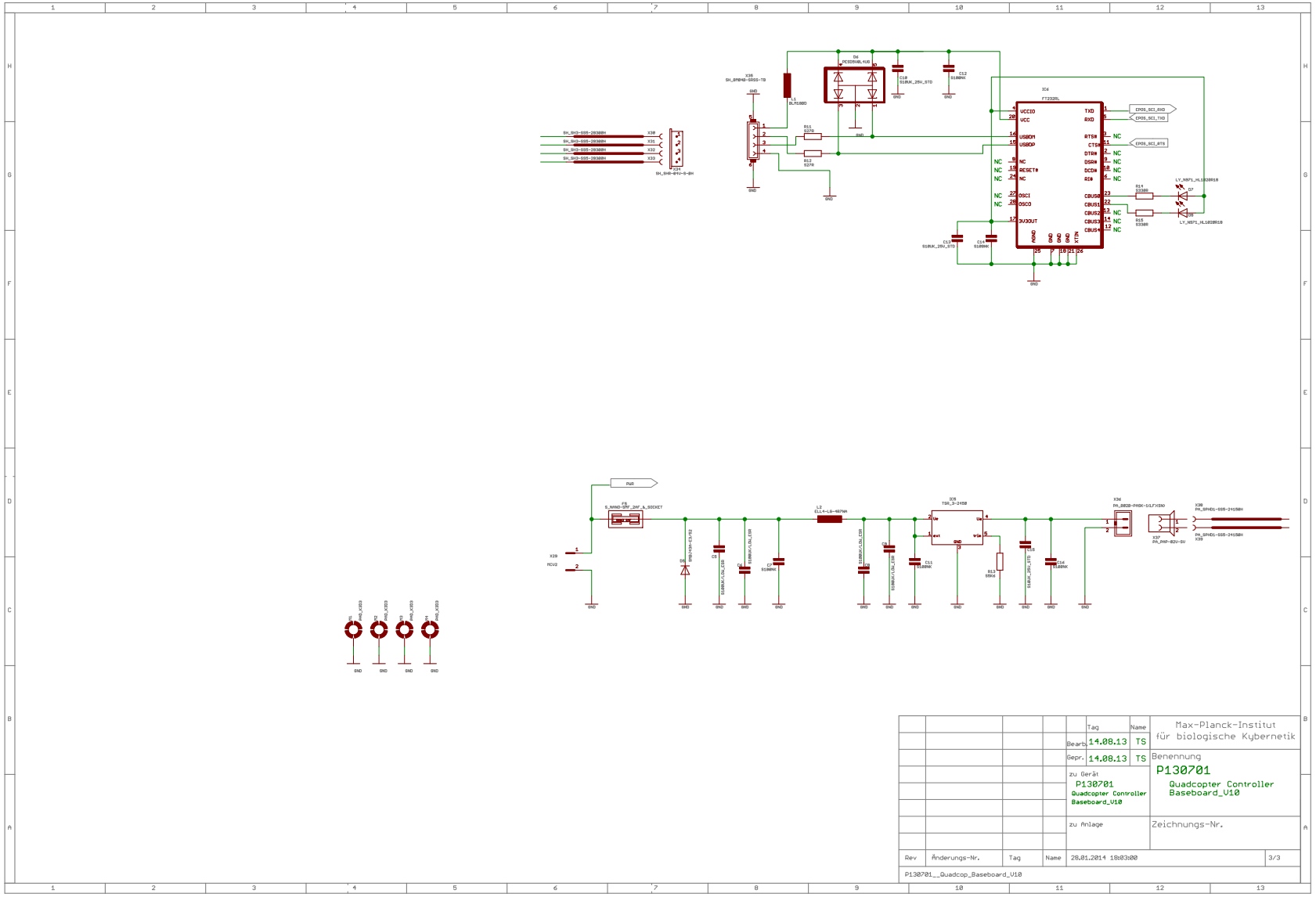
IC4
FT232RL
VCCIO
VCC
USBDM
USBDP
RESET#
OSCI
OSCO
3V3OUT
TXD
RXD
RTS#
CTS#
DTR#
DSR#
DCD#
RI#
CBUS0
CBUS1
CBUS2
CBUS3
CBUS4
GND
EPOS_SCI_RXD
EPOS_SCI_TXD
EPOS_SCI_RTS
IC5
TSR_3-2450
L2
ELL4-LG-4R7NA
FB
G_NANO-SMF_2WF_N_SOCKET
PWR
X36
PH_B8B2B-PASK-1(LF)(SN)
X38
PH_SPHD1-SSS-2x15BH
X37
PH_PAP-B2V-SU
X39
X29
MCV2
Tag
Name
Bearb.
14.08.13
TS
Gepr.
14.08.13
TS
Max-Planck-Institut
für biologische Kybernetik
Benennung
P130701
Quadcopter Controller
Baseboard_V10
zu Gerät
P130701
Quadcopter Controller
Baseboard_V10
zu Anlage
Zeichnungs-Nr.
Rev
Änderungs-Nr.
Tag
Name
28.01.2014 18:03:00
3/3
P130701__Quadcop_Baseboard_V10

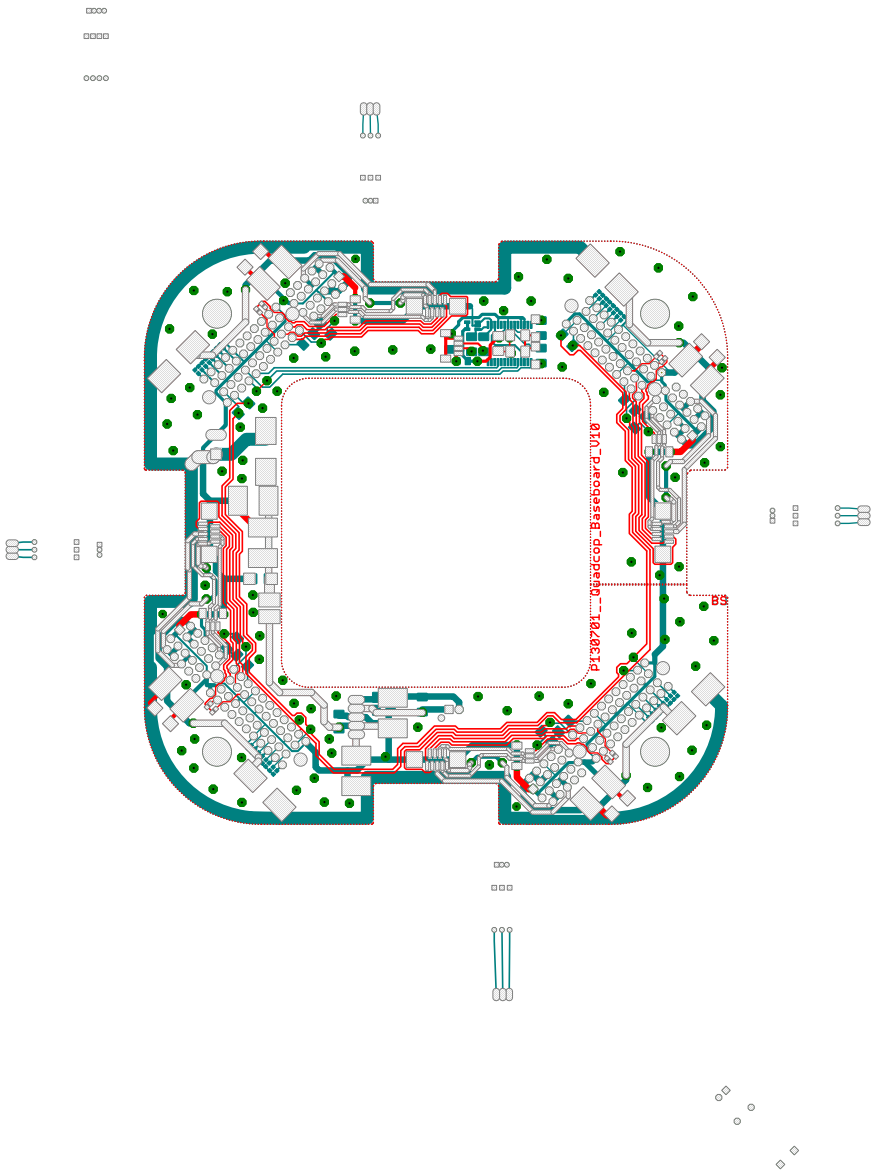
P130701__Quadcop_Baseboard_V10
BS

Bibliography

M. Ahmad, editor. *Advances in Motor Torque Control*, chapter Sensorless Torque/Force Controll. InTech, 2011. ISBN 9789533076867. doi: 10.5772/20741.

A. Benallegue, A. Mokhtari, and L. Fridman. Feedback linearization and high order sliding mode observer for a quadrotor uav. In *Variable Structure Systems, 2006. VSS'06. International Workshop on*, pages 365–372, June 2006. doi: 10.1109/VSS.2006.1644545.

S. Bouabdallah, M. Becker, and R. Siegwart. Autonomous miniature flying robots: Coming soon! *IEEE Robotics and Automation Magazine*, 13(3):88–98, 2007.

A. Briod. *Robust Autonomous Flight in Unstructured Environments.* PhD thesis, STI, Lausanne, 2014.

A. De Luca, G. Oriolo, and B. Siciliano. Robot redundancy resolution at the acceleration level. *Robotica*, 4(2):97–106, 1992.

A. De Luca, G. Oriolo, and P. Robuffo Giordano. Kinematic control of nonholonomic mobile manipulators in the presence of steering wheels. In *2010 IEEE Int. Conf. on Robotics and Automation*, pages 1792–1798, 2010.

EU Collaborative Project ICT-248669 AIRobots. www.airobots.eu.

EU Collaborative Project ICT-287617 ARCAS. www.arcas-project.eu.

R. Falconi and C. Melchiorri. Dynamic Model and Control of an Over-Actuated Quadrotor UAV. In *Proc. of the 10th IFAC Symposium on Robotic Control*, pages 192–197, 2012.

Fay. G. Derivation of the Aerodynamic Forces for the Mesicopter Simulation. Stanford University, 2001.

J. Fink, N. Michael, S. Kim, and V. Kumar. Planning and control for cooperative manipulation and transportation with aerial robots. *Intern. Journal of Robotics Research*, 30(3), 2010.

F. Forte, R. Naldi, A. Macchelli, and L. Marconi. Impedance control of an aerial manipulator. In *American Control Conference (ACC), 2012*, pages 3839–3844, June 2012a.

F. Forte, R. Naldi, A. Serrani, and L. Marconi. Control of Modular Aerial Robots: Combining Under- and Fully-Actuated Behaviors. In *2012 IEEE Conf. on Decision and Control*, pages 1160–1165, 2012b.

A. Franchi, C. Secchi, M. Ryll, H. H. Bülthoff, and P. Robuffo Giordano. Shared control: Balancing autonomy and human assistance with a group of quadrotor uavs. *IEEE Robotics and Automation Magazine*, 19(3):57–68, 2012.

L. Gentili, R. Naldi, and L. Marconi. Modelling and control of VTOL UAVs interacting with the environment. In *2008 IEEE Conf. on Decision and Control*, pages 1231–1236, 2008.

G. Gioioso, M. Ryll, D. Prattichizzo, H. Bülthoff, and A. Franchi. Turning a near-hovering controlled quadrotor into a 3d force effector. *ICRA 2013*, 2013.

G. Gioioso, M. Ryll, D. Prattichizzo, H. H. Bülthoff, and A. Franchi. Turning a near-hovering controlled quadrotor into a 3d force effector. In *2014 IEEE Int. Conf. on Robotics and Automation*, Hong Kong, China, 05/2014 2014.

GmbH HiSystems. Available: http://www.mikrokopter.de. online, 6 2014.

D. Gurdan, J. STumpf, M. Achtelik, K.-M. Dorh, G. Hirzinger, and D. Rus. Energy-efficient autonomous four-rotor flying robot controlled at 1 kHz. In *2007 IEEE Int. Conf. on Robotics and Automation*, pages 361–366, 2007.

M.-D. Hua, T. Hamel, P. Morin, and C. Samson. A Control Approach for Thrust-Propelled Underactuated Vehicles and its Application to VTOL Drones. *IEEE Trans. on Automatic Control*, 54(8):1837–1853, 2009.

M.-D. Hua, T. Hamel, P. Morin, and C. Samson. Introduction to feedback control of underactuated vtol vehicles: A review of basic control design ideas and principles. *IEEE Control System Magazine*, 33(1):61–75, 2013a.

M.-D. Hua, T. Hamel, and C. Samson. Control of VTOL Vehicles with Thrust-direction Tilting. arXiv:1308.0191, 2013b.

W. Iida and K. Ohnishi. Sensorless force control with force error observer. In *Industrial Technology, 2003 IEEE International Conference on*, volume 1, pages 157–162 Vol.1, Dec 2003. doi: 10.1109/ICIT.2003.1290260.

A. Isidori. *Nonlinear Control Systems*. Springer, 3rd edition, 1995.

S. Jeong, S. Jung, and M. Tomizuka. Attitude control of a quad-rotor system using an acceleration-based disturbance observer: An empirical approach. In *Advanced Intelligent Mechatronics (AIM), 2012 IEEE/ASME International Conference on*, pages 916–921, July 2012. doi: 10.1109/AIM.2012.6265965.

S. Katsura, Y. Matsumoto, and K. Ohnishi. Modeling of force sensing and validation of disturbance observer for force control. In *Industrial Electronics Society, 2003. IECON '03. The 29th Annual Conference of the IEEE*, volume 1, pages 291–296 vol.1, Nov 2003. doi: 10.1109/IECON.2003.1279994.

F. Kendoul, I. Fantoni, and R. Lozano. Modeling and control of a small autonomous aircraft having two tilting rotors. *IEEE Trans. on Robotics*, 22(6):1297–1302, 2006.

I. Khalil and A. Sabanovic. Action-reaction based parameters identification and states estimation of flexible systems. In *Industrial Electronics (ISIE), 2010 IEEE International Symposium on*, pages 46–51, July 2010a. doi: 10.1109/ISIE.2010.5637217.

I. Khalil and A. Sabanovic. Sensorless action-reaction-based residual vibration suppression for multi-degree-of-freedom flexible systems. In *IECON 2010 - 36th Annual Conference on IEEE Industrial Electronics Society*, pages 1633–1638, Nov 2010b. doi: 10.1109/IECON.2010.5675440.

A. Kushleyev, D. Mellinger, and V. Kumar. Towards A Swarm of Agile Micro Quadrotors. In *2012 Robotics: Science and Systems*, 2012.

T. Lee, M. Leok, and N. H. McClamroch. Geometric tracking control of a quadrotor UAV on $SE(3)$. In *2010 IEEE Conf. on Decision and Control*, pages 5420–5425, 2010.

Q. Lindsey, D. Mellinger, and V. Kumar. Construction of cubic structures with quadrotor teams. In *Robotics: Science and Systems*, 2011.

Y. Long and D. J. Cappelleri. Linear Control Design, Allocation, and Implementation for the Omnicopter MAV. In *2013 IEEE Int. Conf. on Robotics and Automation*, pages 289–294, 2013.

R. Mahony, V. Kumar, and P. Corke. Multirotor aerial vehicles: Modeling, estimation, and control of quadrotor. *IEEE Robotics & Automation Magazine*, 19(3):20–32, 2012.

M. Manubens, D. Devaurs, L. Ros, and J. Cortés. Motion Planning for 6-D Manipulation with Aerial Towed-cable Systems. In *2013 Robotics: Science and Systems*, Berlin, Germany, June 2013.

L. Marconi and R. Naldi. Control of aerial robots. hybrid force/position feedback for a ducted-fan. *IEEE Control System Magazine*, 32(4):43–65, 2012.

D. Mellinger and V. Kumar. Minimum snap trajectory generation and control for quadrotors. In *2011 IEEE Int. Conf. on Robotics and Automation*, pages 2520–2525, 2011.

D. Mellinger, N. Michael, and V. Kumar. Trajectory generation and control for precise aggressive maneuvers with quadrotors. In *Proc. of the 2010 Int. Symposium on Experimental Robotics*, 2010.

N. Michael, J. Fink, and V. Kumar. Cooperative manipulation and transportation with aerial robots. In *Robotics: Science and Systems*, Seattle, USA, June 2009.

R. Naldi and L. Marconi. Modeling and control of the interaction between flying robots and the environment. In *Proc. of the 2010 IFAC NOLCOS*, 2010.

R. Naldi, L. Gentili, L. Marconi, and A. Sala. Design and experimental validation of a nonlinear control law for a ducted-fan miniature aerial vehicle. *Control Engineering Practice*, 18(7):747–760, 2010.

K. T. Oner, E. Cetinsoy, M. Unel, M. F. Aksit, I. Kandemir, and K. Gulez. Dynamic model and control of a new quadrotor unmanned aerial vehicle with tilt-wing mechanism. In *Proc. of the 2008 World Academy of Science, Engineering and Technology*, pages 58–63, 2008.

K. T. Oner, E. Cetinsoy, E. Sirimoglu, C. Hancer, T. Ayken, and M. Unel. LQR and SMC stabilization of a new unmanned aerial vehicle. In *Proc. of the 2009 World Academy of Science, Engineering and Technology*, pages 554–559, 2009.

OpenServo.org. Available: http://openservo.com. online, 6 2014.

P. E. I. Pound, D. R. Bersak, and A. M. Dollar. Grasping from the air: Hovering capture and load stability. In *2011 IEEE Int. Conf. on Robotics and Automation*, pages 2491–2498, 2011.

P. Pounds, R. Mahony, and P. Corke. Modelling and control of a large quadrotor robot. *Control Engineering Practice*, 18(7):691–699, 2010.

robbe Modellsport GmbH & Co. KG. Available: http://www.robbe.de/servo-s-3150-digital.html. online, 6 2014.

M. Ryll, H. H. Bülthoff, and P. Robuffo Giordano. Modeling and Control of a Quadrotor UAV with Tilting Propellers. In *2012 IEEE Int. Conf. on Robotics and Automation*, pages 4606–4613, 2012.

M. Ryll, H. H. Bülthoff, and P. Robuffo Giordano. First Flight Tests for a Quadrotor UAV with Tilting Propellers. In *2013 IEEE Int. Conf. on Robotics and Automation*, pages 295–302, 2013.

M. Ryll, H. H. Bülthoff, and P. Robuffo Giordano. A novel overactuated quadrotor uav: Modeling, control and experimental validation. *IEEE Transactions on Control Systems Technology*, to be published 2014.

A. Sanchez, J. Escareño, O. Garcia, and R. Lozano. Autonomous hovering of a noncyclic tiltrotor UAV: Modeling, control and implementation. In *Proc. of the 17th IFAC Wold Congress*, pages 803–808, 2008.

S. Shen, Y. Mulgaonkar, N. Michael, and V. Kumar. Vision-Based State Estimation and Trajectory Control Towards High-Speed Flight with a Quadrotor. In *2013 Robotics: Science and Systems*, 2013.

B. Siciliano and O. Khatib, editors. *Handbook of Robotics*, chapter Force Control. Springer, 2008. ISBN 9783540239574.

R. Spica, A. Franchi, G. Oriolo, H. H. Bülthoff, and P. Robuffo Giordano. Aerial Grasping of a Moving Target with a Quadrotor UAV. In *2012 IEEE/RSJ Int. Conf. on Intelligent Robots and Systems*, pages 4985–4992, 2012.

K. Sreenath and V. Kumar. Dynamics, Control and Planning for Cooperative Manipulation of Payloads Suspended by Cables from Multiple Quadrotor Robots. In *2013 Robotics: Science and Systems*, 2013.

W. Stepniewski and C. Keys, editors. *Rotary-Wing Aerodynamics*. Dover Publications, 1984.

K. P. Valavanis, editor. *Advances in Unmanned Aerial Vehicles: State of the Art and the Road to Autonomy*. Springer, 2007.

R. Voyles and G. Jiang. Hexrotor uav platform enabling dextrous interaction with structures - preliminary work. In *Safety, Security, and Rescue Robotics (SSRR), 2012 IEEE International Symposium on*, pages 1–7, 2012.

W. A. Wolovich. *Automatic Control Systems*. Oxford University Press, 1994.